North Atlantic multidecadal variability in coupled climate models

- Mechanisms and responses

Iselin Medhaug

Dissertation for the degree of Philosophiae Doctor (PhD)

Geophysical Institute, University of Bergen, Norway

February, 2011

Acknowledgments

This thesis would not have been possible without the help of several people. First of all I would like thank and to express my sincere gratitude to Tore for all the help and support the last three years. It is not easy turning a UV researcher into an oceanographer, but you had the faith and the patience, and I really appreciate all the hard work you put into getting me through it. I would also like to thank Helene and my "adopted supervisors", Tor, Odd Helge and Mats, for the discussions and collaboration. A special thanks to Helene for letting me come and stay in Seattle.

Several other people deserve to be mentioned, amongst them Asgeir Sorteberg, Nils Gunnar Kvamstø, David Stephenson, Torbjørn Lorentzen, Ingo Bethke, Helge Drange, Peter Rhines and Daniel Soule. Thanks to Christophe and Torleif for the morning coffee, I wouldn't have become addicted to coffee without your help. I would also like to thank the Geophysical Microbrewery crew for help with keeping the sanity and motivation.

Last but not least, I would like to thank Marius. It's been priceless having you around in both ups and downs. I would probably not have finished this thesis without your support and you reminding me that there is a life outside of work. Thanks for the never ending encouragement and for not letting me give up.

This work has been supported by the Research Council of Norway through the NorClim project.

Iselin Medhaug
Bergen, February 2011

Abstract

Global atmosphere-ocean general circulation models have been used to investigate mechanisms controlling the North Atlantic low-frequency variability, with the focus on the Atlantic Meridional Overturning Circulation, the Subpolar Gyre dynamics and the North Atlantic basin scale sea surface temperatures, called the Atlantic Multidecadal Oscillation. The understanding of the dynamics of, and mechanisms behind the variability in these components of the climate system are of great importance for both climate reconstruction and predictability. We have shown that the air-sea interaction plays an important role in the ocean dynamics and ocean circulation in the North Atlantic.

Contents

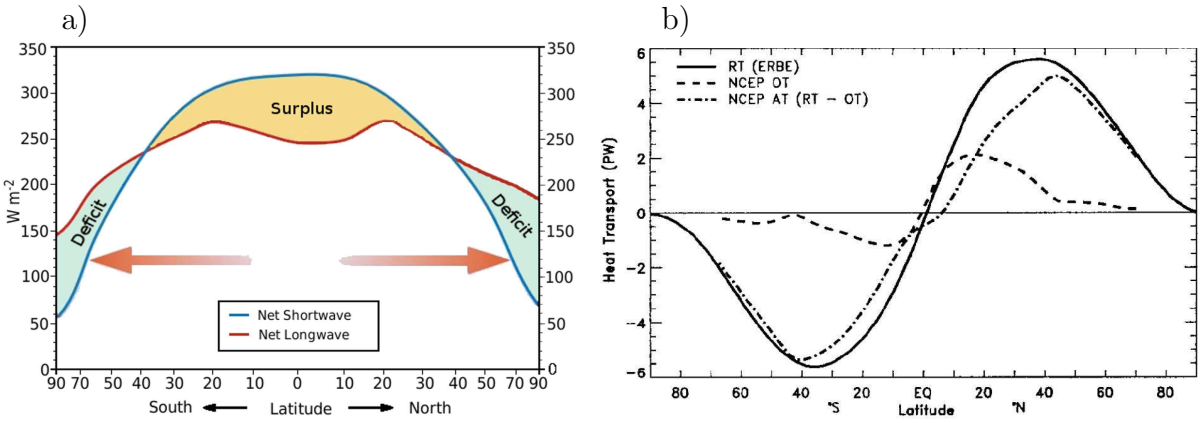

Figure 1: a) Global radiation balance with net incoming shortwave solar radiation (blue) and net outgoing longwave radiation (red). This gives a surplus of radiation in the tropics and a deficit at high latitudes which in a stable climate has to be compensated by poleward heat transport. b) Total global northward heat transport (solid line), and separated into an ocean (dashed line) and an atmospheric contribution (dashed doted line). From Trenberth and Caron (2001)

1 Scientific background

1.1 Global heat budget

The solar radiation is the fundamental driver of the climate system. Net incoming solar radiation at top of the atmosphere is in the tropics larger than the net outgoing longwave radiation (Fig. 1a). Due to the differential solar heating of earths surface, heat has to be transported from low to high latitudes to compensate for the surplus of net incoming to outgoing radiation in the tropics and the deficit at high latitudes.

Most of the global heat transported into the high latitudes comes from atmospheric transport. The ocean dominates at lower latitudes in the northern hemisphere and diminishes northward (Fig. 1b). Total poleward heat transport peaks around 35° in both hemispheres (Trenberth and Caron, 2001).

In the atmosphere the low-to-high latitude heat transport is through the mean meridional circulation (Hadley cell), stationary eddies (mean state of the planetary waves) and transient eddies (mid-latitude cyclones and anti-cyclones), set up by differential heating of the surface and topography. The Hadley circulation, is of primary importance to the atmospheric heat redistribution in the tropics (Hartmann, 1994). This is due to the potential energy transported polewards aloft which is slightly higher than the latent heat

transported equatorward at the surface. The stationary planetary waves are resulting from zonal variability in topography (e.g., Rocky Mountains and Himalayas) and to a less extent temperature differences between land and ocean. Maximum eddy heat flux is found around the location of the planetary waves, where the storm-tracks are located. The transient eddies are very efficient in mid-latitudes, where they transport both latent and sensible heat (released from the ocean) polewards. The northern hemisphere atmospheric heat transport peaks at 43° N, where there is a heat transport of around 5 PW (1 PW = 10^{15} W). Similar southward heat transports are found at 40° S (Trenberth and Caron, 2001). In the Northern Hemisphere the mean meridional circulation peaks at around 10° N and the total eddy heat transport peaks at around 50° N (Hartmann, 1994).

In the ocean both the surface wind-driven currents (e.g., gyre circulation), the overturning circulation and mid-ocean eddies contributes in the equator-to-pole transport of heat. The latter is assumed to be relatively small, since most of the eddy activity occurs north of the maximum ocean heat transport (Hartmann, 1994). The ocean heat transport dominates the total heat transport in the tropics, from 0–17° N, where the maximum heat transport is found, and has minor contribution north of 45° N compared to the atmosphere (Trenberth and Caron, 2001). The strong western boundary currents (e.g., the Gulf Stream and Kuroshio Current) are located in the region of maximum ocean transport and are responsible for transporting warm water from the tropics to the mid-latitudes, making up the western boundary of the subtropical gyres of the Northern hemisphere. There is a large evaporative heat loss from the ocean to the atmosphere in the mid-latitudes, where dry air descends and cold and dry air flows out from the continents. The density driven meridional overturning circulation is more important for the higher latitudes, even though the relative contribution of the ocean to atmosphere heat transport is low. The two dominant features of the ocean heat transport, the gyre and overturning circulations are closely linked, which makes them difficult to separate.

In the Atlantic ocean, the relative contribution of the ocean heat transport to the atmosphere is larger than for the global average. There is a northward heat transport in the entire basin related to the overturning circulation, which is exclusive for the Atlantic. At 24.5° N the Atlantic ocean heat transport is found to be around 1–1.3 PW (e.g., Lavín et al., 1998; Ganachaud and Wunsch, 2000; Trenberth and Caron, 2001), which is more than half of the total global ocean heat transport at this latitude.

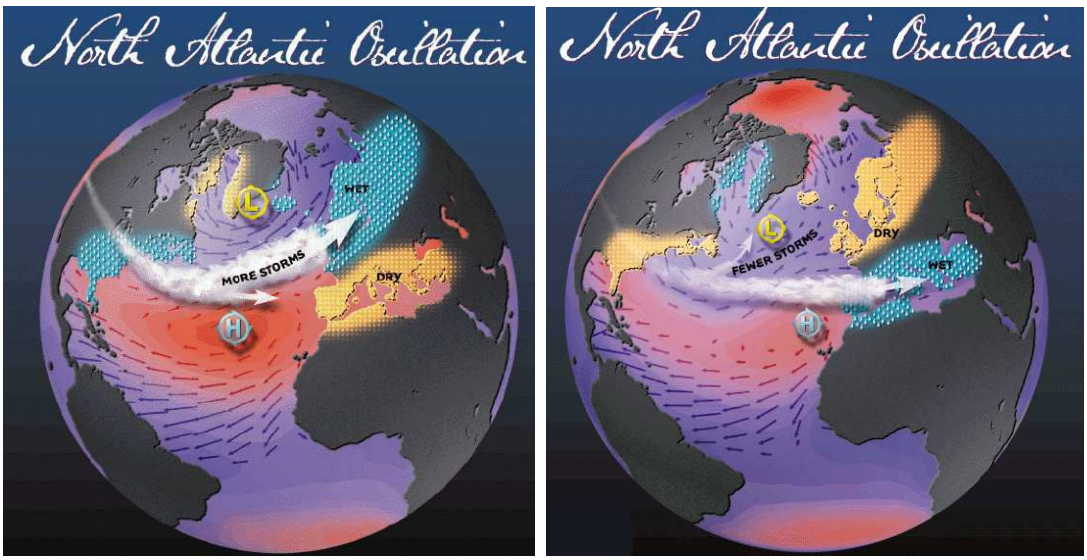

Figure 2: Temperature and precipitation anomalies according to (left) a positive North Atlantic Oscillation index (NAO^+) and (right) a negative NAO index (NAO^-). Source http://www.ldeo.columbia.edu/NAO by Martin Visbeck

1.2 North Atlantic atmospheric variability

1.2.1 North Atlantic Oscillation

The dominant winter atmospheric pattern in the North Atlantic sector is the low pressure system located over Iceland (Icelandic Low) and the high pressure system located in the sub-tropics (Azores High). These two pressure systems fluctuates between a stronger and weaker than normal state, affecting the strength of the westerly winds and storm tracks over the North Atlantic, inducing large changes in surface air temperatures and precipitation over the Atlantic and the adjacent land masses (Hurrell, 1995; Hurrell and Deser, 2009). The oscillation of this pressure pattern is called the North Atlantic Oscillation (NAO; Walker and Bliss, 1932; Wallace and Gutzler, 1981; Barnston and Livezey, 1987; Hurrell, 1995). During a deeper than normal state (NAO^+; Fig. 2a) the westerlies are stronger and more meridional than normal, giving anomalous southerly flow over the eastern United States and more storms into the Nordic Seas and Scandinavia. This results in increased precipitation and temperatures in these regions, while western Greenland, Canadian Arctic and southern Europe experiences dryer and colder than normal conditions. For the opposite phase of the NAO (NAO^-; Fig. 2b) the westerlies are more zonal, and the temperature and precipitation patterns reversed compared to a positive phase.

The NAO has been defined in several different ways, both from direct measurements

and through statistical analysis. From measurements the usual way of defining this index in by taking the normalized winter average sea level pressure (SLP) difference between either Lisbon (Portugal), Ponta Delgada (Azores) or Gibraltar, representing the Azores high, and Iceland (Stykkisholmur/Reykjavik), representing the Icelandic low (Rogers, 1984; Hurrell, 1995; Jones et al., 1997). A similar pattern also shows up by means of point correlations between variations in a reference position and all other geographical locations (e.g., Wallace and Gutzler, 1981).

For the statistical approach, a leading empirical orthogonal function (EOF) of the wintertime (December-March) SLP over the Atlantic basin (20°–80° N, 90° W–40° E; Barnston and Livezey, 1987; Hurrell, 1995) or over the entire northern hemisphere (usually called Arctic Oscillation, AO; Thompson and Wallace, 1998) is used. The NAO in this way accounts for approximately a third of the variability in the SLP time series (Hurrell et al., 2003). The NAO pattern is not stationary in time, giving rise to the two other modes of variability described below.

1.2.2 East Atlantic Pattern

The second dominant mode of the sea level pressure is called the East Atlantic Pattern (EAP; Wallace and Gutzler, 1981; Barnston and Livezey, 1987), and represents the north-south migration of the NAO pattern (Woollings et al., 2010). This pattern consists of an anomaly in the north-eastern North Atlantic, between the centers of action in the NAO. A positive EAO represents a northward shift in the NAO pattern, affecting the placement of the westerlies, and has been associated with more zonal winds (Woollings et al., 2010). This gives increased precipitation and temperatures over western Europe due to more storms hitting this region (Seierstad and Stephenson, 2011).

1.2.3 Scandinavian Pattern

The third dominant mode of the sea level pressure is the Scandinavian Pattern, also called the Eurasian pattern (Wallace and Gutzler, 1981), Eurasian type 1 pattern (Barnston and Livezey, 1987) and blocking pattern (Hurrell and Deser, 2009). In its positive phase this pattern is identified by a high pressure anomaly over Scandinavia and a low pressure anomaly over Greenland. This indicates an east-west shift in the northern center of action in the NAO pattern, and is another manifestation of the non-stationarity of the NAO/AO pattern (Tremblay, 2001). Teleconnection patterns of temperature and

precipitation are also found in relation to this pattern. There is a negative correlation between the Scandinavian Pattern and the precipitation over Siberia and Scandinavia, and a positive correlation over continental Europe, because the blocking high pressure system forces the cyclones towards the European continent in climate models (Bueh and Nakamura, 2007; Haugen and Iversen, 2008).

1.3 North Atlantic ocean circulation

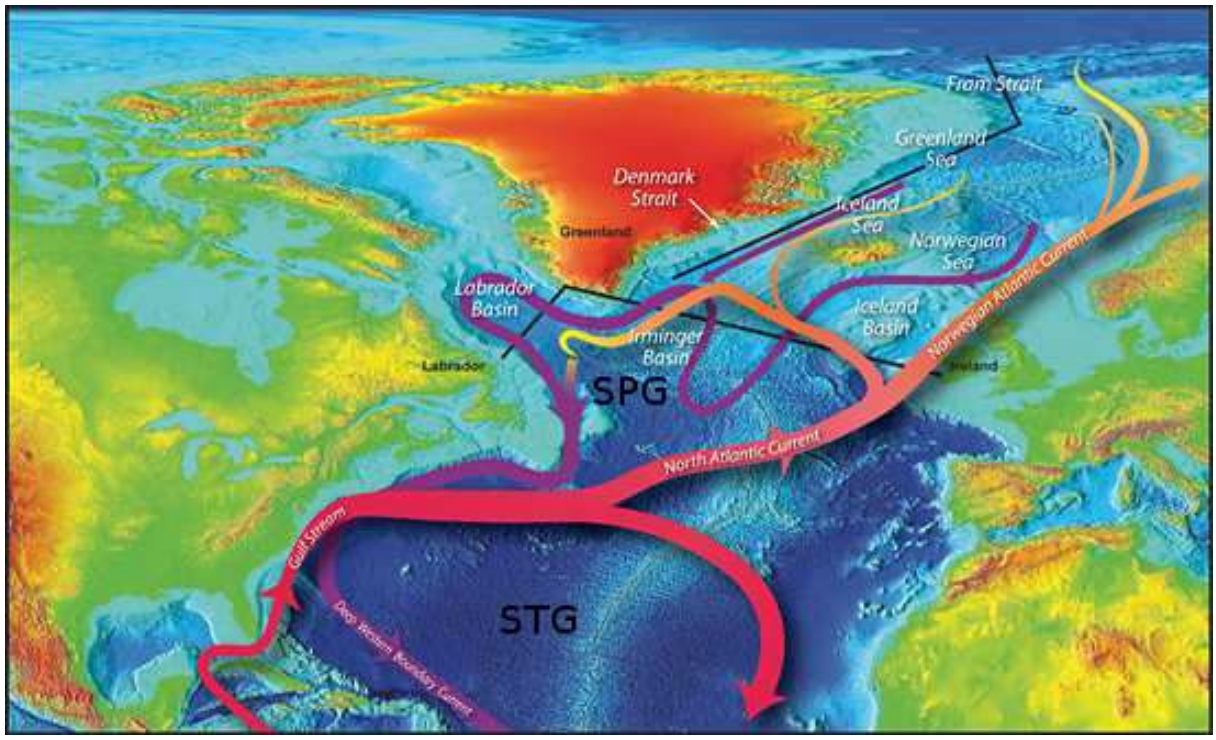

Figure 3: Map of the North Atlantic and Nordic Seas circulation, showing the Subtropical (STG) and the Subpolar (SPG) gyres. Pink indicates warm surface currents and purple indicates cold deep currents. Illustration by Jack Cook, WHOI

The North Atlantic ocean circulation is dominated by the existence of two wind- and density driven gyres (Fig. 3); the anti-cyclonic Subtropical Gyre (STG) and the cyclonic Subpolar Gyre (SPG). The STG includes the Gulf Stream, which breaks off from the eastern coast of North America at Cape Hatteras, continuing easterly and crossing the North Atlantic basin. This flow is split into two parts, one turning south and connecting with the North Atlantic Equatorial Current, and thus closing the large-scale circulation of the STG. The second part, continues northward as the North Atlantic Current (NAC),

situated between the STG and the SPG. Again, this flow splits into two parts, one continuing westward south of the Greenland-Scotland Ridge as the Irminger Current, and the other crossing the GSR where it turns into the Norwegian Atlantic Current (NwAC) and circulates in the Nordic Seas and Arctic basin. The East Greenland Current (EGC) exits the Nordic Seas through the Denmark Strait, meets the southern branch of the NAC south of the ridge, and continues into the Labrador Sea. The Labrador Current, coming from between Canada and Greenland, completes the SPG circulation on the western side.

1.3.1 Atlantic Meridional Overturning Circulation

The Atlantic Meridional Overturning Circulation (AMOC) is the zonally and depth integrated meridional velocity in the Atlantic Ocean. The Atlantic Ocean is characterized by net northward flow of surface water at all latitudes. These partly wind and partly density driven currents are the upper limb of AMOC. As the warm and saline water flows northwards it loses heat to the atmosphere, cools and sinks due to instabilities in the water column (the processes are discussed in more detail in Sect. 1.3.3). The resulting cold and dense deep water flows back toward south as North Atlantic Deep Water (NADW). Eventually, the deep water is gradually brought back to the surface through low-latitude diapycnal mixing and through wind-driven upwelling in the southern ocean (Kuhlbrodt et al., 2007), closing the upper loop. Below the upper circulation cell is a weaker reversed cell of Antarctic Bottom Water (AABW), formed in the Southern Ocean. The AABW flows northward along the bottom in the Atlantic Basin gradually mixing with the southward flowing NADW above (e.g., Ganachaud and Wunsch, 2000; Johnson, 2008).

On longer time scales AMOC is driven by energy input from winds and tides, which gradually mixes the deep and dense water with the lighter water above (Munk and Wunsch, 1998; Wunsch, 2002; Kuhlbrodt et al., 2007). Without this energy input, there would only be a shallow upper ocean circulation cutting off the deep ocean from the surface waters within the order of thousand years (Munk and Wunsch, 1998). The variability in the strength of AMOC on decadal to multidecadal scales are found to be due to dense water production at high latitudes (Kuhlbrodt et al., 2007).

The dense water production associated with AMOC is important in ventilating the deep oceans, where the surface waters remove atmospheric CO_2 and stores it in the deep ocean or in marine sediments. The Atlantic Ocean is responsible for around 41% of the global CO_2 uptake, and most of this occurs in the convective regions (Feely et al., 2001).

Another important aspect of the AMOC is the effect it has on the marine ecosystems, where a simulated weakening of the AMOC resulted in reduced primary production. The reason was a shoaling of the mixed layer and a stronger stratification, resulting in a reduction of available nutrients (Schmittner, 2005).

The temporal and spatial resolution of the observed AMOC is very sparse. Transatlantic hydrographic sections have been taken in 1957, 1981, 1992, 1998 (Fuglister, 1960; Roemmich and Wunsch, 1985; Parrilla et al., 1994; Baringer and Molinari, 1999), and since 2004 there have been more or less continuous measurements (Srokosz, 2004) around 23–26.5° N. These measurements have been used to estimate long-term values for the meridional transports of heat and volume across the various sections in the Atlantic (Roemmich and Wunsch, 1985; Lavín et al., 1998; Bryden et al., 2005; Cunningham et al., 2007).

Based on hydrography, present-day annual mean estimates from 24° and 48° N suggest an AMOC strength of between 13 and 19 Sv (1 Sv = 10^6 m^3 s^{-1}) (Ganachaud and Wunsch, 2000; Ganachaud, 2003; Lumpkin and Speer, 2003), and from estimates of NADW formation rates a strength of around 17–18 Sv (Smethie and Fine, 2001; Talley et al., 2003), with an error estimate of ± 3–5 Sv. Observations from hydrographic sections at 26.5° N taken in the period 2004-2005, show year-long average overturning of 18.7 ± 5.6 Sv, but with large intra-annual variability of between 4 and 34.9 Sv (Cunningham et al., 2007).

1.3.2 Subpolar Gyre

The SPG is a dominant feature of the subpolar North Atlantic Ocean, as the exchange of warm and saline subtropical water with the cold and fresh polar water from the Nordic Seas and Canadian Archipelago occurs in this region. At depth, the circulation in the SPG consists of the lower NADW originating from the Nordic Seas, and the upper NADW from the Irminger and Labrador seas. These deep currents follow the bathymetry, exiting the Labrador Sea as the Deep Western Boundary Current (Schott and Brandt, 2007).

The strength and extension of the gyre is found to influence on the amount and properties of the Atlantic water going into the Nordic Seas. When the gyre is stronger than normal, it has a more east-west extension, resulting in a relative larger fraction of SPG water (colder and less saline) flowing into the Nordic Seas. For a weaker than normal gyre, more subtropical water (warm and saline) flows into the Nordic Seas due to a contraction of the gyre circulation (Hátún et al., 2005).

The large scale atmospheric circulation has a profound influence on the strength and the dynamics of the SPG through the surface wind driven currents and air-sea fluxes resulting in deep water formation (Curry et al., 1998; Häkkinen and Rhines, 2004; Böning et al., 2006).

1.3.3 Deep convection in the North Atlantic

Three regions of deep water formation are found in the high northern latitudes, in the Nordic Seas, in the Labrador Sea and in the Irminger Sea. In these regions the warm northward flowing Atlantic water is transformed into cold and dense water through processes such as diapycnal mixing near steep topography, large-scale open ocean convection, baroclinic instability in convective sites, subduction in colliding currents, and convection on the Arctic shelves (Meincke et al., 1997; Spall and Pickart, 2001).

The Nordic Seas dense water formation has been proposed to be due to open ocean convection mainly in the Greenland Sea during a negative NAO phase (Dickson et al., 1996), dense water produced on the Arctic shelves, and convection due to gradual heat loss as the water circulates the rim of the Nordic Seas and the Arctic ocean (Mauritzen, 1996; Meincke et al., 1997; Rudels et al., 1999; Hansen and Østerhus, 2000; Eldevik et al., 2009).

In the Labrador Sea, the convection is mainly a result of strong wintertime air-sea fluxes, where cold and dry air masses blowing out from the Canadian land masses results in large heat loss (Bumpke et al., 2002; Moore and Renfrew, 2002). The enhanced fluxes has been attributed to a positive phase of the NAO, associated with more of the cold polar air-masses from the north (Dickson et al., 1996).

In the Irminger Sea, the heat loss is normally much less than for the Labrador Sea due to less exposure to the Canadian air masses. Here the Greenland tip jet is found to be the main reason for the open ocean convection (Pickart et al., 2003). The tip jet is an occurrence of strong low-level winds east of Cape Farewell due to high-level northwesterly winds descending orographically east of Greenland, accelerating and drawing cold air over the Irminger sea.

1.4 Atlantic Multidecadal Oscillation

Bjerknes (1964) studied both the year-to-year and decadal variability of the North Atlantic

sea surface temperatures (SST) in relation to the Atlantic sea level pressure changes indicated by the NAO (Sect. 1.2.1). On interannual time scales the SSTs were found to respond to local atmospheric forcing, where increased westerlies (NAO^+) result in larger heat loss from the ocean and reduced temperatures in the entire basin (37.5°–61.5° N). In contrast, the decadal SST variability was found to be driven by changes in the ocean circulation, associated with the Gulf Stream and North Atlantic Current (i.e., gyre circulation) which dominated over the air-sea fluxes from the atmospheric forcing. On decadal time scales the decreased SSTs are only found in a sector between 50°and 60° N during a positive phase of the NAO.

From observations and paleo-proxies the North Atlantic basin scale temperatures have been found to vary on 50–80 year time scales (Schlesinger and Ramankutty, 1994; Delworth and Mann, 2000). The basin scale averaged Atlantic SST variability has been named the Atlantic Multidecadal Oscillation (AMO; Kerr, 2000). Several different definitions have been suggested for this index, e.g., annual mean SST in the North Atlantic region enclosed by 40°–60° N, 50°–10° W (Latif et al., 2004), 0°–60° N, 75° W–7.5° E (Sutton and Hodson, 2005), and EOF analysis of the North Atlantic sea surface temperatures (Kravtsov and Spannagle, 2008), but the various indices all show this low-frequency variability.

Most studies have suggested that these temperature variations are due to changes in the ocean circulation, either the gyre circulation as in Bjerknes (1964), or most often to be connected to the AMOC (Delworth and Mann, 2000; Latif et al., 2004; Knight et al., 2005). A proposed mechanism for this relationship includes variations in the meridional heat and salt transports causing the basin scale fluctuations in SST (e.g., Delworth and Mann, 2000; Latif et al., 2004; Knight et al., 2005). Other studies have suggested that both the solar radiation and volcanoes contribute in setting the phase of the AMO variability (Hansen et al., 2005; Otterå et al., 2010).

Due to the potential great impact of the heat transport on the high-latitude climate AMOC has recently come more into focus. From paleo-records, abrupt climate changes including biomass production or Arctic sea ice cover (Heinrich events, Heinrich, 1988, and Dansgaard-Oeschger events, Dansgaard et al., 1993) in and around the North Atlantic have been linked to periods of abrupt "shutdown" (rapid weakening) of the AMOC (Broecker et al., 1985; Alley, 2007), indicating the potential impact in a large change in AMOC. In a hosing experiment, where a "shutdown" of AMOC is induced by artificially adding a freshening of the surface layer in the North Atlantic, Vellinga and Wood (2002) found that the much of the northern hemisphere was cooled, with local maximum of 8° C

in the North Atlantic the first decade after the collapse. In a pre-industrial control simulation the annual mean European surface air temperatures were found to be around 0.5° C lower for weak than strong AMOC (Pohlmann et al., 2006). Associated with a strong compared to weak AMOC, more precipitation was found over northern Europe and less over southern and eastern Europe.

2 Motivation for the study

Since the onset of the industrial revolution, the anthropogenic release of greenhouse gases into the atmosphere have continued to rise, giving a gradual global temperature increase, estimated to reach up to 2–4.5° C above pre-industrial level by the end of this century (IPCC, 2007). To be able to identify and predict how the excess of greenhouse gases will affect the regional climate and the development of the North Atlantic climate from time scales of decades and beyond, it is a prerequisite to know how the coupled climate system varies internally, and how this relates to both surface and overturning circulation.

From a model intercomparison, the AMOC is expected to be reduced by as much as 30% over this century and perhaps 50% from a quadrupling of the atmospheric CO_2 consentration (Gregory et al., 2005). This is found to be due to changes in the heat flux in the convective regions rather than changes in the freshwater flux. There is at present no observations indicating that this reduction is currently taking place (Cunningham and Marsh, 2010). Since the overturning circulation is strongly connected to the meridional heat transport in the ocean, the projected weakening might have a strong impact on temperatures and sea ice in the high northern latitudes. This heat transport is found to play a significant role in the warming the western European continent (Pohlmann et al., 2006).

Due to the temporal and spatial sparsity of observation of AMOC, it is not possible to assess the potential impact on the Atlantic SSTs (AMO) based on observations. If such relationships can be found, century long time series of observations from paleo-records can be used for reconstruction of past circulation and there will be a tool for monitoring the state of the overturning.

This thesis addresses the role of the North Atlantic ocean circulation on the Atlantic climate variability using a conceptual model, the full range of IPCC AR4 ocean-atmosphere general circulation models, a multi-century control simulation with the Bergen

Climate Model, and observations. The main objectives of this work are to investigate

- To which extent coupled general circulation models are able to capture the observed mean state and variability of the North Atlantic Ocean (Papers I, II, III)

- The potential for climate prediction based on the relationship between AMO and AMOC (Paper I)

- The mechanisms behind natural variability in the North Atlantic climate (Paper II, III)

- The heat transport and air-sea fluxes associated with water mass transformation and deep convection in the North Atlantic (Papers II, III)

Increased understanding of the natural North Atlantic climate variability will be useful for climate predictions on inter-annual to decadal time scales, and for assessing model uncertainties and discrepancies in both reconstruction of the past and for future climate projections. Feedback processes involving sea ice and ocean processes are likely to be key players in the North Atlantic climate variability. Increased knowledge of the relative role of natural versus anthropogenic effects on climate variability will influence upon how we understand present day climate, to which extent we can predict the climate system on seasonal to decadal time scales ahead, and on our ability to assess future climate including extremes.

The 600-year simulation with the Bergen Climate Model (BCM) is a state-of-the-art model tool to identify more clearly the regions of deep convection through diapycnal mixing. In contrast to earlier studies, the convection in the model is directly diagnosed, and also shelf processes are captured. This is not the case by using the traditional approach of mixed layer depth as an indicator of where the North Atlantic Deep Water is produced. Due to the length of the simulation, it is possible to study low-frequency variability that is not possible to do in observations due to limited length of the time series. In addition to the improved convection scheme, the isopycnic coordinate ocean model component making this model well suited both for studying the processes contributing to convection and to track the flow of the resulting water masses to see what effects the deep flow has on the dynamics of the SPG.

3 Summary of Results

The thesis is presented in three scientific papers which focus on processes driving the low-frequency variability of the Atlantic overturning circulation and the potential responses of the surface circulation and climate. The manuscripts included in the thesis are listed below.

- **Paper I: North Atlantic 20th century multidecadal variability in coupled climate models: Sea surface temperature and ocean overturning circulation**
  Medhaug, I. and T. Furevik (2011)
  Ocean Science Discussions, **8**: 353-396, doi: 10.5194/osd-8-353-2011

- **Paper II: Mechanisms for multidecadal variability in a simulated Atlantic Meridional Overturning Circulation**
  Medhaug, I., H. R. Langehaug, T. Eldevik and T. Furevik (2011)
  Climate Dynamics, (submitted)

- **Paper III: Arctic/Atlantic exchanges via the Subpolar Gyre**
  Langehaug, H. R., I. Medhaug, T. Eldevik and O. H. Otterå (2011)
  Journal of Climate, (submitted)

A comprehensive study of the connection between AMO and AMOC is given in Paper I, where the full suite of Intergovernmental Panel on Climate Change (IPCC) Fourth Assessment Report (AR4) models simulating the present day climate are analyzed. All models show most variability on multidecadal timescales for both AMO and AMOC, but with a large intermodel spread in both temperature variability and preferred periodicities. The models are generally not able to reproduce the timing of the observed warm and cold periods in the North Atlantic temperature record, however they are able to reproduce the pattern of temperature variability associated with the warm and cold periods. This indicates that the observed early 20th century extremes, the warm 1930s-50s and cold 1960s-80s, are mainly due to natural variability in the climate system, rather than externally forced. For more than half of the models the AMOC strength is within the range of observational-based estimates, where for a stronger AMOC higher sea surface temperatures and a slightly reduced North Atlantic sea ice cover is found. For all ten models with a realistic AMOC strength, AMOC was found to lead AMO. Individual models show

potential for decadal prediction based on the relationship between the AMO and AMOC, but the models strongly disagree both in phasing and strength of the covariability. This makes it difficult to identify common mechanisms driving the variability in AMO, and to assess the applicability for predictions.

Papers II and III are more mechanistically exploring processes that are driving the multidecadal variability in both the horizontal and overturning circulation in the North Atlantic, using a 600-year pre-industrial climate simulation with the Bergen Climate Model. Deep water formation is found both in the Labrador Sea and in the Nordic Seas. The deep water originating in the Labrador Sea accounts for approximately 1/3, and the Nordic Seas, together with water entrained into the dense overflows south of the Greenland-Scotland Ridge (GSR), accounts for around 2/3 of the deep water formed in the North Atlantic. Together these two deep water sources make up the North Atlantic Deep Water and the lower limb of AMOC. The variability in the Labrador Sea and the Nordic Seas convection is driven by air-sea fluxes in the convective region that can be related to opposite phases of the North Atlantic Oscillation. The Labrador Sea convection is directly linked to the variability in AMOC. Linkages between convection and water mass transformation in the Nordic Seas are more indirect since the GSR forms a continuous barrier inhibiting direct access for the Nordic Seas deep water to the North Atlantic. The Scandinavian Pattern, the third mode of atmospheric variability in the North Atlantic, is a driver of the oceanic poleward heat transport (PHT) over the GSR, the overall constraint on northern water mass transformation. Increased PHT is both associated with an increased water mass exchange across the GSR, and a stronger AMOC.

The mean state of the North Atlantic compares favorably with observations. The model has very realistic ocean transport and well represented water mass distribution feeding into the SPG region. The deep water originating from the Labrador Sea and the Nordic Seas affects the strength of the SPG. Both an increase in the dense overflow from the Nordic Seas and the amount of deep water from the Labrador Sea leads to a spinup of the SPG, but the amount of Labrador Sea Water additionally induce a strengthening in the North Atlantic Current. Around half of the low-frequency variability of the SPG can be explained by the overflow, the Labrador Sea Water, and the East Atlantic Pattern, the second mode of the North Atlantic sea level pressure. The EAP is strongly related to the wind stress in the SPG region.

4 Conclusions and Perspectives

The main conclusions of this study can be summarized in four points:

1) The models used in this study are in general able to reproduce the observed mean state and variability of the North Atlantic climate.

2) Amongst the IPCC model simulations there are some models that show a potential for climate prediction based on the relationship between AMO and AMOC, but the models strongly disagree on the strength and phasing of the relationship, making it difficult to find a common mechanism for variability in the two variables

3) The variability in the flow of deep water masses feeding into the SPG, together with atmospheric variability associated with the East Atlantic Pattern, the second mode of North Atlantic sea level pressure variability, can explain more than half of the decadal variability in the SPG strength, where a positive anomaly in the forcing results in an increased of the SPG strength.

4) The low-frequency natural variability of AMOC in the Bergen Climate Model is mainly driven by the atmospheric forcing at the high latitudes of the North Atlantic, where NAO is contributing to the convection both in the Nordic Seas and Labrador Sea, while the water mass exchange on the GSR is driven by winds associated with the Scandinavian Pattern, the third mode of North Atlantic sea level pressure variability.

A comprehensive summary of the conclusions is found in the respective sections of the papers.

Depending on whether the projected future Arctic warming is due to heat transport in the ocean or in the atmosphere, or whether it is primarily due to ice albedo feedback, this has a large potential consequence for future AMOC. The results from Paper II indicate that if the Arctic warming is due to oceanic heat transport into the Nordic Seas the potential is actually there for an increase in the deep overflows even though the deep convection decreases. By reducing the convection in the boundary current as the water circulates the Nordic Seas, only the dense water which ends up below the sill depth of the GSR is reduced.

This thesis has mainly focused on data from climate models to study the natural variability of the climate system. Although far from perfect, these models are essential in understanding the complex system. Since the models give such diverging results (e.g., Paper I), we need to assess the quality of the models by understanding what makes

the differences. The air-sea fluxes are seemingly important in the deep water formation process, but coarse resolution models have difficulties in giving a good representation of the resulting dense overflows across the GSR. Sub-grid scale processes, i.e., eddy transport, are dynamically important for processes that has been studied in this work, something which has to be resolved to get a more realistic representation and to make us more confident that this is valid in nature. There are several processes that will never be resolved in a Global General Circulation Model, turbulent mixing, such as entrainment, and cloud physics important in determining the effect of clouds or change in cloud type on the radiative forcing in a warmer climate. But we still see this work as one step towards the goal of better understanding of, and better methods for predicting, North Atlantic climate variability.

References

Alley, R. B. (2007). Wally was right: Predictive ability of the North Atlantic "conveyor belt" hypothesis for abrupt climate change. *Annu. Rev. Earth Planet. Sci.*, 35:241–272.

Baringer, M. O. and Molinari, R. (1999). Atlantic ocean baroclinic heat flux at 24 to 26°N. *Geophys. Res. Lett.*, 26:353–356.

Barnston, A. G. and Livezey, R. E. (1987). Classification, seasonality and persistence of low-frequency atmospheric circulation patterns. *Mon. Wea. Rev.*, 115:1083–1126.

Bjerknes, J. (1964). Atlantic air-sea interaction. In Landsberg, H. E. and Van Mieghem, J., editors, *Advances in Geophysics*, pages 1–82. Academic press.

Böning, M., Scheinert, M., Dengg, J., Biastoch, A., and Funk, A. (2006). Decadal variability of subpolar gyre transport and its reverberation in the North Atlantic overturning. *Geophys. Res. Lett.*, 33:L21S01.

Broecker, W. S., Peteet, D. M., and Rind, D. (1985). Does the ocean-atmosphere system have more than one stable mode of operation? *Nature*, 315:21–26.

Bryden, H. L., Longworth, H. R., and Cunningham, S. A. (2005). Slowing of the Atlantic meridional overturning circulation at 25°N. *Nature*, 438:655–657.

Bueh, C. and Nakamura, H. (2007). Scandinavian pattern and its climatic impact. *Q. J. R. Meteorol. Soc.*, 133:2117–2131.

Bumpke, K., Karger, U., and Uhlig, K. (2002). Measurements of turbulent fluxes of momentum and sensible heat over the labrador sea. *J. Phys. Oceanogr.*, 32:401–410.

Cunningham, S. A., Kanzow, T., Rayner, D., Baringer, M. O., Johns, W. E., Marotzke, J., Longworth, H. R., Grand, E. M., Hirschi, J. J.-M., Beal, L. M., Meinen, C. S., and Bryden, H. L. (2007). Temporal variability for the Atlantic Meridional Overturning Circulation at 26.5°N. *Science*, 317:935–937.

Cunningham, S. A. and Marsh, R. (2010). Observing and modeling changes in the Atlantic MOC. *Wiley Interdiscip. Rev.: Climate Change*, 1:180–191. doi: 10.1002/wcc.22.

Curry, R., McCartney, M., and Joyce, T. (1998). Oceanic transport of subpolar climate signals to mid-depth subtropical waters. *Nature*, 391:575–577.

Dansgaard, W., Johnsen, S. J., Clausen, H. B., Dahl-Jensen, D., Gundestrup, N. S., Hammer, C. U., Hvidberg, C. S., Steffensen, J. P., Sveinbjörnsdottir, A. E., Jouzel, J., and Bond, G. (1993). Evidence for general instability of past climate from a 250-kyr ice-core record. *Nature*, 364:218–220.

Delworth, T. L. and Mann, M. E. (2000). Observed and simulated multidecadal variability in the Northern hemisphere. *Clim. Dynam.*, 16:661–676.

Dickson, R., Lazier, J., Meincke, J., Rhines, P., and Swift, J. (1996). Long-term coordinated changes in the convective activity of the North Atlantic. *Prog. Oceanogr.*, 38:241–295.

Eldevik, T., Nilsen, J. E. ., Iovino, D., Olsson, K. A., Sandø, A. B., , and Drange, H. (2009). Observed sources and variability of nordic seas overflow. *Nat. Geosci.*, 2:406–410.

Feely, R. A., Sabine, C. L., Takahashi, T., and Wanninkhof, R. (2001). Uptake and storage of carbon dioxide in the ocean: The global co_2 survey. *Oceanogr*, 14(4):18–32.

Fuglister, F. C. (1960). *Atlantic Ocean Atlas of temperature and salinity profiles and data from the international geophysical year of 1957-1958*, volume 1 of *Woods Hole Oceanogr Inst Atlas Series*. Woods Hole Oceanographic Institution, Woods Hole, Mass.

Ganachaud, A. (2003). Large-scale mass transports, water mass formation, and diffusivities estimated from World Ocean Circulation Experiment (WOCE) hydrographic data. *J. Geophys. Res.*, 108(C7):3213.

Ganachaud, A. and Wunsch, C. (2000). Improved estimates of global ocean circulation, heat transport and mixing from hydrographic data. *Nature*, 408:453–457.

Gregory, J. M., Dixon, K. W., Stouffer, R. J., Weaver, A. J., Driesschaert, E., Eby, M., Fichefet, T., Husami, H., Hu, A., Jungclaus, J. H., Kamenkovich, I. V., Levermann, A., Montoya, M., Murakami, S., Nawrath, S., Oka, A., Sokolov, A. P., and Thorpe, R. B. (2005). A model intercomparison of changes in the Atlantic thermohaline circulation in response to increased CO2 concentration. *Geophys. Res. Lett.*, 32:L12703. doi: 10.1029/2005GL02309.

Häkkinen, S. and Rhines, P. (2004). Decline of Subpolar North Atlantic circulation during the 1990s. *Science*, 304:555–559.

Hansen, B. and Østerhus, S. (2000). North atlantic-nordic seas exchanges. *Prog. Oceanogr.*, 45:109–208.

Hansen, J., Nazarenko, L., Ruedy, R., Sato, M., Willis, J., Del Genio, A., Koch, D., Lacis, A., Lo, K., Menon, S., Navakov, T., Perlwiz, J., Russel, G., Schmidt, G. A., and Tausenev, N. (2005). Earth's energy imbalance: confirmation and implications. *Science*, 308:1431.

Hartmann, D. L. (1994). *Global Physical Climatology*, volume 56 of *International Geophysics Series*. Academic Press.

Hátún, H., Sandø, A. B., Drange, H., Hansen, B., and Valdimarsson, H. (2005). Influence of the Atlantic Subpolar Gyre on the Thermohaline Circulation. *Science*, 309:1841–1844.

Haugen, J. E. and Iversen, T. (2008). Response in extremes of daily precipitation and wind from a downscaled multi-model ensemble of anthropogenic global climate change scenarios. *Tellus*, 60A:411–426.

Heinrich, H. (1988). Origin and consequences of cycling ice rafting in the Northeast North Atlantic Ocean during the past 130,000 years. *Quat. Res.*, 29(2):142–152.

Hurrell, J. W. (1995). Decadal trends in the North Atlantic Oscillation: Regional temperatures and precipitation. *Science*, 269(5224):676–679.

Hurrell, J. W. and Deser, C. (2009). North Atlantic climate variability: The role of the North Atlantic Oscillation. *J. Mar. Syst.*, 78(1):28–41.

Hurrell, J. W., Kushnir, Y., Ottersen, G., and Visbeck, M. (2003). An overview of the North Atlantic Oscillation. In Hurrell, J. W., Kushnir, Y., Ottersen, G., and Visbeck, M., editors, *The North Atlantic Oscillation: Climatic significance and environmental impact*, Geophysical Monograph Series 134, pages 1–35. American Geophysical Union.

IPCC (2007). *Climate Change 2007: The physical science basis. Contribution of Working Group I to the Fourth Assessment Report of the Intergovernmental Panel on Climate Change*. S. Solomon and D. Qin and M. Manning and Z. Chan and M. Marquis and K. B. Averyt and M. Tignor and H. L. Miller.

Johnson, G. C. (2008). Quantifying Antarctic Bottom Water and North Atlantic Deep Water volumes. *J. Geophys. Res.*, 113:C05027.

Jones, P. D., Tónsson, T., and Wheeler, D. (1997). Extension to the North Atlantic Oscillation using earlier instrumental pressure observations from Gibraltar and south-west Iceland. *Int. J. Climatol.*, 17:1433–1450.

Kerr, R. (2000). A North Atlantic climate pacemaker for centuries. *Science*, 288(5473):1984–1985.

Knight, J. R., Allan, R. J., Folland, C. K., Vellinga, M., and Mann, M. E. (2005). A signature of persistent natural thermohaline circulation cycles in observed climate. *Geophys. Res. Lett.*, 32:L20708.

Kravtsov, S. and Spannagle, C. (2008). Multidecadal climate variability in observed and modelled surface temperatures. *J. Climate*, 21:1104–1121.

Kuhlbrodt, T., Griesel, A., Montoya, M., Levermann, A., Hofmann, M., and Rahmstorf, S. (2007). On the driving processes of the atlantic meridional overturning circulation. *Rev. Geophys.*, 45:RG2001.

Latif, M., Roeckner, E., Botzet, M., Esch, M., Haak, H., Hagemann, S., Jungclaus, J. H., Legutke, S., Marsland, S., and Mickolajevicz, U. (2004). Reconstructing, monitoring, and predicting multidecadal-scale changes in the North Atlantic thermohaline circulation with sea surface temperature. *J. Climate*, 17:1605–1613.

Lavín, A., Bryden, H., and Parrilla, G. (1998). Meridional transport and heat flux variations in the subtropical North Atlantic. *Glob. Atmos. Ocean Syst.*, 6:269–293.

Lumpkin, R. and Speer, K. (2003). Large-scale vertical and horizontal circulation in the North Atlantic Ocean. *J. Phys. Oceanogr.*, 33:1902–1920.

Mauritzen, C. (1996). Production of dense overflow waters feeding the North Atlantic across the Greenland-Scotland Ridge, Part I: Evidence for a revised circulation scheme. *Deep-Sea Res. I*, 43:769–806.

Meincke, J. B., Rudels, B., and Friedrich, H. J. (1997). The arctic ocean nordic seas thermohaline system. *ICES J. Mar. Sci.*, 54(3):283–299.

Moore, G. W. K. and Renfrew, I. A. (2002). An assessment of the surface turbulent heat fluxes from the ncep-ncar reanalysis over the western boundary currents. *J. Climate*, 15:2020–2037.

Munk, W. and Wunsch, C. (1998). Abyssal recipes ii: energetics of tidal and wind mixing. *Deep-Sea Res. I*, 45:1977–2010.

Otterå, O. H., Bentsen, M., Drange, H., and Suo, L. (2010). External forcing as a metronome for atlantic multidecadal variability. *Nat. Geosci.*, 3:688–694. doi: 10.1038/ngeo955.

Parrilla, G., Lavin, A., Bryden, H., Garcia, M., and R., M. (1994). Rising temperatures in the subtropical North Atlantic ocean over the past 35 years. *Nature*, 369:48–51.

Pickart, R. S., Spall, M. A., Ribergaard, M. H., Moore, G. W. K., and Milliff, R. F. (2003). Deep convection in the irminger sea forced by the greenland tip jet. *Nature*, 424:152–156.

Pohlmann, H., Sienz, F., and Latif, M. (2006). Influence of the multidecadal Atlantic meridional overturning circulation variability on European climate. *J. Climate*, 19:6062–6067.

Roemmich, D. and Wunsch, C. (1985). Two transatlantic sections: meridional circulation and heat flux in the subtropical North Atlantic Ocean. *Deep-Sea Res.*, 32:619–664.

Rogers, J. C. (1984). The association between the North Atlantic Oscillation and the Southern Oscillation in the Northern Hemisphere. *Mon. Weather. Rew.*, 112:1999–2015.

Rudels, B., Friedrich, H. J., and Quadfasel, D. (1999). The arctic circumpolar boundary current. *Deep-Sea Res. I*, 46:1023–1062.

Schlesinger, M. E. and Ramankutty, N. (1994). An oscillation in the global climate system of period 65-70 years. *Nature*, 367:723–726.

Schmittner, A. (2005). Decline of the marine ecosystem caused by a reduction in the Atlantic overturning circulation. *Nature*, 434:628–633.

Schott, F. A. and Brandt, P. (2007). Circulation and deep water export of the subpolar North Atlantic during the 1990's. In Schmittner, A., Chiang, J., and Hemmings, S., editors, *Ocean circulation: Mechanisms and impacts*, Geophysical Monograph Series 173, pages 91–118. American Geophysical Union.

Seierstad, I. A. and Stephenson, D. B. (2011). The East Atlantic Pattern and variability of the Atlantic zonal jet. *(Manuscript in preparation).*

Smethie, Jr., W. M. and Fine, R. A. (2001). Rates of North Atlantic deep water formation calculated from chlorofluorocarbon inventories. *Deep-Sea Res. I*, 48:189–215.

Spall, M. A. and Pickart, R. S. (2001). Where does dense water sink? a subpolar gyre example. *J. Phys. Oceanogr.*, 31:810–826.

Srokosz, M. (2004). New experiment deploys observing array in N. Atlantic to investigate rapid climate change. *Eos*, 85(8):78–83.

Sutton, R. T. and Hodson, D. L. R. (2005). Atlantic Ocean forcing of North American and European summer climate. *Science*, 309(5731):115–118.

Talley, L. D., Reid, J. L., and Robbins, P. E. (2003). Data-based meridional overturning streamfunctions for the global ocean. *J. Climate*, 16:3213–3226.

Thompson, D. W. J. and Wallace, J. M. (1998). The Arctic Oscillation signature in the wintertime geopotential height an temperature fields. *Geophys. Res. Lett.*, 25(9):1297–1300.

Tremblay, L. B. (2001). Can we consider the Arctic Oscillation independently from the Barents Oscillation? *Geophys. Res. Lett.*, 28(22):4227–4230.

Trenberth, K. E. and Caron, J. M. (2001). Estimates of meridional atmosphere and ocean heat transports. *J. Climate*, 14:3433–3443.

Vellinga, M. and Wood, R. A. (2002). Global climatic impacts of a collapse of the Atlantic thermohaline circulation. *Clim. Change*, 54(3):251–267. doi: 10.1023/A:1016168827653.

Walker, G. T. and Bliss, E. W. (1932). World weather V. *Mem. Roy. Met. Soc.*, 4:53–84.

Wallace, J. M. and Gutzler, D. S. (1981). Teleconnections in the geophysical height field during northern hemisphere winter. *Mon. Wea. Rev.*, 109:784–812.

Woollings, T., Hannachi, A., and Hoskins, B. (2010). Variability of the North Atlantic eddy-driven jet stream. *Q. J. R. Meteorol. Soc.*, 136:856–868.

Wunsch, C. (2002). What is the thermohaline circulation? *Science*, 298:1180–1181.

Paper I

North Atlantic 20th century multidecadal variability in coupled climate models: Sea surface temperature and ocean overturning circulation

Medhaug, I. and T. Furevik (2011)

Ocean Science Discussions, **8**: 353-396, doi: 10.5194/osd-8-353-2011

North Atlantic 20th Century Multidecadal Variability in Coupled Climate Models: Sea Surface Temperature and Ocean Overturning Circulation

I. Medhaug and T. Furevik
Geophysical Institute and Bjerknes Centre for Climate Research, University of Bergen, Bergen, Norway

Abstract

Output from a total of 24 state-of-the-art Atmosphere-Ocean General Circulation Models is analyzed. The models were integrated with observed forcing for the period 1850-2000 as part of the Intergovernmental Panel on Climate Change (IPCC) Fourth Assessment Report. All models show enhanced variability at multi-decadal time scales in the North Atlantic sector similar to the observations, but with a large intermodel spread in amplitudes and frequencies for both the Atlantic Multidecadal Oscillation (AMO) and the Atlantic Meridional Overturning Circulation (AMOC). The models, in general, are able to reproduce the observed geographical patterns of warm and cold episodes, but not the phasing such as the early warming (1930s–50s) and the following colder period (1960s–80s). This indicates that the observed 20th century extreme in temperatures are due to primarily a fortuitous phasing of intrinsic climate variability and not dominated by external forcing. Most models show a realistic structure in the overturning circulation, where more than half of the available models have a mean overturning transport within the observed estimated range of 13–24 Sverdrup. Associated with a stronger than normal AMOC, the surface temperature is increased and the sea ice extent slightly reduced in the North Atlantic. Individual models show potential for decadal prediction based on the relationship between the AMO and AMOC, but the models strongly disagree both in phasing and strength of the covariability. This makes it difficult to identify common mechanisms and to assess the applicability for predictions.

1 Introduction

The ocean currents transport vast amounts of heat from low to high latitudes by the horizontal wind-driven gyre circulation and the density-driven thermohaline circulation

(THC), with a maximum of ∼2 PW at 17°N (Trenberth and Caron, 2001). In the Atlantic the THC component is known as the Atlantic Meridional Overturning Circulation (AMOC), which in a zonal mean is characterized by a cell of northward flowing warm and saline water in the upper 1000 m, above a southward flowing colder and fresher water down to 3-4000 m. Below there is a deeper reversed cell of Antarctic bottom water (Delworth et al., 2008). The poleward transport of heat in the upper cell is an important driver for the climate system. At high latitudes the ocean is subjected to intense heat loss to the atmosphere and the water therefore loses buoyancy and sinks. The potential energy lost in the sinking process is regained by wind- and tidal mixing across stable stratification further south, and the deep water gradually returns to the surface (Wunsch, 2002). On very long time scales (order of 1000 years) the AMOC is therefore sustained by mechanical energy input through wind- and tidal mixing.

Decadal to multidecadal variability in the North Atlantic climate has been found in a large number of observational studies (e.g., Bjerknes, 1964; Kushnir, 1994; Schlesinger and Ramankutty, 1994; Delworth and Mann, 2000; Polyakov and Johnson, 2000), with two 20th century extremes being the early warming in the 1930s to 1950s, and the subsequent colder period during the 1960s to 1980s. From multimodel analysis of 20th century climate simulations, these temperature extremes have been attributed mainly to the internal variability of the North Atlantic and not to the externally forced responses (Kravtsov and Spannagle, 2008; Knight, 2009; Ting et al., 2009). However, other model simulations indicate that both solar variability and volcanoes contribute in setting the phase of the variability (Hansen et al., 2005; Otterå et al., 2010). The decadal to multidecadal temperature variations observed in the Nordic Seas and the Arctic are seemingly related to the slowly varying SST field further to the south in the North Atlantic (Polyakov et al., 2004), where heat transport variability in both ocean and atmosphere appears to provide the link (e.g., Furevik, 2001). Bjerknes (1964) suggested that the decadal to multidecadal climate variations were driven by slow changes in the ocean gyre circulation, while many later studies indicate that the main cause is variations in the AMOC, driven by density fluctuations in the convection regions. The mechanisms suggested for this relationship include variations in the meridional heat and salt transports causing basin scale fluctuations in surface temperatures known as the Atlantic Multidecadal Oscillation (AMO) (Delworth and Mann, 2000; Latif et al., 2004; Knight et al., 2005), and the effect heat and salinity anomalies have on the density in the convective regions, and hence the strength of the deep water formation (e.g., Delworth et al., 1993; Marshall et al., 2001; Bentsen et al., 2004; Jungclaus et al., 2005; Medhaug et al., 2011).

At present there is no consensus to what degree the AMOC variability is: a pure ocean-only mode or a fully coupled atmosphere-ocean mode, with density fluctuations in the convection regions driven by advection of anomalous dense water from the south (e.g., Delworth et al., 1993; Vellinga and Wu, 2004); a fully coupled atmosphere-ocean or atmosphere-sea ice-ocean mode with the deep water formation rate dominated by variations in the local wind forcing (e.g., Dickson et al., 1996; Häkkinen, 1999; Eden and Willebrand, 2001; Deshayes and Frankignoul, 2008; Msadek and Frankignoul, 2009; Medhaug et al., 2011); or if AMOC is simply a low frequency damped response to fluctuations in the atmospheric forcing fields (Hasselmann, 1976; Frankignoul et al., 1997; Frankcombe et al., 2009).

Low frequency variability in the ocean overturning circulation and possible relations with upper ocean heat content and air-sea interaction of heat and moisture suggest a potential for predicting surface temperature and atmospheric mean state on annual to decadal time scales. Recent works in this rapidly growing research field suggest that AMOC is predictable up to 20 years (Collins et al., 2006). By relaxing the model to observed SSTs (Keenlyside et al., 2008), to upper ocean properties (temperature and salinity) and atmospheric data (Smith et al., 2007), or to hydrographic observations (Pohlmann et al., 2009), the various groups have reported improved prediction skills of both global and regional climate. More precise understanding of the linkages between the hydrographic structure of the ocean, the large scale ocean circulation, and the impacts of variations in the ocean transports on atmospheric climate, will increase our ability to give more realistic decadal forecasts in the years to come.

The temporal resolution of AMOC is sparse, with transatlantic measurements taken only four times during the time period 1957-1997 (Fuglister, 1960; Roemmich and Wunsch, 1985; Parrilla et al., 1994; Baringer and Molinari, 1999), and with continuous measurements only available since 2004 (Cunningham et al., 2007). Due to the extent of the basin-scale circulation long term direct observations of the AMOC have not been conducted as it would require an unrealistic number of sections and instruments. As a result, neither the relationships between the AMO and AMOC in nature, nor the impacts of AMOC on North Atlantic climate variability are known. We therefore have to primarily rely on models in this study.

For the first time the full range of Intergovernmental Panel on Climate Change (IPCC) Fourth Assessment Report (AR4) climate simulations for the 20th century integrations (1850-2000) have been used in a dedicated investigation of the connection between the two variables of North Atlantic multidecadal variability. Our main objectives have been

to investigate to what extent i) the observed AMOC and AMO strength and variability are captured in the climate models, ii) relationships exist between the two measures of multidecadal climate fluctuations, iii) any physical mechanisms behind such relationships can be identified, and iv) century long observations of SST can be used as a proxy for AMOC, and knowledge of the phase of the AMOC therefore will improve our ability to predict climate on interannual to decadal time scales.

Section 2 gives an overview of the modelling and observational data sets used in this study and the applied statistical methods. The results of the model analysis, and comparison with observations, are given in Sect. 3, and the results and their implications discussed in Sect. 4. Section 5 gives a summary with concluding remarks on the implications for predictability of AMO and other climatic variables based on the state of the AMOC.

2 Methods and data

2.1 The coupled models

This study is based on 24 climate simulations provided by 16 modeling groups worldwide (Table 1). Available monthly mean surface temperature (TS), sea ice concentration (SIC) and Atlantic meridional overturning streamfunction (AMOC) data from the scenario "twentieth century climate in coupled models" (20c3m) are used. For most models the scenario 20c3m covers the period 1850-2000. The models have been integrated using observed values of greenhouse gas concentrations and direct effect of sulphate aerosols. For 12 of the models also natural forcing (volcanic aerosols and solar variability) has been included, and for 13 of the models tropospheric and stratospheric ozone. Only four of the models use flux adjustment, CGCM3.1 T47 and T63 (globally), INM-CM3.0 (regionally) and MRI-CGCM2.3.2 (in tropics). The data is the same as used in the IPCC AR4 and is downloaded from the World Climate Research Program's (WCRP's) Coupled Model Intercomparison Project phase 3 (CMIP3) multi-model database.

From the model output the AMO index is defined as the area-weighted SST for 60°W–0°, 0°–60°N, similar to definitions used in earlier works (e.g., Knight et al., 2005; Sutton and Hodson, 2005). For the spatial maps of the multi model mean and their spread, all models are interpolated onto a 2.5°×2.5°grid using exponential kernel smoothing (Gijbels et al., 1999), where weights are decreasing exponentially with distance from the center point of each grid cell. Data from a distance exceeding 600 km are excluded from the

Table 1: List of models that participate in this study.

Modeling groups	IPCC ID	Horizontal Atm. res.	Natural forcing
Bjerknes Centre for Climate Research, University of Bergen, Norway	BCCR-BCM2.0	T63	No
National Center for Atmospheric Research, USA	CCSM3	T85	Yes
Canadian Centre for Climate Modeling & Analysis, Canada	CGCM3.1(T47)	T47	No
	CGCM3.1(T63)	T63	No
Météo-France/Centre National de Recherches Météorologique, France	CNRM-CM3	T63	No
CSIRO Atmospheric Research, Australia	CSIRO-Mk3.0	T63	No
	CSIRO-Mk3.5	T63	No
Max Planck Institute for Meteorology, Germany	ECHAM5/MPI-OM	T63	No
Meteorological Institute of the University of Bonn, Meteorological Research Institute of KMA, and Model and Data group, Germany/Korea	ECHO-G	T30	Yes
LASG/Institute of Atmospheric Physics, China	FGOALS-g1.0	T42	No
NOAA/Geophysical Fluid Dynamics Laboratory, USA	GFDL-CM2.0	2.0°×2.5°	Yes
	GFDL-CM2.1	2.0°×2.5°	Yes
NASA/Goddard Institute for Space Studies, USA	GISS-AOM	3°×4°	No
	GISS-EH	4°×5°	Yes
	GISS-ER	4°×5°	Yes
National Institute of Geophysics and Volcanology, Italy	INGV-SXG	T106	No
Institute for Numerical Mathematics, Russia	INM-CM3.0	4°×5°	Yes
Institute Pierre Simon Laplace, France	IPSL-CM4	2.5°×3.8°	No
Center for Climate System Research, National Institute for Environmental Studies, and Frontier Research Center for Global Change, Japan	MIROC3.2(HI)	T106	Yes
	MIROC3.2(MED)	T42	Yes
Meteorological Research Institute, Japan	MRI-CGCM2.3.2	T42	Yes
National Center for Atmospheric Research, USA	PCM	T42	Yes
Hadley Centre for Climate Prediction and Research/Met Office, UK	UKMO-HadCM3	2.8°×3.8°	No
	UKMO-HadGEM1	N96	Yes

interpolation. The intermodel standard deviation is used as a measure of the level of agreement between the different models, where the mean has been subtracted for the individual model.

In models the AMOC index is usually defined as the maximum Atlantic meridional overturning streamfunction in a zonal band, either chosen at a specific latitude (usually 30°N) or in a latitude band (e.g., north of 20°N), measured in Sverdrup (1 Sv = 10^6 m^3 s^{-1}). Here maximum north of 20°N in the annual streamfunction is used. To exclude surface wind driven overturning we have used the further criteria that the maximum should be located deeper than 500 m (Schott et al., 2004). The meridional stream function is only available for 18 of the models.

The sea ice extent is defined here as the area where the sea ice concentration equals or exceeds 15%. The sea ice is regridded into a 2.5°×2.5°grid using the same interpolation method as given above.

2.2 Observations

In order to compare the model performance with observations, gridded time series of SST on a 5°latitude by 5°longitude grid (Kaplan SST V2, see Kaplan et al., 1998) are used. These time series are provided by the Climate Diagnostics Center, Boulder, Colorado, USA, from their Web site at http://www.cdc.noaa.gov/ on a monthly global field from 1856 to present.

From observations the AMO index is found in the same manner as from models. For AMOC no exact measurements or estimates exists. However, the AMOC strength is a measure of the net northward transport in the upper ocean, or to a good approximation net southward transport at depth (e.g., Ganachaud and Wunsch, 2000; Talley et al., 2003). Due to the Bering Strait through flow (Woodgate et al., 2005) the latter definition is slightly larger than the former.

2.3 Statistical methods

A one-sided adaptively weighted multitaper method is used to make power spectral densities for the AMOC and AMO indices (Thompson, 1982). The seasonal cycle and the linear trend in the time series are removed from the monthly values prior to the analysis. The power spectrum of the red-noise spectra is computed from the first order autoregressive (AR(1); e.g., Bartlett, 1966) process for the individual time series.

In order to remove high frequency variability, time series are filtered using a 15 year running binomial filter. Compared to standard running mean this filter to a large extent remove spectral leakage in the filtered time series.

To investigate statistical significance of the lagged correlation (at 5% level), a two sided t-test has been used with the estimated effective degrees of freedom, N_e. This is calculated from the formula of Quenouille (1952); $N_e = N/(1 + 2r_a^1 r_b^1 + 2r_a^2 r_b^2)$, where N is the number of data points in the time series, r_a^1 and r_b^1 are the autocorrelations at lag one, and r_a^2 and r_b^2 the autocorrelations at lag two for time series a and b, respectively.

3 Simulated AMO and AMOC variability

3.1 AMO

The spatial pattern of the sea surface temperature (SST) field associated with the AMO index is shown in Fig. 1. In the observations there is an overall high positive correlation

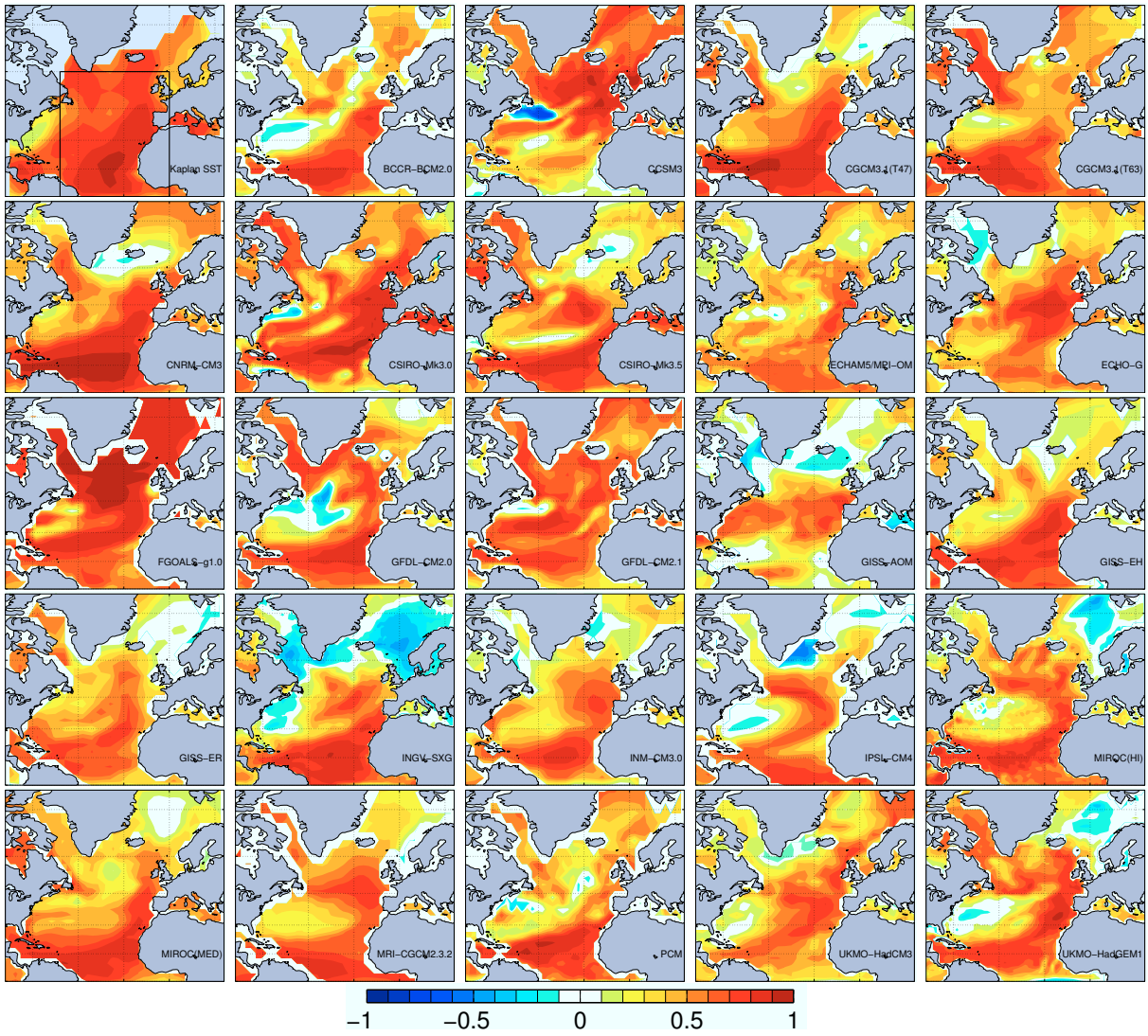

Figure 1: The correlation between the local SST and the AMO index in the observations (upper left panel) and in the 24 models. The gray shading over ocean means too few observations. The AMO is defined as the average SST inside the black box shown in the first plot. The time series are filtered with a 15 year running binomial filter to remove the high frequency variability and the linear trends are removed prior to the correlation

between the SST and the AMO index for the entire AMO region (shown as square box in the first plot). A region with reduced correlation is seen in the Gulf Stream area and in the Nordic Seas. Most models also show a region of reduced or slightly negative correlation along the North American coast, but for some models this region is shifted slightly north or is distributed over a larger area. Some of the models show polar amplifications of the AMO signal. This is not seen in the observations here due to the lack of data, but has been identified in earlier papers (e.g., Polyakov et al., 2004). Both observations and the

majority of models show the strongest correlation between SST and the AMO index in the tropical Atlantic. North of 30°N the models are more varying.

a)

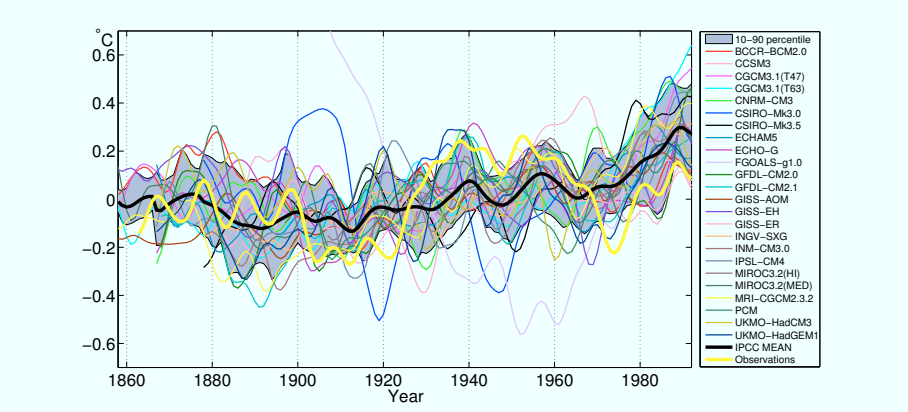

b)

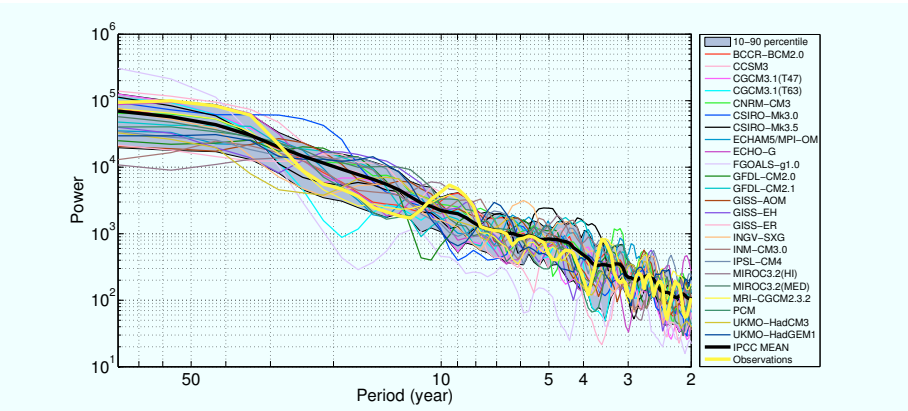

Figure 2: a) The annual mean AMO index in the different models (thin lines) and observations (thick yellow line) relative to the mean of 1901–80. The black thick line shows the ensemble mean and the gray band shows the 10–90 percentile of the model spread. All curves are filtered by a 15 year running binomial filter. The units are given in °C. b) Smoothed power spectrum of the monthly mean AMO. The linear trends are removed and the time series are normalized for different models prior to the analysis. The colours are the same as in (a)

The AMO index for the different models are shown in Fig. 2a. The mean of the period 1901–80 has been removed form the models. FGOALS-g1.0 starts from a relative warm state, in contrast to the other models and observations. The model has yet to reach a stable equilibrium, and the model has therefore been omitted from the ensemble mean in this figure.

The individual models (thin lines) show highly varying amplitudes, but all models do show a warming in the last two decades when anthropogenic warming becomes influential (IPCC, 2007). Compared to the observations (thick yellow line), the ensemble mean (thick black line) shows much less variability. This is to be expected from an average of many independent realizations. For most years the observations are nevertheless reproduced by the model spread, here shown as the 10–90 percentile (gray band). The two main discrepancies between the model spread and the observations are during the mid century warming (1930s–50s) where the models underestimate the warming, and during the subsequent cold period (1960s–80s) when the models are generally too warm. This could be due to errors in the observed time series, inadequacy in the modelled response to the external forcing or forcing that is not included in the simulation, or due to timing of the internal/natural variability in the models compared to observations.

Figure 2b shows the power spectra for the AMO index. The observations have two bands of increased power, one at multidecadal time scales (above ∼30 years) and one around 10 years, both being above the level of red noise. Due to varying autocorrelation at lag one for the models and observations, the individual red-noise spectra are not shown. The interannual-decadal power maximum in observations is likely the imprint of the North Atlantic Oscillation on the SST, as this atmospheric mode does show enhanced power at these time scales (Furevik et al., 2003; Hurrell et al., 2003). Most models also show maximum power at multidecadal time scales but with too weak amplitudes compared to the observations. The observed maximum at around 10 years is not captured by the models.

The persistence in the modelled AMO index, defined as the maximum time lag before the autocorrelation function first crosses the significance line at 5% level (Fig. 3), varies from 1 and up to 25 years (Table 2). This indicates the potential for predicting future SSTs based on persistence. For the observations the equivalent persistence time scale is 11 years.

In order to check to what extent the models are able to reproduce the observed warming and cooling patterns, composites of 15 warm years minus 15 cold years are made. Since the models are not able to reproduce the timing of the observed extremes, the simulated warm periods have been selected where the 15 year average temperature in each simulation is at its maximum, and the subsequent modelled cold period is then subtracted (Table 2). Due to the anthropogenic warming signal adding to the amplitude of the SST variability towards the end of the time series, warm periods after 1980 have been omitted. FGOALS-g1.0 does not have any distinct warm or cold 15 year periods, hence it is omitted from

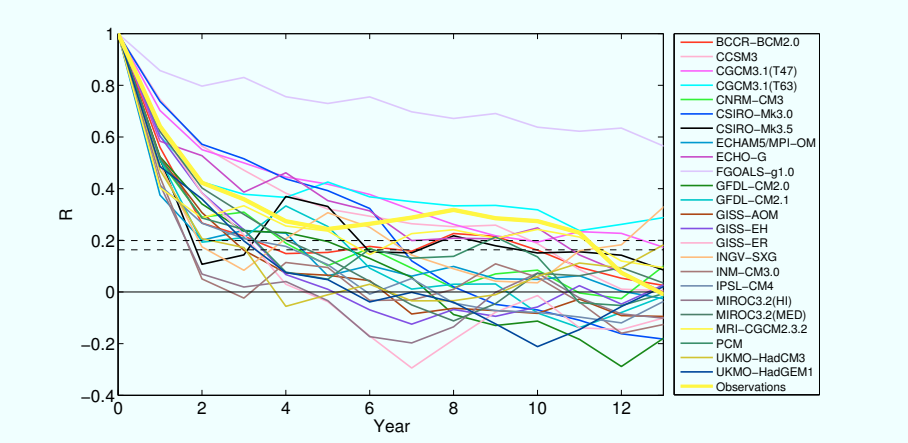

Figure 3: Autocorrelation function for the annual mean values of the AMO index in the different models (thin coloured lines), and for the observations (thick yellow line) to estimate the persistence in the time series. Significance level varies between the two dashed black lines, depending on length of the time series

the ensemble. The ensemble mean patterns of the warm and cold periods are statistically different with regards to the 5% level in a two sided t-test, except for in the Nordic Seas, south of $\sim$10°N and in the Gulf Stream region. Here, the number of models are used as degrees of freedom. The difference between the composites (Fig. 4a) has the same sign in the whole North Atlantic with largest values in the Subpolar Gyre region to the southeast of Greenland. A warm tongue is also seen extending from the Nordic Seas and into the Barents Sea. The intermodel spread (thin black lines) roughly follows the pattern of the anomaly. The largest model spread is found in the Subpolar Gyre region including the Irminger Sea, with almost the same amplitude as the differences between the warm and cold composites. In the tropical Atlantic there is only marginally higher temperatures in the warm compared to the cold periods. In order to see how sensitive this signal is to the chosen warm and cold periods, differences between all warm minus all cold 15 year periods in the models have also been calculated. This analysis gives approximately the same results (not shown).

The observed SST difference between a warm (1941–55) and a cold (1967–81) 15 year period (Fig. 4b) shows a warm anomaly mainly focused in the center of the Subpolar Gyre and around Iceland. The year to year standard deviation of the observed time series (thin black lines) shows that most of the temperature variance is found in the regions of largest temperature differences. The choice of warm period in the observations could potentially be problematic due to changes in the sampling technique (Thompson et al., 2008). Changing from warm biased engine room intake measurements (US ships) to a

Table 2: Warm and subsequent cold 15 year periods (center years) used to make AMO composites. The persistence (τ given in years) of the AMO time series is taken from the autocorrelation function of the annual time series

Model	Warm	Cold	τ
BCCR-BCM2.0	1879	1918	3
CCSM3	1962	1980	10
CGCM3.1(T47)	1864	1879	13
CGCM3.1(T63)	1923	1943	13
CNRM-CM3	1943	1958	4
CSIRO-Mk3.0	1904	1919	6
CSIRO-Mk3.5	1921	1937	1
ECHAM5/MPI-OM	1946	1966	4
ECHO-G	1945	1975	10
FGOALS-g1.0	-	-	25
GFDL-CM2.0	1960	1979	5
GFDL-CM2.1	1936	1950	5
GISS-AOM	1958	1968	2
GISS-EH	1878	1888	3
GISS-ER	1956	1977	3
INGV-SXG	1924	1932	2
INM-CM3.0	1957	1968	1
IPSL-CM4	1925	1940	4
MIROC3.2(HI)	1962	1970	1
MIROC3.2(MED)	1876	1893	4
MRI-CGCM2.3.2	1956	1969	5
PCM	1940	1962	3
UKMO-HadCM3	1878	1897	3
UKMO-HadGEM1	1940	1969	3
Observations	1948	1974	11

temporary majority of uninsulated bucket measurement (UK ships) may have made the cooling trend in the data larger than in reality. To test the robustness of the results, we have shifted the period forward or backward in time. The pattern stays the same but with a slightly reduced amplitude when omitting most of the affected time period (not shown). Comparison with the models show that the regions with largest temperature differences are south of Greenland for both cases, but over a slightly larger region in the observations. In the Norwegian Sea a modest warm anomaly is found in the models but not in the observations, while in the Iceland Sea the anomaly in the models is too low compared to the observations.

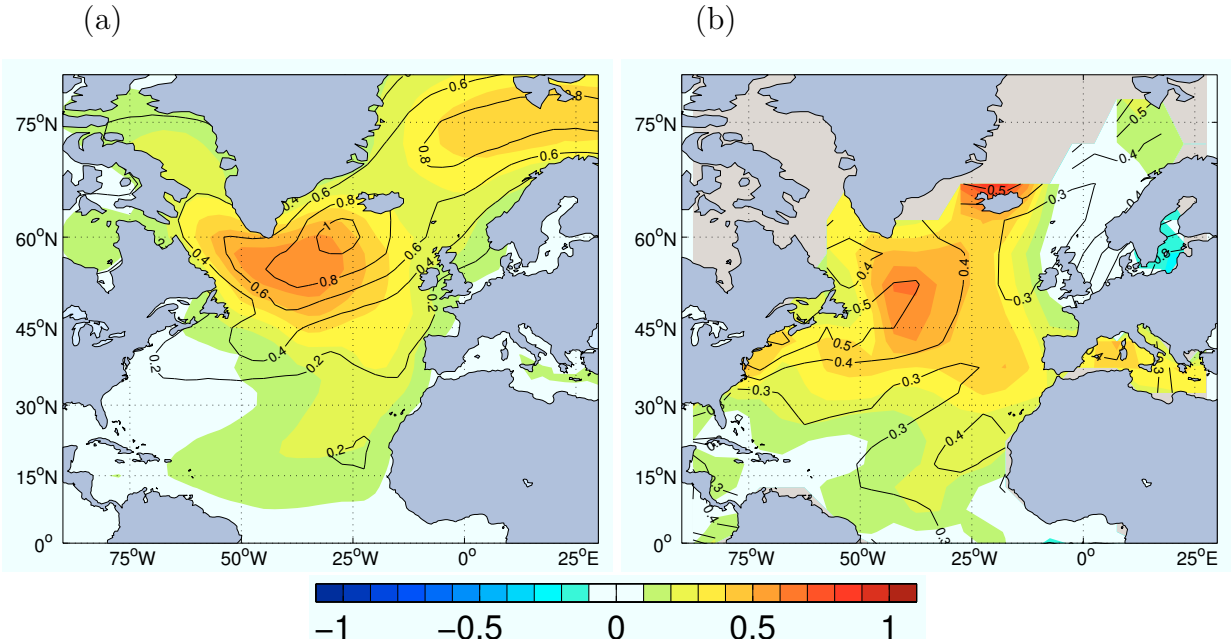

Figure 4: (a) Colour shading shows mean SST difference between the warmest 15 year period and the subsequent cold 15 year period in the models (see Table 2). Thin black lines show spread in the warm minus the cold SST differences represented by the standard deviation of the model responses. (b) Observed SST difference (°C) between a warm 15 year period (1941–55) and the subsequent cold 15 year period (1967–81). Thin black lines indicate the variability, given by the year to year standard deviation in of the observed time series. Gray areas have too few observations to make the analysis. Observations are from Kaplan et al. (1998)

3.2 AMOC

The models show highly varying structures in the mean state of their overturning (Fig. 5). The positions of the maximum overturning are typically found at 600–1500 m depth and between 20°N and 60°N. In comparison, the estimated depth of the maximum overturning at 25°N is from observations around 1000 m (Bryden et al., 2005). There are large differences in how the models reproduce the lower overturning cell. Several models show either an absent or a very weak lower overturning cell of Antarctic Bottom Water (AABW), while other models show AABW all the way north to 60°N. Hydrographic observations show that the AABW has almost disappeared north of 35°N (Johnson, 2008). One model, INM-CM3.0, show a deep gyre-driven upper circulation where the subtropical and subpolar gyres are nearly decoupled and where the AABW cell seems to be disconnected from the regions of AABW formation.

The models show an annual mean overturning circulation range from 1.3 to 67.7 Sv,

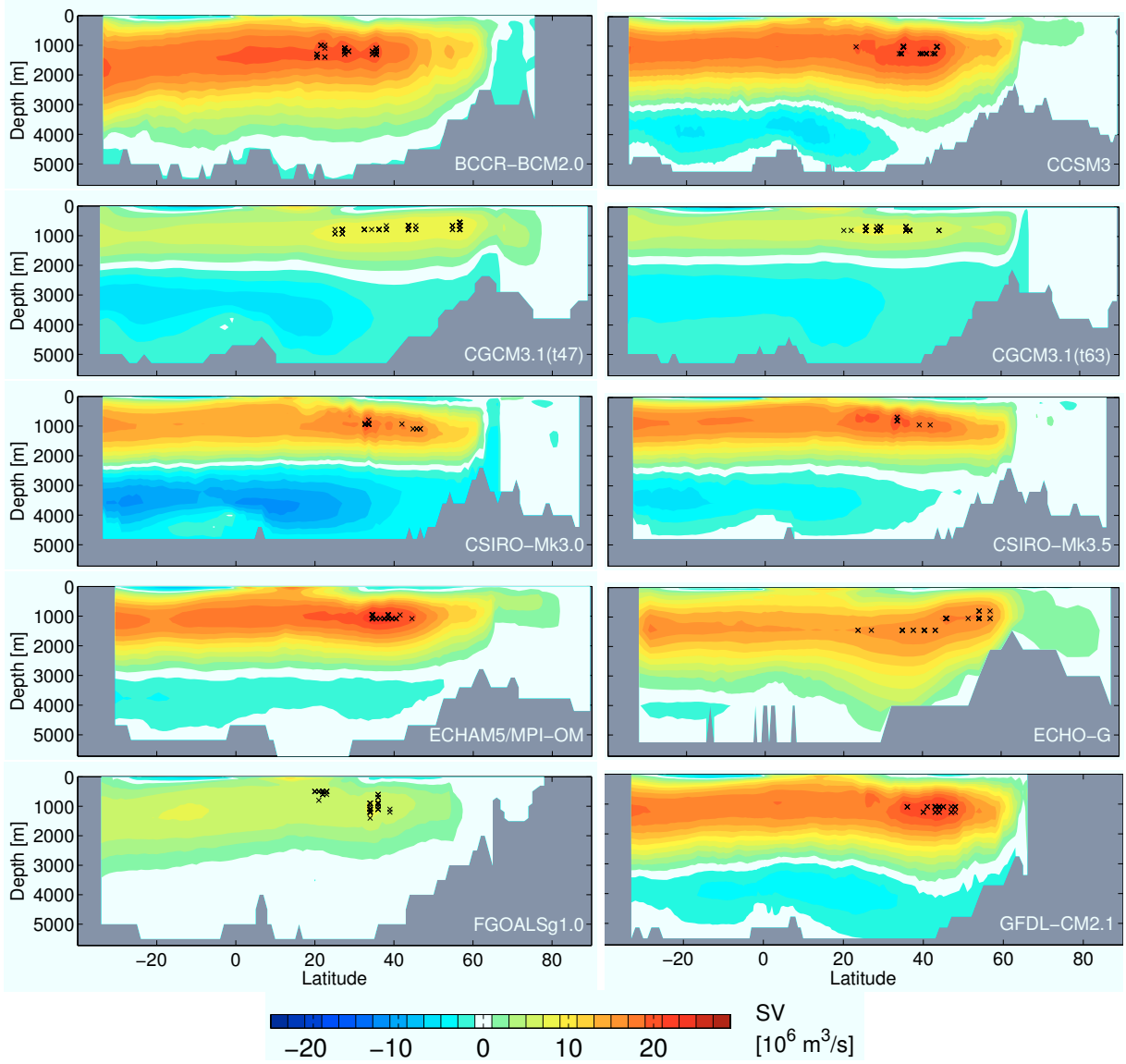

Figure 5: Mean state of the Atlantic meridional overturning streamfunction for the different models. Colour shading represents volume transport (Sv = 10^6 m^3 s^{-1}), where positive (negative) values indicate a clockwise (anticlockwise) circulation. × mark location of maximum overturning north of 20°N for individual years in the model

with a long term mean between 7.6 and 39.6 Sv. Based on hydrography, present-day estimates of the AMOC strength are 14–18 Sv at 24°N (Ganachaud and Wunsch, 2000; Lumpkin and Speer, 2003) and 13–19 Sv at 48°N (Ganachaud, 2003). Average values from estimates of NADW formation rate are 17.2 Sv (Smethie and Fine, 2001) and 18 Sv (Talley et al., 2003) with an error of ± 3–5 Sv. Observations from hydrographic sections at 26.5°N measured in the period 2004-2005, show year-long average overturning of 18.7

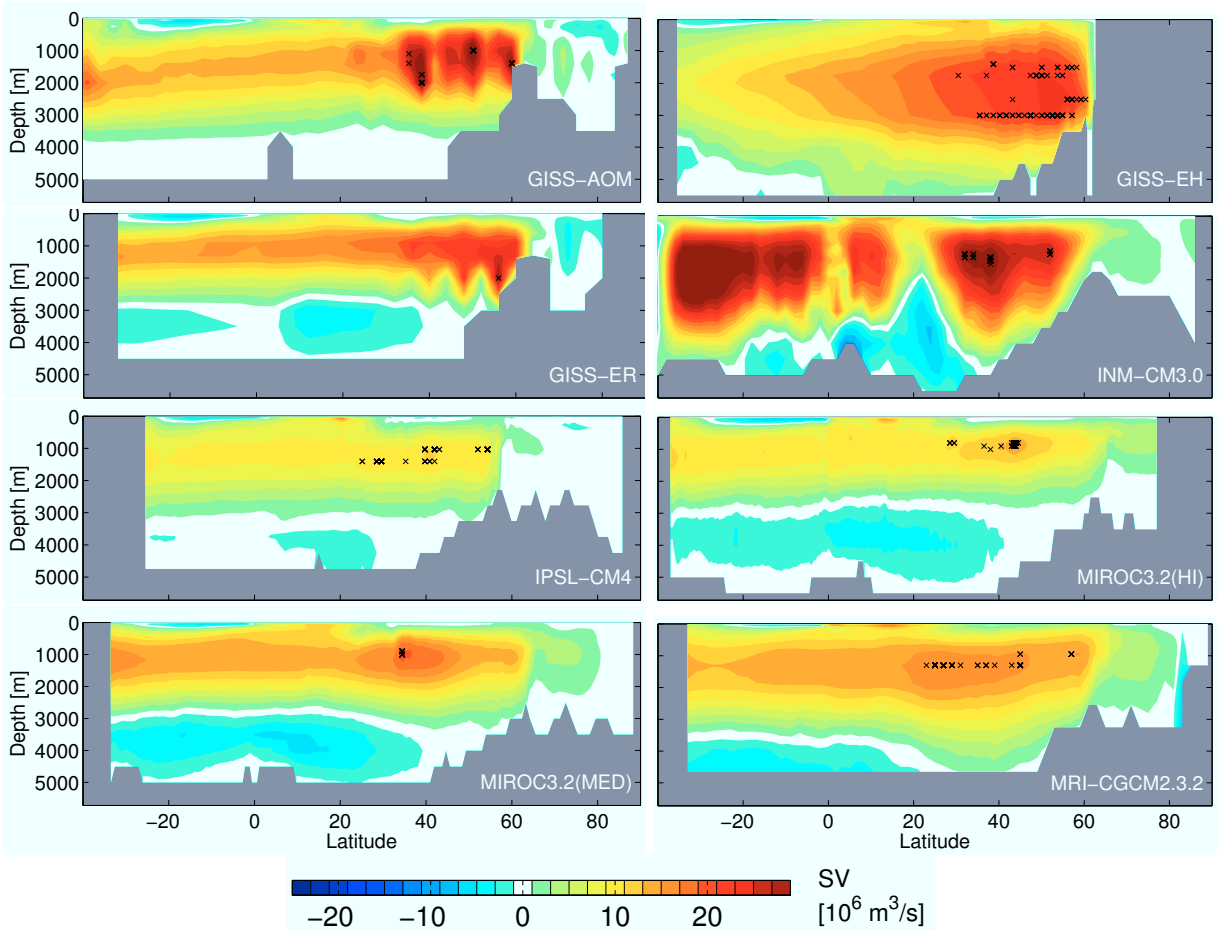

Figure 5: **Continued**

± 5.6 Sv (Cunningham et al., 2007). Taking all the observations together, this gives an observed range of 13–24.3 Sv. Many models are outside these estimates (Fig. 6a). GISS-AOM, INM-CM3.0, GISS-ER and GISS-EH show too strong, while FGOALS-g1.0, CGCM3.1(T47 and T63) and IPSL-CM4 show too weak overturning compared to the observations. The remaining 10 of the 18 models have a mean overturning within the observed range, and we will focus on this subset of models in the subsequent analysis.

Figure 6b shows the power spectra for the monthly AMOC index time series. The models have in general most energy on multidecadal time scales. The individual models all show increased power on time scales from around 20 years and upwards. Most models have maximum energy around the red noise level (not shown due to the varying autocorrelation at lag one defined in Sect. 2), but some show a decrease in power for periods from around 30 years and longer.

For the individual models the persistence in the AMOC variability varies from 1 to

a)

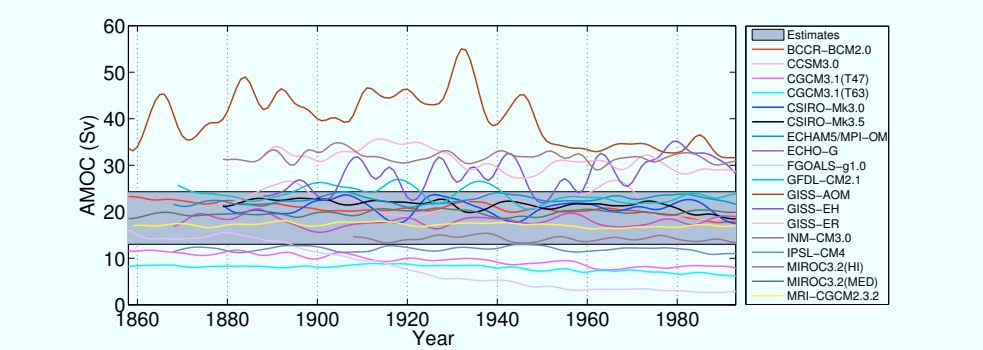

b)

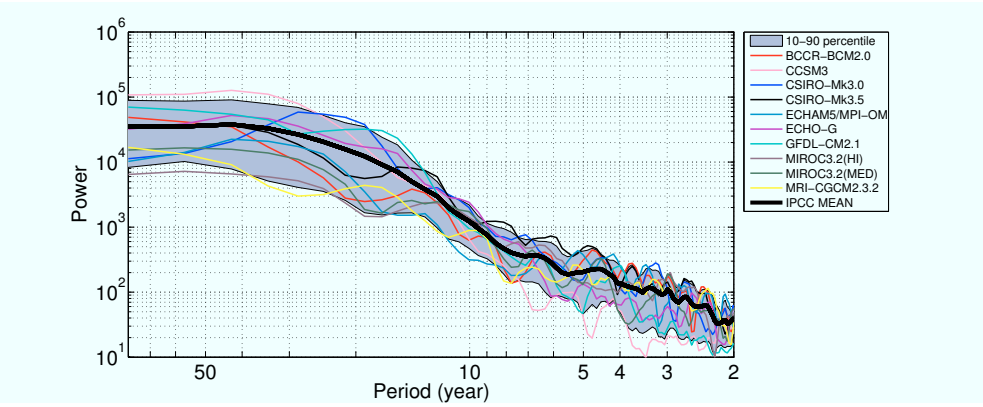

Figure 6: a) Atlantic Meridional Overturning Circulation (AMOC) strength (in Sv = 10^6 m^3 s^{-1}) for the individual model, defined as the maximum in the annual meridional streamfunction north of 20°N and below 500m depth. All curves are filtered by a 15 year running binomial filter. The gray band shows the present-day observational estimates of the AMOC in the range 13–24.3 Sv (references in text). b) Smoothed power spectrum of the detrended monthly time series of AMOC strength. The linear trends are removed and the time series are normalized for the different models prior to the analysis. The gray band shows the 10–90 percentile of the model spread, where the thick black line is the model mean and the coloured lines are the same as in (a). Only the 10 models having a mean overturning within the observed range are shown

10 years (Table 3), defined as the maximum time lag before the autocorrelation function first crosses the significance line at the 5% level (Fig. 7).

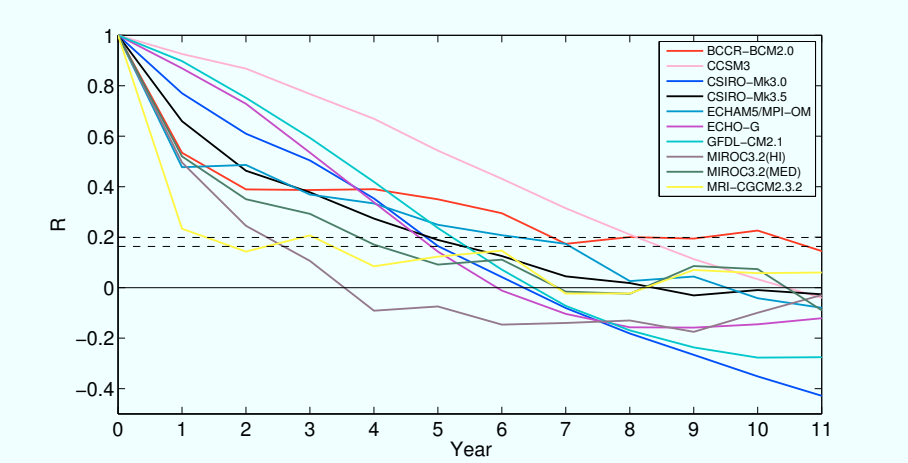

Figure 7: Autocorrelation function for the annual values of AMOC in the different models (coloured lines). Significance level varies between the two dashed black lines, depending on length of the time series. Only the 10 models having a mean overturning within the observed range are shown

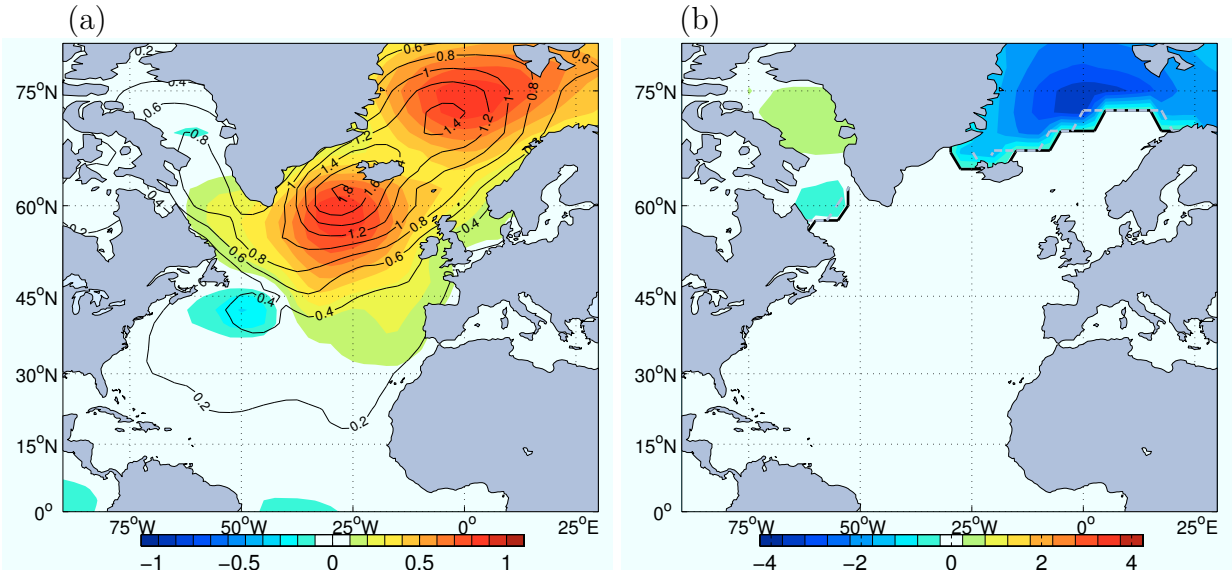

Figure 8: Composite of the ensemble mean difference between a 15 year period of strong AMOC and a 15 year period of weak AMOC (see Table 3) in (a) surface temperature (colour; °C), where thin lines show the ensemble standard deviation and (b) the sea ice concentration (%). The boundary of the annual mean, model-averaged, sea ice extent (defined at 15% ice consentration) is indicated by the black thick line for the weak AMOC period and thick gray dashed line for the strong AMOC period

3.3 Surface response to AMOC variability

Figure 8a shows the spatial pattern for the ensemble-mean surface temperature (TS) difference composite for a strong 15 year period minus a weak 15 year period of the

Table 3: Strong and subsequent weak 15 year periods (center years) used to make AMOC composites. The persistence (τ given in years) of the AMOC time series is taken from the autocorrelation function of the annual time series

Model	Strong	Weak	τ
BCCR-BCM2.0	1933	1949	10
CCSM3	1891	1920	8
CSIRO-Mk3.0	1905	1915	4
CSIRO-Mk3.5	1891	1938	5
ECHAM5/MPI-OM	1905	1923	7
ECHO-G	1881	1902	4
GFDL-CM2.1	1903	1927	5
MIROC3.2(HI)	1933	1948	2
MIROC3.2(MED)	1921	1945	4
MRI-CGCM2.3.2	1911	1924	1

AMOC index (see Table 3). The periods are selected where the 15 year average AMOC strength is at a maximum and the subsequent period of low AMOC strength subtracted. An exception has been made if the time series start from or end with the strong or weak AMOC, respectively, since it is unclear whether this is the actual maximum/minimum of the period. For strong AMOC the temperature in the northern North Atlantic and central Nordic Seas is reaching 0.9°C higher than for weak AMOC. Compared to the magnitude found for warm minus cold phases of AMO in the Subpolar Gyre region (Fig. 4a), the AMOC composite has a larger temperature difference, and the region of maximum temperature response is slightly displaced northeastward. In the Nordic Seas there is a substantial difference between the AMO and AMOC composites. Only for the tropical Atlantic, weak or even negative temperature differences are found for strong minus weak AMOC. The intermodel spread is very large over Iceland and Denmark Strait and into the Nordic Seas, and the signal to noise ration is low in these areas. The model spread seems to be partly due to the very variable sea ice extent in the different models, where some models have sea ice and others do not in these areas.

The corresponding fractional annual sea ice difference composite is shown in Fig. 8b. The sea ice generally extends further to the south and has higher concentration both in the Nordic Seas and Labrador Sea when AMOC is weak. For individual models the sea ice extent in the Greenland Sea is mainly unchanged or decreased for strong AMOC and

increased sea ice extent for weak AMOC compared to the mean (not shown). In the Barents Sea all models show increased sea ice extent for a weak AMOC, while the results are not conclusive for a strong AMOC. In the Labrador Sea the models show diverging results. The models with less sea ice are the same models that show higher temperatures for strong compared to weak AMOC.

3.4 Covariance between AMOC and AMO in models

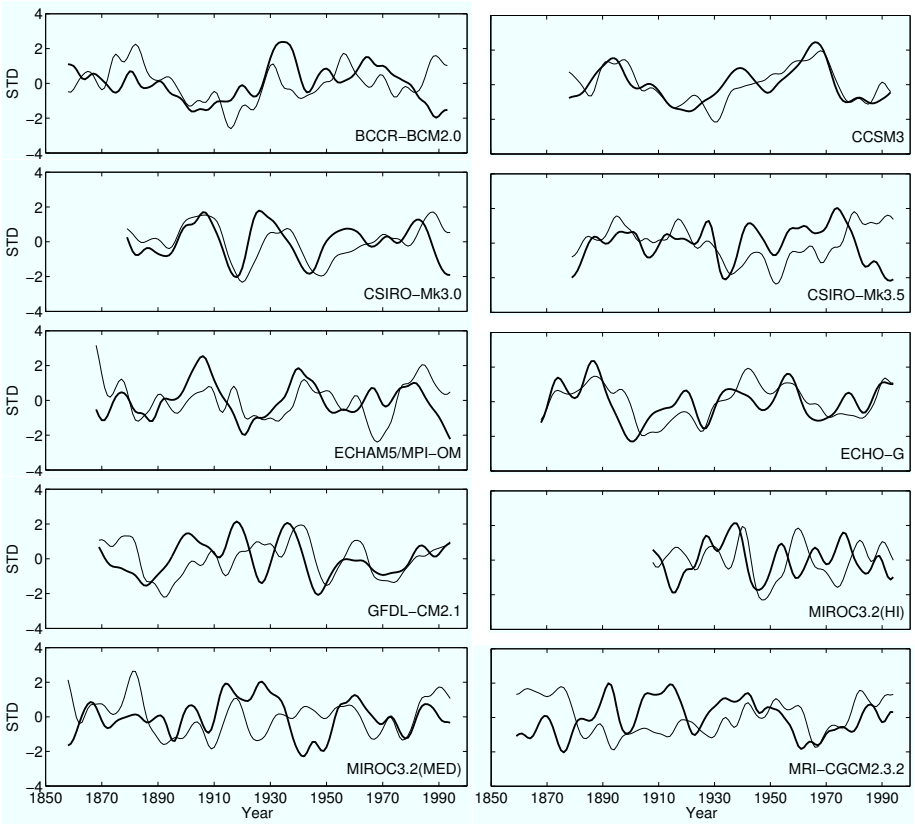

Figure 9: Normalized AMOC strength (thick line) and AMO (thin line) from the 15 year filtered time series for the different models

The low pass filtered and linearly detrended annual mean time series for the AMOC and AMO indices are shown in Fig. 9. The values and lags for the maximum correlations between the time series are shown in Table 4. Positive lag indicates that AMOC is leading the AMO, e.g., after a strong AMOC the North Atlantic SSTs will tend to be high some years later. All models show the maximum correlation at positive lag. The time lags of variy between 1 and 29 years, and the correlation varies between 0.04 (not significant) and 0.81. Thus the maximum variance that can be explained by the covariance is in the

Table 4: Maximum lagged correlation (R_{max}) between AMOC and AMO (AMO), and AMOC and rate-of-change of AMO (AMOroc) for the 15 year filtered time series. P-value indicate on which level the correlation is significant, where 0.975 indicates significance at 5% level using a two sided t-test with correction for degrees of freedom after the method of Quenouille (1952). Lag indicates time lags in years for maximum correlation. Lags are positive when AMOC is leading AMO. Max lag (N) is limited to 20% of the length of the time series in the individual models.

	AMO			AMOroc			N
Model	R_{max}	p-value	Lag	R_{max}	p-value	Lag	
BCCR-BCM2.0	0.45	0.990	21	0.29	0.965	-10	29
CCSM3	0.81	1.000	2	0.37	0.975	-4	25
CSIRO-Mk3.0	0.68	0.999	4	0.78	1.000	-2	25
CSIRO-Mk3.5	0.37	0.969	18	0.34	0.975	15	25
ECHAM5/MPI-OM	0.34	0.965	3	0.35	0.980	-3	25
ECHO-G	0.65	1.000	1	0.61	1.000	-3	27
GFDL-CM2.1	0.58	0.998	5	0.54	0.999	-1	19
MIROC3.2(HI)	0.43	0.971	4	0.43	0.980	1	29
MIROC3.2(MED)	0.39	0.984	28*	0.28	0.956	13	28
MRI-CGCM2.3.2	0.04	0.591	7	0.28	0.957	4	28

* The peak is located outside of the maximum lag included in the analysis. R_{max}=0.4 at lag 29

order of 65% or less.

Assuming that the North Atlantic becomes warmer when AMOC is stronger than normal, and colder when AMOC is weak, the rate-of-change of AMO should be a better proxy for AMOC than the actual magnitude of the AMO index itself (Fig. 10). With three exceptions (BCCR-BCM2.0, CSIRO-Mk3.5, MIROC3.2(MED)), the analysis does show that AMOC and rate-of-change of AMO is closer to be in phase (Table 4), indicating that there is a linkage between AMOC strength and warming or cooling of the Atlantic surface waters.

4 Discussion

A number of observational studies have shown multidecadal variability in the North Atlantic climate, with a typical time scale of around 50–70 years (e.g., Bjerknes, 1964;

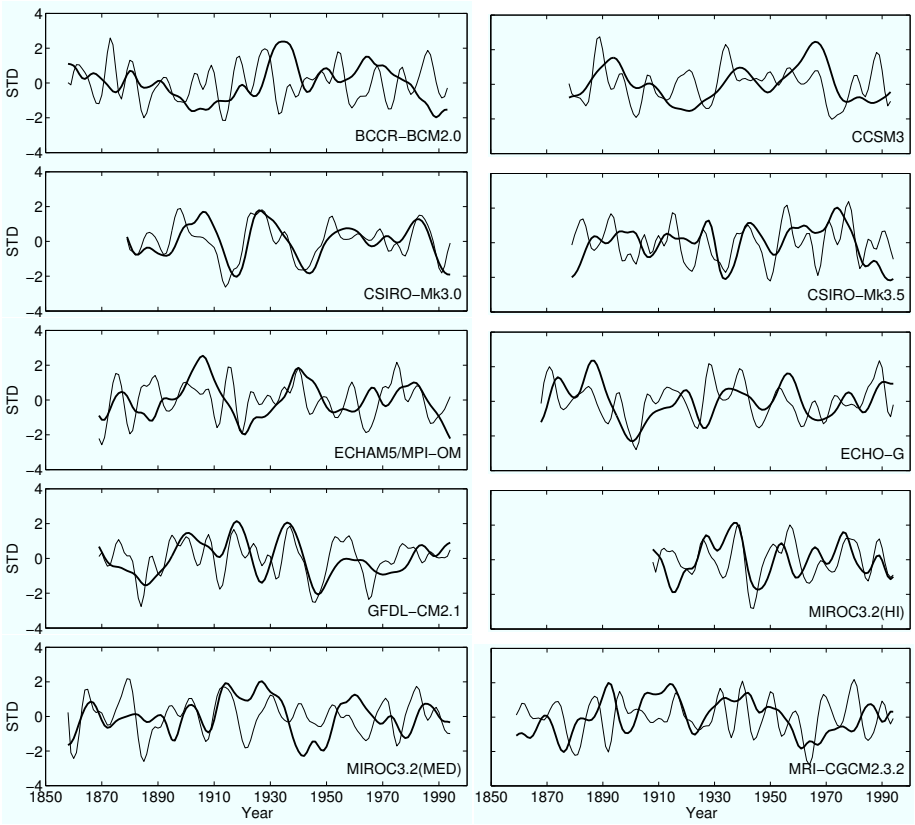

Figure 10: Normalized AMOC strength (thick line) and AMO rate-of-change (thin line) from the 15 year filtered time series for the different models

Kushnir, 1994; Schlesinger and Ramankutty, 1994; Delworth and Mann, 2000; Kravtsov and Spannagle, 2008), and a polar amplification of the climate variations (Furevik, 2001; Polyakov et al., 2004). 20th century extremes are the so-called early warming signal in the 1930s–50s (Delworth and Knutson, 2000) followed by the colder 1960s–80s, and also the very strong North Atlantic and Arctic warming after the 1990s may partly be due to a positive phasing of this mode (e.g., Knight et al., 2005; Zhang et al., 2007; Knight, 2009). Although many of the climate models are able to give reasonable amplitudes and to some extent the durations of the climate fluctuations in the North Atlantic region, they are not able to reproduce the timing of the observed warm and cold periods in our analysis. This indicates that the variability is intrinsic to the climate system and not primarily externally forced. This is in agreement with the findings of Kravtsov and Spannagle (2008), Knight (2009) and Ting et al. (2009), where a subset of the IPCC AR4 models was analysed. Other possibilities for the discrepancies, such as errors in the observed time series, inadequacy in the modelled response to the external forcing or forcing that is not included in the simulations have been studied thoroughly in Knight (2009), hence will not

be discussed here. Other model simulations, on the other hand, indicate that both solar variability and volcanoes play a role in setting the phase of the variability (Hansen et al., 2005; Otterå et al., 2010). The models are in general able to reproduce the pattern of the recent surface temperature extremes in most of the North Atlantic, but amplitudes seem to be too small in the Iceland Sea and too large in the Norwegian Sea compared to observations. Comparing warm minus cold AMO state, there is no sign of the observed polar amplification in the models. This indicates that the polar amplification is not in phase with the AMO.

For strong AMOC, the multi-model ensemble mean shows anomalously high temperatures in the mid and high latitudes (Fig. 8a), and also lower than normal sea ice extent in the Arctic (Fig. 8b). The most plausible mechanism supported by most models is that a stronger overturning transports more oceanic heat to high latitudes where more of the sea ice melts (Delworth et al., 1993; Medhaug et al., 2011). Contradicting this, some models surprisingly show more sea ice for stronger AMOC. An underlying mechanism in this seems to be that more northerly winds over the convection regions move the sea ice edge towards south by advection or local freezing, and more dense water is formed due to cooling and possibly also brine release. This will consequently lead to a strengthening of the overturning circulation (Hawkins and Sutton, 2007). The various mechanisms taking place in the individual models have not been the focus of this study and will not be discussed further.

Both the simulated and observed AMO indicate a potential for decadal predictability. While the observations show an inherent AMO persistence of around 11 years, the models have a memory of 1–25 years (Fig. 3). A similar range is found for the modelled AMOC variability, although long persistence of a signal in one parameter does not necessarily imply the same in the other of the two indices of North Atlantic variability. All models are found to have maximum correlation when AMO is lagging AMOC, with lags varying in the range of 1 to 29 years, indicating that AMO variability might be a response to the AMOC variability. When AMOC is found to lead AMO by several decades, an out-of-phase relationship between AMO and AMOC may be expected at shorter lags. This is only found for CSIRO-Mk3.5. For the others such relations are not found due to quasi-periodic time series. In 7 out of 10 models, AMOC is in phase with the rate-of-change of AMO, indicating that through changes in the northward advection of ocean heat, the sea surface temperature starts to respond. The overall results are the same whether we are using the AMO definition of Latif et al. (2004) (50–10°W, 40–60°N), Sutton and Hodson (2005) (75–7.5°W, 0–60°N) or the dipole pattern from Keenlyside et al. (2008)

(60–10W,40–60°N minus 50–0°W, 40–60°S), although the individual results will change slightly for the individual models.

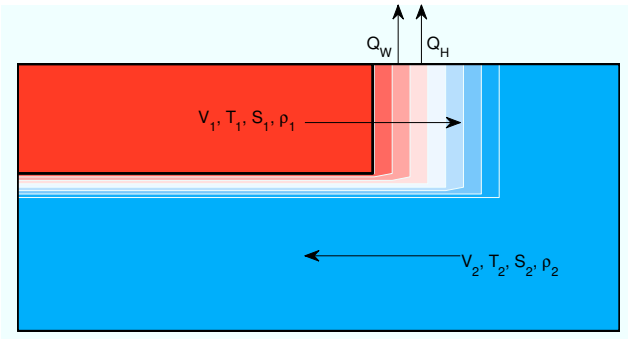

Figure 11: Simple model of the North Atlantic overturning circulation. The red region shows the reservoir simulating the warm tropical and subtropical water with the properties T_1, S_1 and ρ_1 being transported into the SPG region by the volume transport V_1. Here the water properties change due to surface cooling and the water sinks and returns as a deep return flow with a volume transport V_2 and the properties T_2, S_2 and ρ_2 in the blue box. Q_W and Q_H are the net atmospheric freshwater and heat fluxes, defined positive upwards

We should expect that if advection of heat plays a key role in the AMO variability there should be a simple relationship between the strength of the overturning and the frequency of the variability, as long as the volume of the active basins are the same. To illustrate this we introduce a simple conceptual model of the flow into and out of the Subpolar Gyre (SPG) region (Fig. 11). The northward flow (from red box) enters the SPG (blue box), sinks and reenters the World Oceans as deep and dense North Atlantic Deep Water. The equations for conservation of mass, heat and salinity for the SPG box become

$$\frac{d}{dt}M = V_1\rho_1 - V_2\rho_2 - Q_W\rho_W, \tag{1}$$

$$\frac{d}{dt}(Mc_pT_2) = V_1\rho_1 c_p T_1 - V_2\rho_2 c_p T_2 - Q_H, \tag{2}$$

$$\frac{d}{dt}MS_2 = V_1\rho_1 S_1 - V_2\rho_2 S_2, \tag{3}$$

where M is the mass of the water in the mixed layer of the SPG region (here the full water column), V_1 and V_2 are the volume transports and ρ_1, T_1, S_1 and ρ_2, T_2, S_2 are the densities, temperatures and salinities of water entering or leaving the SPG box, respectively. The net atmospheric freshwater and heat fluxes are given by Q_W [m^3 s^{-1}] and Q_H [J s^{-1}], defined positive upwards, c_p the specific heat capacity, and ρ_W the density of the

evaporating water.

To get the salinity balance in terms of fresh water content, we divide the salinity conservation equation (Eq. 3) on a reference salinity (S_0) and subtract from the mass conservation equation (Eq. 1). Using the Boussinesq approximation, neglecting evaporation minus precipitation in the mass conservation equation, and assuming conservation of volume gives the balance

$$V_1 = V_2, \tag{4}$$

$$\frac{dT_2}{dt} + \frac{V_2\rho_0}{M}T_2 = \frac{V_1\rho_0}{M}T_1 - \frac{Q_H}{Mc_p}, \tag{5}$$

$$\frac{dS_2}{dt} + \frac{V_2\rho_0}{M}S_2 = \frac{V_1\rho_0}{M}S_1 + \frac{S_0\rho_0 Q_W}{M}, \tag{6}$$

where ρ_0 is a reference density.

Equation 5 is a simple first order differential equation on the form $dT/dt + T/\tau = k$, where $\tau = M/V_1\rho_0$ and $k = T_1/\tau - Q_H/Mc_p$ (the discussion for salinity will be similar and is therefore omitted). τ is the flushing time scale of the system, i.e. the time it would have taken for the inflowing water to fill the volume of the SPG, k is a measure of the amount of heat entering the system. With constant coefficients τ and k the simple solution becomes

$$T(t) = (T_0 - k\tau)e^{-t/\tau} + k\tau \tag{7}$$

where T_0 is the temperature at $t = 0$. Using the size of the region where the temperature is most sensitive to changes in overturning strength (Fig. 8a), i.e. 45–65°N, 50–10°W gives $M = Area \times Depth \times \rho_0 \approx 5.6 \times 10^{18}$ kg, where the mixing depth is set to 1000 m due to the depth range of the upper North Atlantic Deep Water (Bryden et al., 2005) and ρ_0 is set to 1000 kg m^{-3}. Based on WOCE estimates (Ganachaud and Wunsch, 2000) the mean flow into the SPG region through 48°N has been estimated to $V_1 = 14$ Sv which from conservation of mass in the simple model equals the return flow at depth (V_2). This gives a flushing time of $\tau = 13$ years which may be interpreted as a time scale for persistence. Although not directly comparable, this is similar to the 11 years estimated from the autocorrelation of the observed AMO variability (Fig. 3). It is reasonable that the persistence is shorter than the flushing time since the latter is a measure for when all of the water is exchanged, while the former is a measure for when a temperature signal is lost through mixing with surrounding water. Also atmospheric variability will lower the persistence.

There are several studies indicating a relationship between the large scale north-south density gradient and the overturning circulation, where a larger depth integrated density

gradient is associated with a stronger overturning (Thorpe et al., 2001, and references therein). If more heat is transported into the sinking region, reduced density in the SPG will reduce the north-south density gradient and thus reduce the inflow strength. The result will be gradually colder water and a reversed phase. The time scale of this fluctuating behavior will depend on τ, the flushing time scale, with large flushing time scales τ indicating more long-periodic behavior.

For the salt transport, the analogous mechanism with a freshwater anomaly in the sinking region will lead to a reduced north-south density gradient and reduce the strength of the overturning. This will increase the residence time of the water in sub-tropical Atlantic, give a more net evaporation, and lead to a positive salinity anomaly being transported into the sinking region. This will in turn restore the north-south density gradient and speed up the overturning circulation. This mechanism is seen in a freshwater hosing experiment (Otterå et al., 2003). As the relative importance of the temperature and salinity anomalies in determining the density in the convective regions varies between the models, the mechanisms and thus the dominant time scales are expected to be highly model dependent (Delworth et al., 1993; Thorpe et al., 2001).

It should be noted finally that if there is a direct link between the strength of the AMOC and the AMO, irrespective of which mechanisms are at play, the periodicities of the two time series should be expected to be similar. Based on flushing time scales, the models with the strongest overturning circulation would be expected to be the same as those having the shortest memory if ocean advection is the dominant mechanism. For most models we find a clear link between the AMOC and AMO time scales, but no relation is found between the memory in the system and the strength of the overturning (Fig. 12). This clearly indicates that even if ocean advection (AMOC) plays an important role for the AMO variability, there are other factors such as non-predictable stochastic forcing from the atmosphere or externally forced variability that is masking the signal.

5 Summary and concluding remarks

Simulated variability in the North Atlantic has been investigated and compared with observations. Focus has been on the basin-scale averaged sea surface temperature variability known as the Atlantic Multidecadal Oscillation (AMO), and on the northward upper ocean transports associated with the Atlantic Meridional Overturning Circulation (AMOC). For the first time the full suit of IPCC AR4 atmosphere-ocean general circulation models have been used for this purpose. The models show most variability on

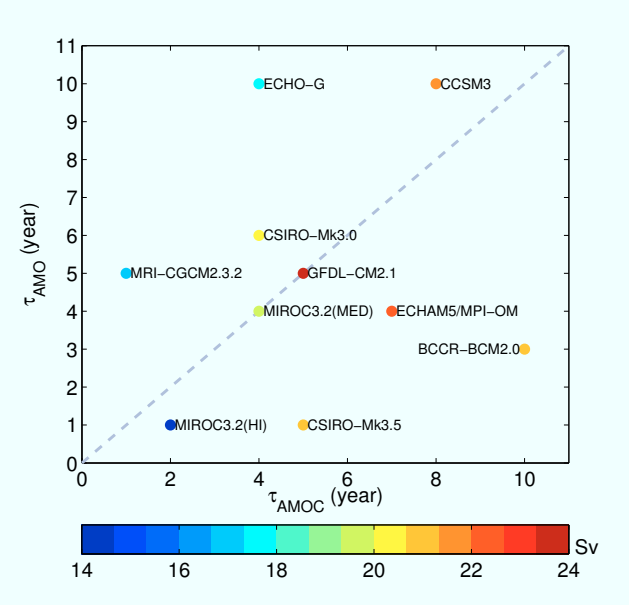

Figure 12: Flushing time scale (τ) of AMO vs AMOC defined as lag in years when the autocorrelation is significant. Colour shading represents the mean AMOC strength given in Sv (Sv = 10^6 m^3 s^{-1}). Models having identical AMO and AMOC decorrelation time will be along the gray dashed line

multidecadal time scales in the North Atlantic sector both with respect to the AMO and AMOC indices, but with a large intermodel spread in both amplitudes and frequencies. The AMOC is found to lead the AMO in all models, and for 7 out of the 10 models showing most realistic AMOC strength, AMOC is close to being in phase with the rate-of-change of AMO suggesting that increased northward heat transport warms the surface ocean.

The spatial structures and amplitude of the simulated temperature anomalies are similar to the observed, but the models fail to capture the timing of the observed extremes, indicating that they are primarily due to internally generated variability and not externally forced.

Most models show a realistic structure of the overturning circulation. This includes both the upper North Atlantic (AMOC) cell and the lower Antarctic overturning cell, and 10 out of 18 models show values within the observationally-based estimate of the range of 13–24.3 Sv for the North Atlantic overturning.

Associated with a stronger AMOC the models shows a positive temperature anomaly and reduced sea ice extent in both the Nordic Seas and in the Labrador Sea compared to a weak AMOC.

From a simple conceptual model connecting flushing time scales of a temperature/salinity

anomaly to the overturning circulation through the north-south density gradient, there is a potential mechanism for decadal predictability of the SSTs if the AMOC state is known. However, from the model results, it is not possible to identify a common mechanism responsible for the variability associated with the AMO, or evidence that observations of the surface properties of the ocean (e.g., AMO) automatically can be used as a proxy for the state of the overturning, as suggested by Collins et al. (2006), Smith et al. (2007) and Keenlyside et al. (2008). Hence the road toward future operational decadal predictions of North Atlantic or global climate should involve a full 3D assimilation of the state of the ocean, including both sea level height anomaly from satellites and hydrography, the latter being available through the Argo project (Roemmich and Owens, 2000; Gould, 2005). The study by Dunstone and Smith (2010) suggests that this might significantly improve the skills of the decadal predictions compared to only using the sea surface properties.

Acknowledgments

The project has been supported by the Research Council of Norway through the NorClim project, and is also contributing to the BIAC and DecCen projects. The authors would like to thank Asgeir Sorteberg for help throughout the work, and Nils Gunnar Kvamstø and David Stephenson for useful comments to an earlier draft. This publication is no. XXXX from the Bjerknes Centre for Climate Research.

References

Baringer, M. O. and Molinari, R.: Atlantic Ocean baroclinic heat flux at 24 to 26° N, Geophys. Res. Lett., 26, 353–356, 1999.

Bartlett, M. S.: An introduction to stochastic processes. Cambridge University Press, 1966.

Bentsen, M., Drange, H., Furevik, T., and Zhou, T.: Simulated variability of the Atlantic meridional overturning circulation, Clim. Dynam., 22, 701–720, doi:10.1007/s00382-004-0397-x, 2004.

Bjerknes, J.: Atlantic air-sea interaction, edited by: Landsberg, H. E. and Van Mieghem, J., Adv. Geophys., Academic press, 1–82, 1964.

Bryden, H. L., Longworth, H. R., and Cunningham, S. A.: Slowing of the Atlantic meridional overturning circulation at 25°N. Nature, 438, 655–657, doi:10.1038/nature04385, 2005.

Collins, M., Botzet, M., Carril, A. F., Drange, H., Jouzeau, A., Latif, M., Masina, S., Otterå, O. H., Pohlmann, H., Sorteberg, A., Sutton, R., and Terray, L.: Interannual to decadal climate predictability in the North Atlantic: a multimodel-ensemble study, J. Climate, 19(7), 1195–1203, 2006.

Cunningham, S. A., Kanzow, T., Rayner, D., Baringer, M. O., Johns, W. E., Marotzke, J., Longworth, H. R., Grand, E. M., Hirschi, J. J. M., Beal, L. M., Meinen, C. S., and Bryden, H. L.: Temporal variability for the Atlantic Meridional Overturning Circulation at 26.5°N, Science, 317, 935–937, doi:10.1126/science.1141304, 2007.

Delworth, T. L. and Knutson, T. R.: imulation of early 20th century global warming, Science, 287(5461), 2246–2250, 2000.

Delworth, T. L., Manabe, S. and Stouffer, R. J.: Interdecadal variation in the thermohaline circulation in a coupled ocean-atmosphere model, J. Climate, 6, 1993–2011, 1993.

Delworth, T. L. and Mann, M. E.: Observed and simulated multidecadal variability in the Northern hemisphere, Clim. Dynam., 16, 661–676, 2000.

Delworth, T. L., Clark, P. U., Holland, M., Johns, W. E., Kuhlbrodt, T., Lynch-Stieglitz, J., Morrill, C., Seager, R., Weaver, A. J., and Zhang, R.: The potential for abrupt change in the Atlantic Meridional Overturning Circulation. Abrupt Climate Change, A report by the U.S., Climate Change Science Program and the Subcommittee on Global Change Research, U.S. Geological Survey, Reston, VA, chap. 4, 117–162, 2008.

Deshayes, J. and Frankignoul, C.: Simulated variability of the circulation of the North Atlantic from 1953 to 2003. J. Climate, 21, 4919–4933, doi:11.1175/2008JCLI1882.1, 2008.

Dickson, R., Lazier, J., Meincke, J., Rhines, P., and Swift, J.: Long-term coordinated changes in the convective activity of the North Atlantic, Prog. Oceanogr., 38, 241–295, 1996.

Dunstone, N. J. and Smith, D. M.: Impact of atmosphere and sub-surface ocean data on decadal climate prediction, Geophys. Res. Lett., 37, L02709, doi:10.1029/2009GL041609, 2010.

Eden, C. and Willebrand, J.: Mechanisms of interannual to decadal variability of the North Atlantic circulation, J. Climate, 14, 2266–2280, 2001.

Frankcombe, L. M., Dijkstra, H. A., and von der Heydt, A.: Noise-induced multidecadal variability in the North Atlantic: Excitation of normal modes, J. Phys. Oceanogr., 39, 220–233, doi:10.1175/2008JPO3951.1, 2009.

Frankignoul, C., Müller, P., and Zorita, E.: A simple model of the decadal response of the ocean to stochastic wind forcing, J. Phys. Oceanogr., 27, 1533–1546, 1997.

Fuglister, F. C.: Atlantic Ocean Atlas of temperature and salinity profiles and data from the international geophysical year of 1957–1958, Woods Hole Oceanogr Inst Atlas Series, Vol. 1, Woods Hole Oceanographic Institution, Woods Hole, Mass, 1960.

Furevik, T.: Annual and interannual variability of Atlantic Water temperatures in the Norwegian and Barents Seas: 1980-1996. Deep-Sea Res. Pt. I, 48(2), 383–404, 2001.

Furevik, T., Bentsen, M., Drange, H., Kindem, I. K. T., Kvamstø, N. G., and Sorteberg, A.: Description and evaluation of the Bergen climate model: ARPEGE coupled with MICOM, Clim. Dynam., 21, 27–51, doi:10.1007/s00383-003-0317-5, 2003.

Ganachaud, A.: Large-scale mass transports, water mass formation, and diffusivities estimated from World Ocean Circulation Experiment (WOCE) hydrographic data, J. Geophys. Res., 108(C7), 3213, doi:10.1029/2002JC001565, 2003.

Ganachaud, A. and Wunsch, C.: Improved estimates of global ocean circulation, heat transport and mixing from hydrographic data, Nature, 408, 453–457, 2000.

Gijbels, I., Pope, A., and Wand, M. P.: Understanding exponential smoothing via kernel regression, J. R. Stat. Soc. B, 61(1), 39–50, 1999.

Gould, J.: From shallow floats to Argo-The development of neutrally buoyant floats, Deep-Sea Res. Pt. II, 52, 529–543, 2005.

Hansen, J., Nazarenko, L., Ruedy, R., Sato, M., Willis, J., Del Genio, A., Koch, D., Lacis, A., Lo, K., Menon, S., Navakov, T., Perlwiz, J., Russel, G., Schmidt, G. A., and Tausenev, N.: Earth's energy imbalance: confirmation and implications, Science, 308, 1431, doi:10.1126/science.1110252, 2005.

Hasselmann, K.: Stochastic climate models, Part I, theory, Tellus, 28, 473–483, 1976.

Hawkins, E. and Sutton, R.: Variability of the Atlantic thermohaline circulation described by three-dimensional empirical orthogonal functions. Clim. Dynam., 29, 745–762, doi:10.1007/s00382-007-0263-8, 2007.

Häkkinen, S.: Variability of the simulated meridional heat transport in the North Atlantic for the period 1951–1993, J. Geophys. Res., 104(C5), 10991–11007, 1999.

Hurrell, J. W., Kushnir, Y., Ottersen, G., and Visbeck, M.: An overview of the North Atlantic Oscillation, The North Atlantic Oscillation: Climatic significance and environmental impact, edited by: Hurrell, J. W., Kushnir, Y., Ottersen, G., and Visbeck, M., American Geophysical Union, Geoph. Monog. Series, 134, 1–35, 2003.

IPCC, 2007: Climate Change 2007: The physical science basis. Contribution of Working Group I to the Fourth Assessment Report of the Intergovernmental Panel on Climate Change, Cambridge University Press, Cambridge, United Kingdom and New York, NY, USA.

Johnson, G. C.: Quantifying Antarctic Bottom Water and North Atlantic Deep Water volumes, J. Geophys. Res., 113, C05027, doi:10.1029/2007JC004477, 2008.

Jungclaus, J. H., Haak, H., Latif, M., and Mikolajewicz, U.: Arctic-North Atlantic interactions and multidecadal variability of the meridional overturning circulation, J. Climate, 18(19), 4013–4031, 2005.

Kaplan, A., Cane, M., Kushnir, Y., Clement, A., Blumenthal, M., and Rajagopalan, B.: Analyses of global sea surface temperature 1856–1991, J. Geophys. Res., 103, 18567–18589, 1998.

Keenlyside, N. S., Latif, M., Jungclaus, J., Kornblueh, L., and Roeckner, E.: Advancing decadal-scale climate prediction in the North Atlantic sector. Nature, 453, 84–88, doi:10.1038/nature06921, 2008.

Knight, J. R.: The Atlantic Multidecadal Oscillation inferred from the forced climate response in coupled general circulation models, J. Climate, 22, 1610–1625, doi:10.1175/2008JCLI2628.1, 2009.

Knight, J. R., Allan, R. J., Folland, C. K., Vellinga, M., and Mann, M. E.: A signature of persistent natural thermohaline circulation cycles in observed climate, Geophys. Res. Lett., 32, L20708, doi:10.1029/2006GL026242, 2005.

Kravtsov, S. and Spannagle, C.: Multidecadal climate variability in observed and modeled surface temperatures, J. Climate, 21, 1104–1121, doi:10.1175/2007JCLI1874.1, 2008.

Kushnir, Y.: Interdecadal variations in North Atlantic sea surface temperature and associated atmospheric conditions, J. Climate, 7(1), 141–157, 1994.

Latif, M., Roeckner, E., Botzet, M., Esch, M., Haak, H., Hagemann, S., Jungclaus, J. H., Legutke, S., Marsland, S., and Mickolajevicz, U.: Reconstructing, monitoring, and predicting multidecadal-scale changes in the North Atlantic thermohaline circulation with sea surface temperature, J. Climate, 17, 1605–1613, 2004.

Lumpkin, R. and Speer, K.: Large-scale vertical and horizontal circulation in the North Atlantic Ocean, J. Phys. Oceanogr., 33, 1902–1920, 2003.

Marshall, J., Kushnir, Y., Battisti, D., Chang, P., Czaja, A., Dickson, R., Hurrell, J., McCartney, M., Saravanan, R., and Visbeck, M.: North Atlantic climate variability: Phenomena, impacts and mechanisms, Int. J. Climatol., 21, 1863–1898, 2001.

Medhaug, I., Langehaug, H. R., Eldevik, T., and Furevik, T.: Mechanisms for multidecadal variability in a simulated Atlantic Meridional Overturning Circulation, in prep., 2011.

Msadek, R. and Frankignoul, C.: Atlantic multidecadal oceanic variability and its influence on the atmosphere in a climate model, Clim. Dynam., 33, 45–62, doi:10.1007/s00382-008-0452-0, 2009.

Otterå, O. H., Bentsen, M., Drange, H., and Suo, L.: External forcing as a metronome for Atlantic multidecadal variability, Nat. Geosci., 3, 688–694, doi:10.1038/ngeo955, 2010.

Otterå, O. H., Drange,H., Bentsen, M., Kvamstø, N. G., and Jiang, D.: The sensitivity of the present-day Atlantic meridional overturning circulation to freshwater forcing, Geophys. Res. Lett., 30(17), 1898, doi:10.1029/2003GL017578, 2003.

Parrilla, G., Lavín, A., Bryden, H., and Millard, R.: Rising temperatures in the subtropical North Atlantic Ocean over the past 35 years, Nature, 369, 48–51, 1994.

Pohlmann, H., Jungclaus, J., Köhl, A., Stammer, D., and Marotzke, J.: Initializing decadal climate prediction with the GECCO oceanic synthesis: Effects on the North Atlantic, J. Climate, 22, 3926–3938, 2009.

Polyakov, I. V. and Johnson, M. A.: Arctic decadal and interdecadal variability, Geophys. Res. Lett., 27(24), 4097–4100, 2000.

Polyakov, I. V., Alekseev, G. V., Timikhov, L. A., Bhatt, U. S., Colony, R. L., Simmons, H. L., Walsh, D., Walsh, J. E., and Zakharov, V. F.: Variability of the Intermediate Atlantic Water of the Arctic Ocean over the last 100 years, J. Climate, 17(23), 4485–4497, 2004.

Quenouille, M. H.: Associated Measurements, Butterworths, London, 241 pp., 1952.

Roemmich, D. and Owens, W. B.: The Argo project: Global ocean observations for understanding and prediction of climate variability, Oceanogr., 13, 45–50, 2000.

Roemmich, D. and Wunsch, C.: Two transatlantic sections: meridional circulation and heat flux in the subtropical North Atlantic Ocean, Deep-Sea Res., 32, 619–664, 1985.

Schlesinger, M. E. and Ramankutty, N.: An oscillation in the global climate system of period 65-70 years, Nature, 367, 723–726, 1994.

Schott, F. A., McCreary Jr, J. P., and Johnson, G. C.: Shallow overturning circulation of the tropical-subtropical oceans, Earth Climate: The Ocean-Atmosphere Interaction, edited by: Wang, C., Xie, S., and Carton, J. A., American Geophysical Union, Geoph. Monog. Series, 147, 261–304, 2004.

Smethie, W. M. and Fine, R. A.: Rates of North Atlantic deep water formation calculated from chlorofluorocarbon inventories, Deep-Sea Res. Pt. I, 48, 189–215, 2001.

Smith, D. M., Cusack, S., Colman, A. W., Folland, C. K., Harris, G. R., and Murphy, J. M.: Improved surface temperature prediction for the coming decade from a global climate model, Science, 317, 796–799, doi:10.1126/science.1139540, 2007.

Sutton, R. T. and Hodson, D. L. R.:Atlantic Ocean forcing of North American and European summer climate, Science, 309(5731), 115–118, doi:10.1126/science.110949, 2005.

Talley, L. D., Reid, J. L., and Robbins, P. E.: Data-based meridional overturning streamfunctions for the global ocean, J. Climate, 16, 3213–3226, 2003.

Thompson, D. J.: Spectrum estimation and harmonic analysis, P IEEE, 70(9), 1055–1096, 1982.

Thompson, D. W. J., Kennedy, J. J., Wallace, J. M., and Jones, P. D.: A large discontinuity in the mid-twentieth century in observed global-mean surface temperature, Nature, 453, 646–649, doi:10.1038/nature06982, 2008.

Thorpe, R. B., Gregory, J. M., Johns, T. C., Wood, R. A., and Mitchell, J. F. B.: Mechanisms determining the Atlantic thermohaline circulation response to greenhouse gas forcing in a non-flux-adjusted coupled climate model, J. Climate, 14, 3102–3116, 2001.

Ting, M., Kushnir, Y., Seager, R., and Li, C.: Forced and internal twentieth-century SST trends in the North Atlantic, J. Climate, 22, 1469–1481, doi:10.1175/2008JCLI2561.1, 2009.

Trenberth, K. E. and Caron, J. M.: Estimates of meridional atmosphere and ocean heat transports, J. Climate, 14, 3433–3443, 2001.

Vellinga, M. and Wu, P.: Low-latitude freshwater influence on centennial variability of the Atlantic thermohaline circulation, J. Climate, 17, 4498–4511, doi:10.1175/3219.1, 2004.

Woodgate, R. A., Aagaard, K., and Weingartner, T. J.: Monthly temperature, salinity, and transport variability of the Bering Strait through flow, Geophys. Res. Lett., 32, L04601, doi:10.1029/2004GL021880, 2005.

Wunsch, C.: What is the thermohaline circulation? Science, 298, 1180–1181, 2002.

Zhang, R., Delworth, T. L., and Held, I. M.: Can the Atlantic Ocean drive the observed multidecadal variability in Northern Hemisphere mean temperature?, Geophys. Res. Lett., 34, L02709, doi:10.1029/2006GL028683, 2007.

Paper II

Mechanisms for multidecadal variability in a simulated Atlantic Meridional Overturning Circulation

Medhaug, I., H. R. Langehaug, R. Eldevik and T. Furevik

Climate Dynamics, (submitted)

Mechanisms for multidecadal variability in a simulated Atlantic Meridional Overturning Circulation

I. Medhaug[1,2], H. R. Langehaug[3,2], T. Eldevik[1,2] and T. Furevik[1,2]

[1]*Geophysical Institute, University of Bergen, Bergen, Norway*

[2]*Bjerknes Centre for Climate Research, Bergen, Norway*

[3]*Nansen Environmental and Remote Sensing Center, Bergen, Norway*

Abstract

Variability in the Atlantic Meridional Overturning Circulation (AMOC) has been analysed using a 600-year pre-industrial control simulation with the Bergen Climate Model. The typical AMOC variability has amplitudes of 1 Sverdrup (1 Sv = 10^6 m^3 s^{-1}) and time scales of 40-70 years. The model is reproducing the observed dense water formation regions and has very realistic ocean transports and water mass distributions. The dense water produced in the Labrador Sea (1/3) and in the Nordic Seas, including the water entrained into the dense overflows across the Greenland-Scotland Ridge (GSR; 2/3), are the sources of North Atlantic Deep Water (NADW) forming the lower limb of the AMOC's northern overturning. The variability in the Labrador Sea and the Nordic Seas convection is driven by air-sea fluxes in the convective region that can be related to opposite phases of the North Atlantic Oscillation. The Labrador Sea convection is directly linked to the variability in AMOC. Linkages between convection and water mass transformation in the Nordic Seas are more indirect. The Scandinavian Pattern, the third mode of atmospheric variability in the North Atlantic, is a driver of the ocean's poleward heat transport (PHT), the overall constraint on northern water mass transformation. Increased PHT is both associated with an increased water mass exchange across the GSR, and a stronger AMOC.

Keywords: *Multidecadal variability, Atlantic Meridional Overturning Circulation, Deep water formation, Water mass transformations, Convection*

1 Introduction

The Atlantic Meridional Overturning circulation (AMOC) is wind- and density driven with northward flowing surface water in the North Atlantic Current, buoyancy loss and sinking in

the north, and southward flowing North Atlantic Deep Water (NADW) at depth. The circulation is closed as NADW is gradually brought to the surface by low latitude diapycnal mixing as well as wind-driven upwelling in the Southern Ocean (Kuhlbrodt et al. 2007). Further below there is a weaker and reversed overturning cell associated with the northward spreading of the denser Antarctic Bottom Water, which gradually mixes with the southward flowing NADW above (e.g., Ganachaud and Wunsch 2000; Johnson 2008).

While surface water is flowing from low to high latitudes, it gradually looses buoyancy due to cooling. The effect is partly compensated by freshening from river runoff, precipitation and ice melt. The lowering of the centre of mass represents a loss in potential energy. Without energy input, the deep ocean would turn into a stagnant pool of dense water within the order of thousand years (Munk and Wunsch 1998). The energy needed to drive the AMOC comes from winds and tides gradually mixing deep and dense water masses with lighter waters above and thus increasing the potential energy (Munk and Wunsch 1998; Wunsch 2002; Gade and Gustafsson 2004; Kuhlbrodt et al. 2007). Using wind and satellite altimetry products (e.g., Egbert and Ray 2000) the spatial variations in the energy input can be estimated, but little is known about how this energy input is varying on decadal and longer time scales, and to what extent and on which time scales such variations can influence the overturning.

Although schematically simple and appealing, the exact mechanisms governing the mean AMOC structure, and its spatial and temporal variability, are far from understood. Recent findings indicate that synoptic surface winds and small scale ocean eddies have much more important roles in the circulation than what has been the traditional view, and that the various components of the overturning circulation are varying both spatially and temporally contrary to what has been the perception from studies of ocean tracers or coarse resolution climate models (see Lozier 2010, and references therein).

Due to its linkages with the northward heat transport and the climate of the North Atlantic region (e.g., Vellinga and Wood 2002; McManus et al. 2004; Rhines et al. 2008), AMOC variability is a key constraint on observed or projected climate change. The majority of the state-of-the-art climate models show a weakening in the AMOC throughout the 21st century when they are forced with increasing atmospheric greenhouse gas concentrations (e.g., Gregory et al. 2005; Meehl et al. 2007; Medhaug and Furevik 2011). In the models warming

and freshening in the north reduce the buoyancy loss and weaken the rate of water mass transformation. While the models agree on the sign of the changes they do not agree on the relative importance of the change in heat and freshwater fluxes for the weakening of the AMOC. There are at present no observations indicating whether such a decrease in overturning rate is already taking place (e.g., Cunningham et al. 2007; Cunningham and Marsh 2010). On the contrary, high-resolution modelling (Biastoch et al. 2008) and combined satellite altimetry and in situ observations (Willis 2010) hint to a weak upward trend in overturning circulation during the last decades.

The North Atlantic Ocean (see overview map in Fig. 1) has two main source regions for deep water: The Labrador Sea/Irminger Sea and the Nordic Seas (Clarke and Gascard 1983; Dickson and Brown 1994; Hansen and Østerhus 2000; Pickart et al. 2003). Surface cooling, and in some shelf regions brine release due to ice freezing, make the relatively saline North Atlantic water sufficiently dense to form the NADW.

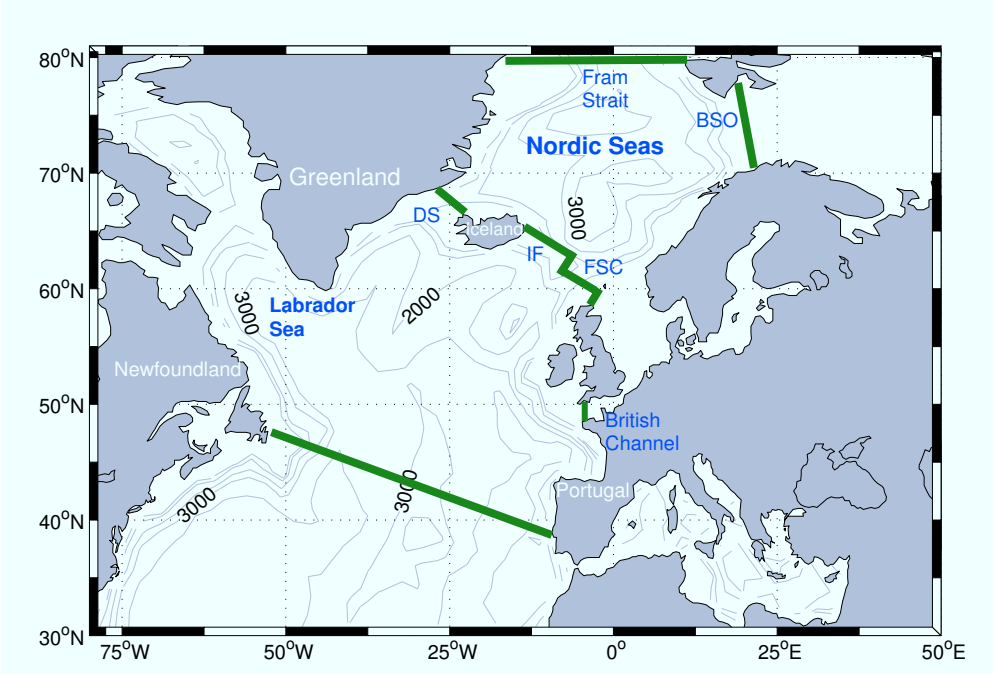

Fig. 1 Bathymetry of the North Atlantic – Nordic Seas region. Green sections show the Fram strait, Barents Sea opening (BSO), the Greenland-Scotland Ridge (GSR) and the British Channel enclosing the Nordic Seas, and the Newfoundland section in the North Atlantic. Openings on the GSR are indicated by the Denmark Strait (DS), Iceland-Faroe Ridge (IF) and Faroe-Shetland Channel (FSC)

From direct current measurements and water mass properties, Dickson and Brown (1994) estimated that around one-third of the total NADW originates from water spilling over the

Greenland-Scotland Ridge, one third is due to entrainment of ambient water when this water is cascading downwards south of the sill, and the final third originates in the Labrador Sea.

Due to its potential great importance for North Atlantic climate, improved knowledge of the mechanisms for the variability in AMOC will improve the understanding and simulation of present and upcoming climate variability. This includes detection and attribution of anthropogenic climate change, the origins for the discrepancies between models and observations, and the construction of observational schemes for initialising future decadal climate prediction systems.

The aim of this work is to identify mechanisms for the low frequency changes in the Atlantic Meridional Overturning Circulation (AMOC) in the Bergen Climate Model (Otterå et al. 2009; 2010) and compare with what is known from observations. Previously suggested candidates for AMOC variability are oceanic response to aggregated atmospheric white noise forcing at high northern latitudes where dense water is produced (e.g., Dickson et al. 1996; Häkkinen 1999; Delworth and Greatbatch 2000; Eden and Willebrand 2001; Deshayes and Frankignoul 2008), a pure oceanic mode associated with advection of density anomalies (e.g., Delworth et al. 1993; Jungclaus et al. 2005), or a coupled atmosphere-ocean mode which in some models includes sea ice variability (e.g., Holland et al. 2001; Bentsen et al. 2004; Biastoch et al. 2008).

The layout of this paper is as follows. Section 2 contains a brief model description with the formulation of mixed layer and convection dynamics, and the statistical methods used in the analysis. The dense water formation regions are identified and the driving mechanisms for the decadal to multidecadal changes of the AMOC are presented in section 3 and discussed in section 4. Summary and concluding remarks are given in section 5.

2 The coupled Bergen Climate Model

2.1 Model description

The model run being used for this study is a 600-year long simulation of the pre-industrial control climate with the Bergen Climate Model (BCM), a fully coupled atmosphere-ocean-sea ice general circulation model. A general description of the model can be found in

Furevik et al. (2003), with more recent updates given in Otterå et al. (2009). Only a brief overview of the model system will be given here.

The model consists of the ocean model MICOM (Miami Isopycnic Coordinate Ocean Model; Bleck et al. 1992) coupled with the atmospheric model ARPEGE/IFS (Action de Recherche Petite Echelle Grande Echelle/Integrate Forecast System; Déqué et al. 1994). A dynamic-thermodynamic sea ice model (GELATO; Salas-Mélia 2002) is included. The model uses no flux correction, and is therefore free to evolve its own climatology. The only constraint is the seasonal cycle of the incoming solar radiation at the top of the atmosphere.

ARPEGE is configured with a spectral truncation of wave number (T_L63) on a linear grid. The physical resolution is approximately 2.8˚ along the Equator and a total of 31 vertical levels are used, ranging from the surface to 0.01 hPa. The horizontal distribution of continental and marine aerosols, aerosols from desert dust and black carbon, are held constant at their respective default values. Concentrations of tropospheric sulphate aerosols and the atmospheric CO_2 concentration and held fixed at pre-industrial level, and a solar constant of 1370 W m^{-2} is used.

The horizontal ocean grid in MICOM is almost regular with a grid spacing approximately 2.4˚ latitude × 2.4˚ longitude. To better resolve tropically confined dynamics, latitudinal grid spacing is gradually decreasing to 0.8˚ near the Equator. The ocean model consists of 34 isopycnic layers below the non-isopycnic mixed layer. MICOM uses potential density with reference pressure at 2000 decibar (db) as vertical coordinate (σ_2 -coordinate), whereas the previous version of BCM (Furevik et al. 2003) used 0 db (σ_0 -coordinate) as reference pressure. The potential density relative to 2000 db ranges from σ_2 = 30.119 kg m^{-3} to σ_2 = 37.800 kg m^{-3} in the isopycnic layers. The pressure gradient force is computed as the gradient of the geopotential on pressure surfaces and the geopotential is found by an accurate integration of the hydrostatic equation using in-situ density.

2.2 Mixed layer dynamics

On top of the isopycnic layers there is a non-isopycnic mixed layer (ML), providing the connection between the atmosphere and the interior of the ocean. The density of the ML varies horizontally and temporally. Three mixing processes determine the mass exchange

across the interface between the ML and the interior isopycnic layers. These are (1) diapycnal mixing, i.e. mixing across the density interfaces, (2) the mass exchange caused by changes in mixed layer depth (MLD) determined by a Kraus-Turner type parameterization, and (3) convective adjustment (Kraus and Turner 1967; Gaspar 1988; Bleck et al. 1992). The diapycnal mixing is generally small compared to the other two processes, but in areas with dense plumes of water flowing down steep bottom slopes, the diapycnal mixing is considerable. To incorporate the shear instability and gravity current mixing a Richardson number dependent diffusivity is included (see Orre et al. 2009).

In contrast to earlier versions of this model, the MLD is no longer the best indicator of where deep convection occurs. If the ML becomes denser than the water in the layer below such that the water column tends to become unstable, convective mixing is parameterized to happen instantaneously to restore the stability. In previous versions of the model this was done by entrainment of the entire isopycnic layer below (Fig. 2a). This led to unphysical stepwise increase in MLD, and to spurious flows associated with the tilting of the density surfaces. In the updated version (Fig. 2b), stability is achieved without the large expansion of the ML. Here a slightly modified version of Bleck et al. (1992) has been used: A portion of water with density (ρ_k) matching that of the receiving intermediate layer, k, is instead detrained from the ML, and replaced by an equal amount of water with a density just below that of the layer below. The expansion of layer k is accounted for by an equal reduction in the thickness of layer k-1, giving a doming structure of the isopycnals.

2.3 Methods

The rate of which the water is detrained from the mixed layer due to instability is used as an indicator of where the convection in the model occurs, and where dense water is convected to increase the thickness of the intermediate layers.

In the model, more than 80% of the annual convection in the Nordic Seas (including Greenland, Iceland and Norwegian seas) and more than 90% of the annual convection in the Labrador Sea happens during the winter (herein November-April). This period has therefore been used when calculating convection rates and for calculating the atmospheric forcing variables used in the convection analysis in section 3. For all other purposes annual values are used.

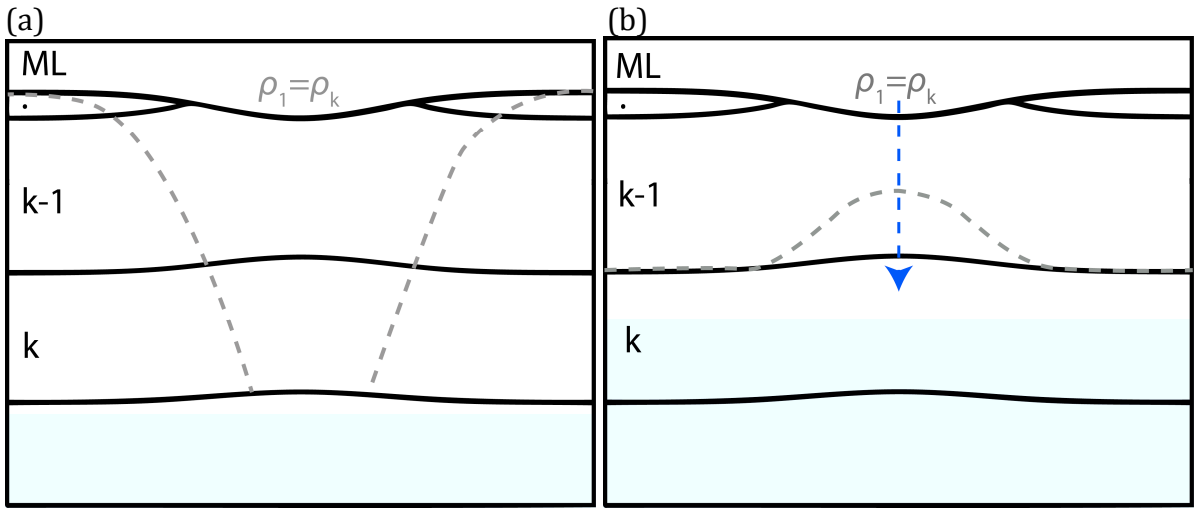

Fig. 2 A schematic of the isopycnals of the (a) old and (b) the new convection scheme in the model. Black lines show the isopycnals for an initial stable state and the gray dashed lines show the isopycnals after the adjustment for instability in the mixed layer. Letters in the left side of the figures indicate layer number, where ML indicates the mixed layer. The density of the mixed layer (ρ_1) equals the density (ρ_k) of the intermediate layer (k) before the convection

Since the focus of this paper is on multidecadal variability, the inter-annual variability has been removed using a centred third order Butterworth low-pass filter with a cut-off period of 5 years. In the correlation/regression analyses the time series have further been high-pass filtered using the same filter but removing time scales longer than 100 years. The latter is to avoid spurious statistical relationships due to model drift or other low-frequency changes.

For significance testing a student *t*-test is used together with Chelton's (1983) method for estimating the effective number of degrees of freedom by taking into account the cross- and auto-covariance of the two time series. Significance at 5% level is used if not stated otherwise.

3 Results

3.1 Atlantic Meridional Overturning Circulation (AMOC)

The Atlantic meridional overturning is quantified by the stream function

$$\psi_V(y,z,t) = \int_{-z}^{0}\int_{0}^{L} v(x,y,z,t)\,dx\,dz\,,$$

where the meridional velocity $v(x,y,z,t)$ is integrated from west ($x = 0$) to east ($x = L$) across the basin, and from depth z up to the surface.

Average AMOC in the BCM (Fig. 3a) shows an upper cell of northward flow from the surface and down to 800–1300 m (where maximum ψ_V is found). In the areas north of around 60˚N the water sinks, and returns southward at depth as North Atlantic Deep Water (NADW). Below is a weak signal of the counter-circulating Antarctic Bottom Water (1.2 Sv; 1 Sv = 10^6 m^3 s^{-1}), and a negative stream function at the bottom reflects the net inflow through the Bering Strait (1.5 Sv).

In this study the AMOC index is defined as the maximum overturning stream function value in the latitudinal band north of 20˚N for each model year (Fig. 3b). The position of the maximum is found to vary between 22˚N and 45˚N. For decadal and longer time scales a latitudinal varying index has been shown to capture the basin-wide spinup/spin-down of the NADW cell, while the physical interpretation of this index on interannual time scales is shown to be potentially problematic (Vellinga and Wu 2004). The mean modelled AMOC index is 18.8 Sv. From observational estimates the mean overturning circulation is in the range of 13-24.3 Sv, estimated from hydrographic observations at 24˚N (Ganachaud and Wunsch 2000; Lumpkin and Speer 2003), 26.5˚N (Cunningham et al. 2007), and 48˚N (Ganachaud 2003), and from estimated NADW formation rates (Smethie and Fine 2001; Talley et al. 2003). Hence, the modelled overturning strength is well within the observational range.

There is little observational basis for constraining the longer term variability of the AMOC or the amplitude of fluctuations in general. The power spectrum of the modelled AMOC index shows power resembling a theoretical red noise spectrum. An exception is the increased power at periods around 40-70 years, where the energy at 45 years periodicity is found to be significant above the red noise (Fig. 3c). The time scales are similar to what is found in many other models (e.g., ~50 yrs in Delworth et al. 1993; 70-80 yrs in Jungclaus et al. 2005; ~60 yrs in Zhu and Jungclaus 2008), and also similar to the 65-70 year variability in the North Atlantic surface climate suggested by observations (e.g., Schlesinger and Ramankutty 1994).

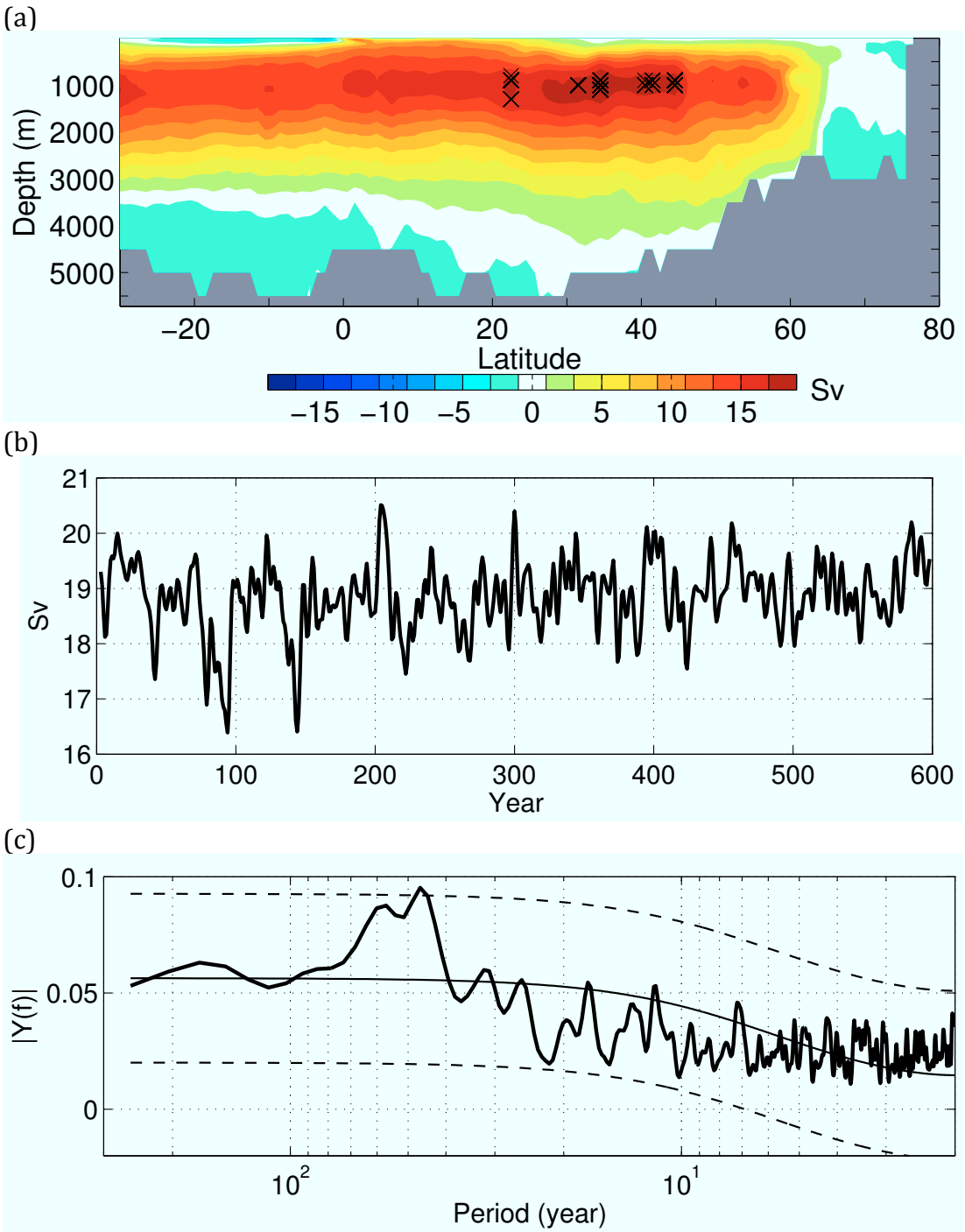

Fig. 3 (a) Mean state of the Atlantic meridional overturning stream function. Colour shading represents the zonally integrated volume transport, where positive (negative) values indicate a clockwise (anticlockwise) circulation. × marks the maximum overturning north of 20˚N for the individual model years, giving the AMOC index. (b) The low-pass filtered annual mean AMOC index. Units given in Sv (Sv = 10^6 m^3 s^{-1}). (c) Smoothed power spectrum of the linearly detrended annual data (thick line) together with the theoretical red noise spectrum (thin solid line) computed by fitting a first order autoregressive process with a 95% confidence interval (dashed lines) around the red noise

3.2 Gyre circulation

The horizontal stream function $\psi_H(x,y,t)$ is here defined as the vertically and zonally integrated meridional flow integrated from bottom (-*H*) to surface and from the western coastline towards east

$$\psi_H(x,y,t) = \int_0^x \int_{-H}^0 v(x,y,z,t)dzdx .$$

Sign conversion is defined by cyclonic (anticyclonic) flow having negative (positive) values in the stream function.

The average modelled North Atlantic barotropic stream function (Fig. 4**,** contours) shows an anticyclonic circulation to the south (STG; subtropical gyre), with a maximum volume transport exceeding 30 Sv, and a cyclonic subpolar gyre (SPG) transporting slightly less water. This approximately is as seen in observations, where the STG is found to be 20-40 Sv (Schott et al. 1988; Bryden et al. 2005) and the SPG 25-40 Sv (Clarke 1984; Bacon 1997), where the STG is generally considered slightly stronger than SPG (Curry and McCarthey 2001).

A mixture of water from these two gyres is flowing across the Greenland-Scotland Ridge (GSR) into the Nordic Seas, where it circulates in a cyclonic direction, gradually releasing heat to the atmosphere, increases in density and sinks. In the model, the western part of the Nordic Seas cyclonic circulation cell is shifted east compared to observations (Fig. 4). This is most likely due to too zonal westerlies bringing fewer storms into the Nordic Seas (Otterå et al. 2009), resulting in a large Nordic Seas sea ice cover in the model.

3.3 Convective Mixing Regions

The strongest convection occurs over the continental slope southwest of Svalbard, with an average sinking rate of water from the mixed layer to the layers below reaching 30 m day-1 in the winter months (Fig. 4, colour shading). Some open ocean convection also occurs in the eastern part of the Greenland Sea. Although the sinking rate may seem very large, horizontal advection rates responsible for exporting the denser water from the formation region are at least two orders of magnitudes larger. In the northwestern part of the Labrador

Sea, the modelled sinking from plume convection reaches 12 m day^{-1} while smaller values are seen in the Irminger Sea. The bulk part of this convection occurs on the continental shelves or on the shelf slopes.

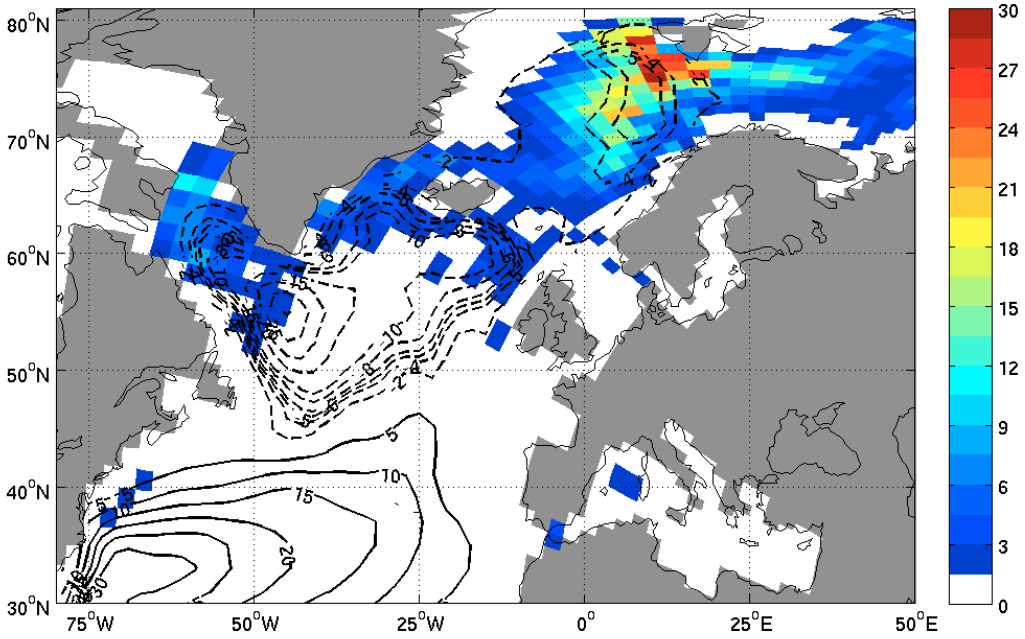

Fig. 4 North Atlantic long-term average winter (Nov-Apr) convection (colours; in m per day) together with long term average annual barotropic stream function (contours; in Sv). Solid lines indicate anti-cyclonic and dashed lines cyclonic circulation

In order to show the dominant pattern of variability in the convection, we have calculated the first Empirical Orthogonal Function (EOF1) of convection in the Nordic Seas (Fig. 5a), explaining 22% of the variance in the data. This shows a dipole pattern, indicating that when there is more convection in the northern Norwegian Sea (positive region on the map), there is less convection in the Fram Strait (negative region). One standard deviation increase in the PC (Fig. 5b) corresponds to more than 5 m day-1 change in sinking rates in the two regions. The convection follows the sea ice edge, where there is increased convection in the Norwegian Sea for more sea ice, and in the Greenland Sea for reduced sea ice extent.

The corresponding leading EOF of the convection in the Labrador Sea (Fig. 5c) shows that most of the variability in the convection occurs in the northwestern part. In contrast to the Nordic Seas the mode shows a monopole structure. This pattern explains 19% of the

variance in the convection time series. The corresponding PC1 for this pattern can be seen in Fig. 5d. The sea ice extent in the Labrador Sea does not reach the main convective region.

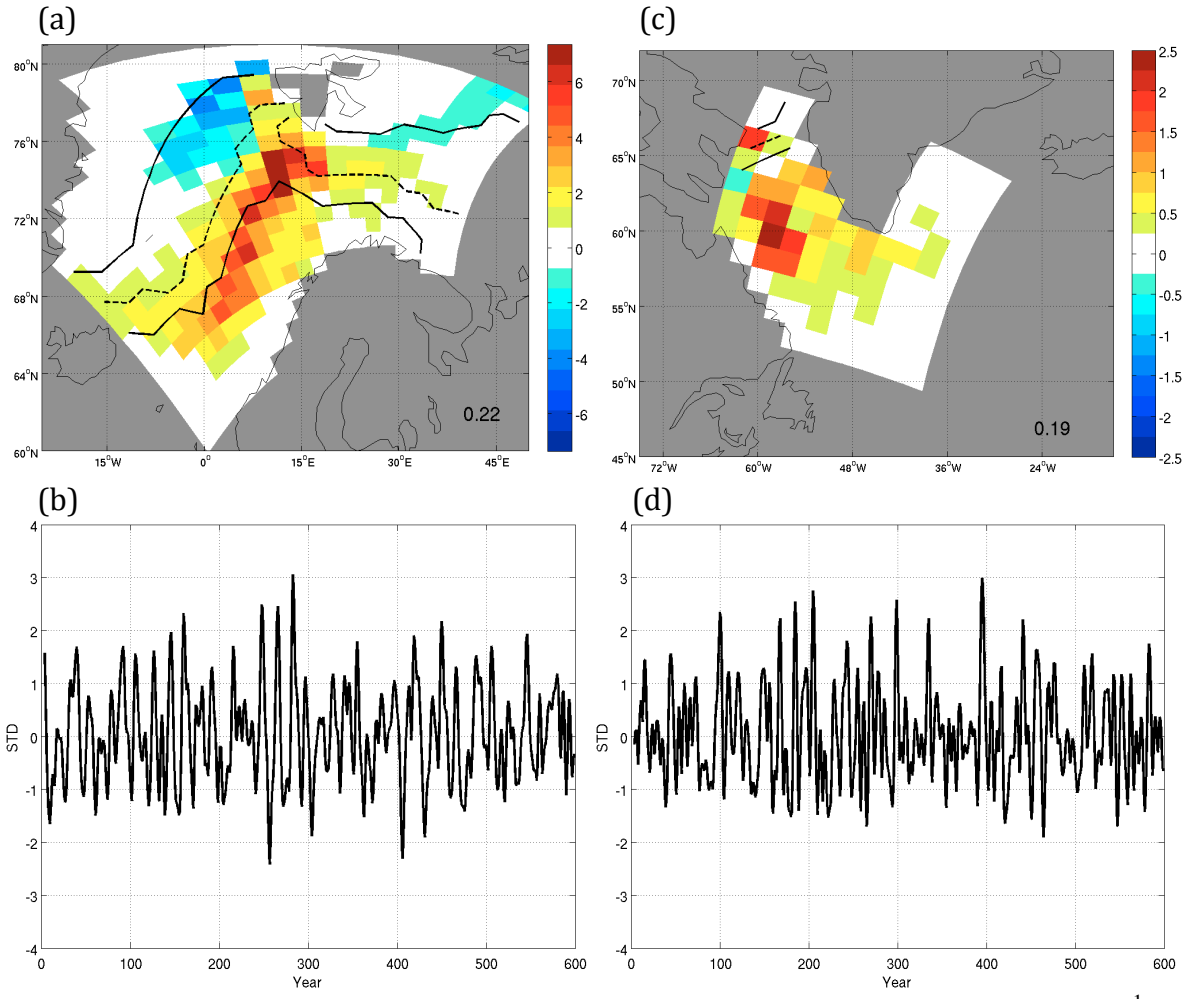

Fig. 5 The first EOF of the (a) Nordic Seas and (c) Labrador Sea convection (in m day $^{-1}$ std^{-1}) calculated for the white and colored area. The convection time series for the individual grid points have been high-pass filtered. Black thick lines show the minimum, mean (dashed) and maximum March sea ice extent. The explained variance is given in the bottom right corner. Low-pass filtered first principal components (in std) for the (b) Nordic Seas and (d) Labrador Sea

3.4 Atmospheric forcing: Heat, freshwater and momentum fluxes in the Nordic Seas and Labrador Sea

There is a net winter heat flux from the ocean to the atmosphere in the entire North Atlantic and Nordic Seas (Fig. 6a), with maximum heat loss found off Cape Hatteras, where the Gulf Stream leaves the eastern coast of North America, in the northeastern Nordic Seas, and in the Labrador Sea. The winter freshwater fluxes (Fig. 6b) are generally large along the sea ice

edge position (the border between positive and negative values), with a positive freshwater flux out of the ocean where sea ice is formed (the ocean becomes more saline), and a negative freshwater flux where sea ice melts. River runoff from land, and in the subtropics the net evaporation (E – P > 0), also contributes to the freshwater flux. Note that the land contribution is relatively small since the data is from northern hemisphere winter with little river runoff. The momentum flux (Fig. 6c) is on average strongest in the North Atlantic Current region, around the Denmark Strait and in the Labrador Sea. A region of increased momentum flux is also seen south east of Svalbard.

In order to investigate where the buoyancy forcing (heat and freshwater fluxes) is increasing the local surface density and contributing to convection, and where the forcing has a stabilizing effect on the water column, regressions between the convection and each of the forcing terms have been calculated (Fig. 6d-f). Regions of positive (negative) regressions show where the forcing has a positive (negative) contribution to the convection. More heat loss, less freshwater input or more wind (i.e., more vertical mixing) generally acts to increase surface density and thus the convection. The results show that the strongest response in convection (i.e., detrainment rate) is due to changes in heat and freshwater fluxes. The freshwater flux is acting to reduce convection in the Fram Strait region, since it is negatively correlated with convection. The reason is that convection driven by more heat loss from more open water implies less sea ice freezing. Here the negative contribution from sea ice melt is counteracting the positive contribution from decreased precipitation. In contrast, in the Norwegian Sea a positive freshwater flux anomaly (more sea ice and evaporation and/or less precipitation) is contributing to convection. In the Labrador Sea all three contributions have a positive effect on the convection.

The convection in the Nordic Seas is significantly correlated with the NAO index (R = -0.46), where NAO leads by 1 year. Averaged over the Nordic Seas, the negative NAO phase indicates less freshwater (due to less precipitation), more heat loss from the ocean to the atmosphere and slightly stronger wind. The correlations between the freshwater flux, and heat flux with the NAO index are -0.52 and -0.32, respectively. The wind stress does not have a significant correlation with the NAO. The correlation between the convection and the heat and freshwater fluxes averaged over the Nordic Seas are close to 0.5 at zero time lag. The analysis further indicates stronger momentum fluxes and preconditioning of the mixed layer, where the momentum flux is found to lead convection by one year (Fig. 7a).

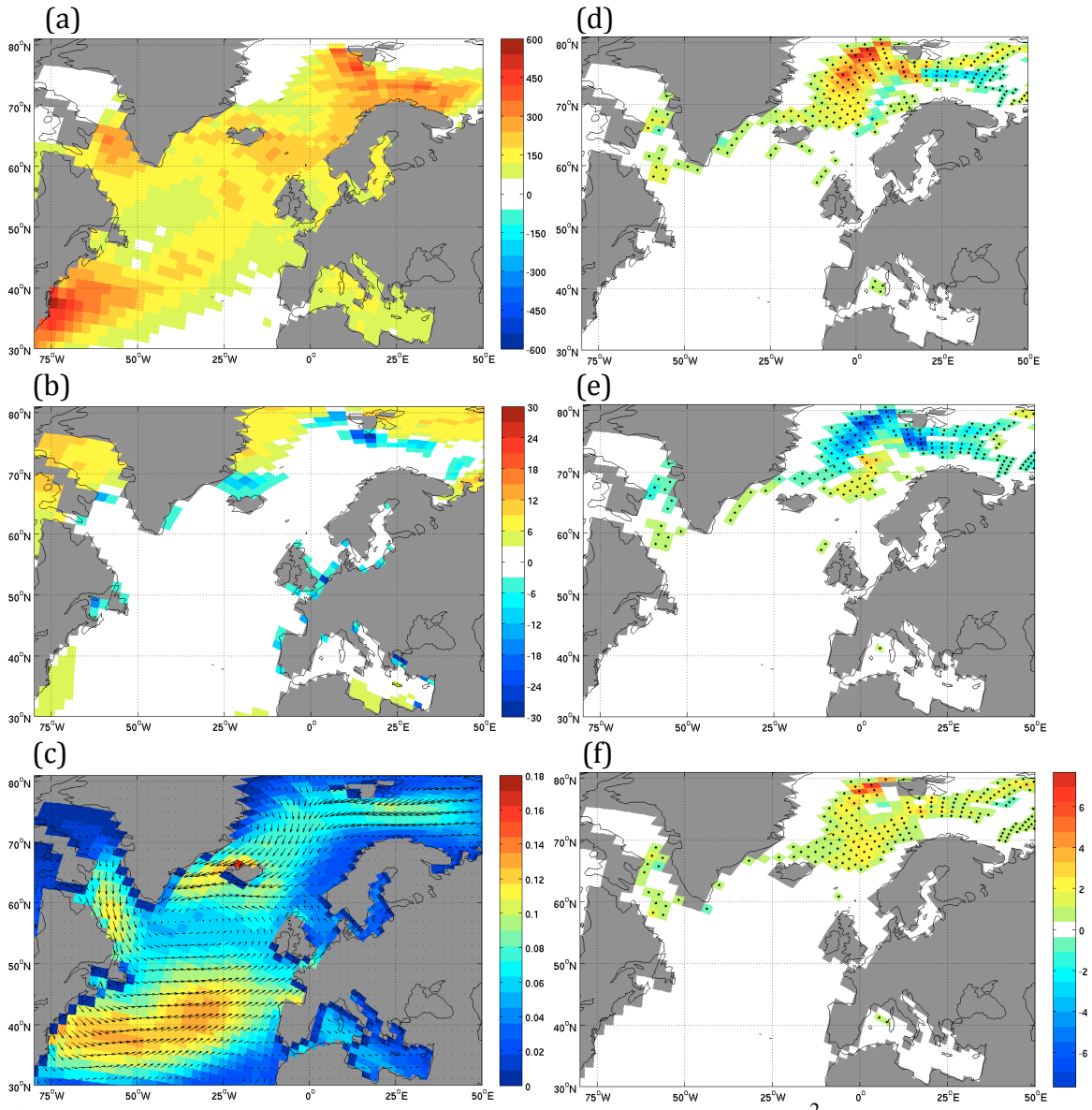

Fig. 6 Long term average winter (Nov-Apr) (a) heat flux (W m^{-2}), where positive values indicate heat lost from the ocean to the atmosphere, (b) freshwater flux (mm day^{-1}), where negative values indicate freshwater added to the ocean, and (c) momentum flux (N m^{-2}), where colour shading shows the strength of the momentum flux and the arrows show the average wind direction. Regression between the winter (Nov-Apr) convection and (d) heat flux, (e) freshwater flux and (f) momentum fluxes filtered with a band-pass filter. Units are given in m convection per standard deviation of forcing, and dotts mark significant correlations at 1% level using a two sided *t*-test and correction of degrees of freedom after the method of Chelton (1983)

As for the Nordic Seas, the PC1 for convection in the Labrador Sea is found to have maximum correlation with all three atmospheric forcing parameters at zero lag (Fig. 7b). The strongest relation is between the convection and the heat flux, with a correlation of 0.51, followed by the freshwater flux (0.45) and the momentum flux (0.41). The average Labrador Sea atmospheric fluxes all have a significant correlation with the positive phase of the NAO

index, giving increased heat loss, less freshwater and stronger winds. The correlations between the NAO index and the fluxes are 0.69, 0.42 and 0.31, respectively at zero time lag.

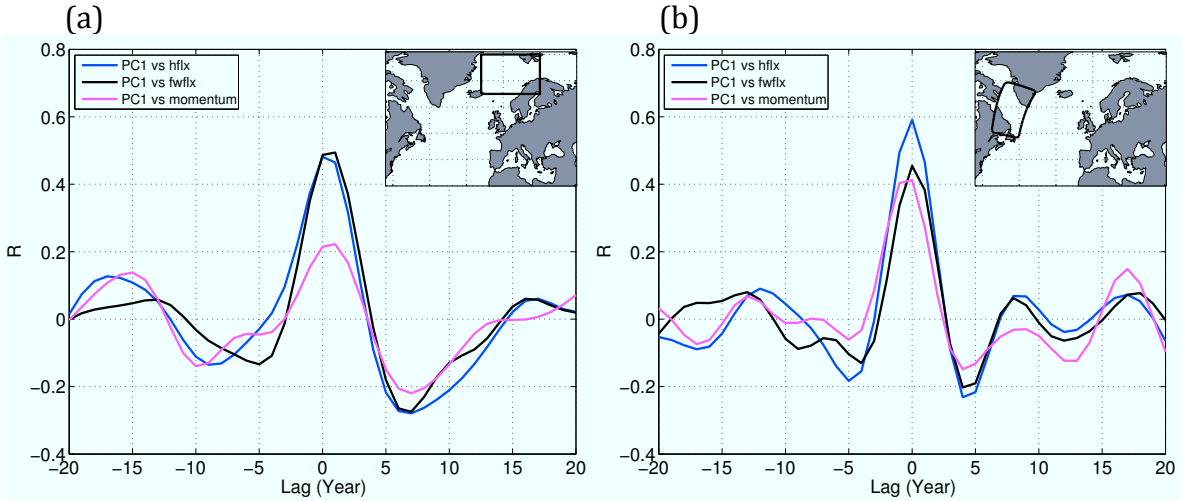

Fig. 7 Cross correlation between the forcing time series of heat (hflx), freshwater (fwflx) and momentum fluxes averaged over the ice free areas within the black box indicated on the maps and the principal component (PC1) of the first EOF of the convection, for (a) the Nordic Seas and (b) the Labrador Sea. The time series have been filtered with a band-pass filter. Positive lags mean the forcing leads

3.5 Volume transport across the Greenland-Scotland Ridge and Newfoundland section

The water crossing the Greenland-Scotland Ridge (GSR) is usually classified into three different water masses (e.g., Hansen and Østerhus 2000; Eldevik et al. 2009); A warm and saline northward flow of Atlantic water (AW) with the Norwegian Atlantic Current (NwAC), a cold and fresh southward flow of polar water (PW) with the East Greenland Current (EGC), and cold and dense southward flow of deep water (DW) with the overflows (Overflowing Deep Water: ODW).

The PW is here defined as the net southward flowing water in the upper 16 density layers (σ_2 < 36.946 kg m^{-3} ≈ σ_0 = 27.622 kg m^{-3}) with salinity less than or equal to 34.7, and temperature less or equal to 8˚C. The net northward flow of AW is correspondingly defined as the rest of the water flowing across the GSR in the upper 16 density layers. The DW is the net southward flowing water beneath layer 16. The definitions of the water masses and corresponding currents are summarized in Table 1 with average water mass properties given in Table 2.

Table 1 Water mass definitions. The water masses are defined using isopycnic layers (σ_2), where some water masses also have additional salinity (S) and potential temperature (T) criteria. LSW and LNADW are taken from a section from Newfoundland to Portugal

Water mass	Water mass flow	Current	σ_2-layer	S, T
AW	Norwegian Atlantic Current	NwAC	1-16	S > 34.7 or T > 8˚C
PW	East Greenland Current	EGC	1-16	S ≤ 34.7 & T ≤ 8˚C
DW	Overflowing Deep Water	ODW	17-35	
LSW	Labrador Sea Water flow	LSWf	17	S < 35.3
LNADW	Entrained Overflowing Deep Water	EODW	18-35	S* < 35.3

*Salinity criteria only for layer 18

Table 2 Average water mass properties; Salinity (S), temperature (T), density (σ_2) and volume transports (flow) for the whole period. Positive volume transports on the GSR indicate net southward transport. The LSW and LNADW flow is only representing the southward transport within the criteria given in Table 1. The hydrography is averaged for water in the net flow direction

Water mass	S	T (˚C)	σ_2 (kg m^{-3})	Flow (Sv)
AW	35.70	10.5	36.252	-7.4
PW	34.25	3.3	36.410	2.1
DW	35.04	1.4	37.290	5.7
LSW	35.22	4.7	36.946	4.9
LNADW*	35.29	4.0	37.124	8.7

* Large difference in properties across the Mid-Atlantic Ridge (see Langehaug et al., *submitted*)

The location of the currents on the GSR can be seen in Fig. 8a. The Irminger Current is included in the definition of the NwAC and is situated to the east in the Denmark Strait. Time series for the volume transports in the various currents are shown in Fig. 8b. The modelled NwAC is on average 7.4 Sv, ECG 2.1 Sv and ODW 5.7 Sv. From observations, the corresponding values are 8.5 Sv (Østerhus et al., 2005), 0.7-3.0 Sv (Pickart et al. 2005, and references therein) and 6.4 Sv (Olsen et al. 2008), respectively. The modelled transports are in general in good agreement with the observation, and also the partitioning into ~75% and 25% between ODW and EGC agrees fairly well to observations (Hansen and Østerhus 2000).

(a)

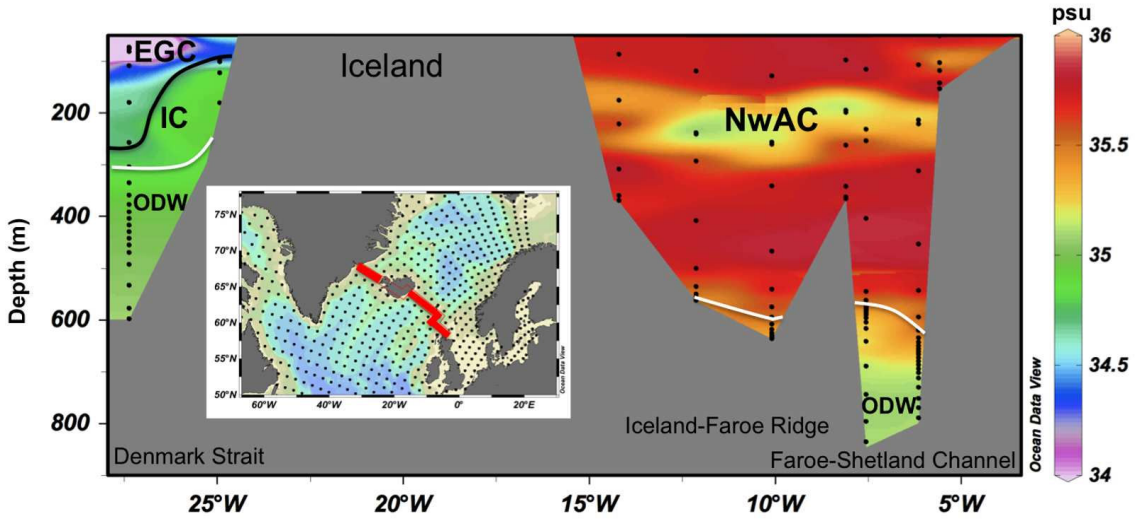

(b)

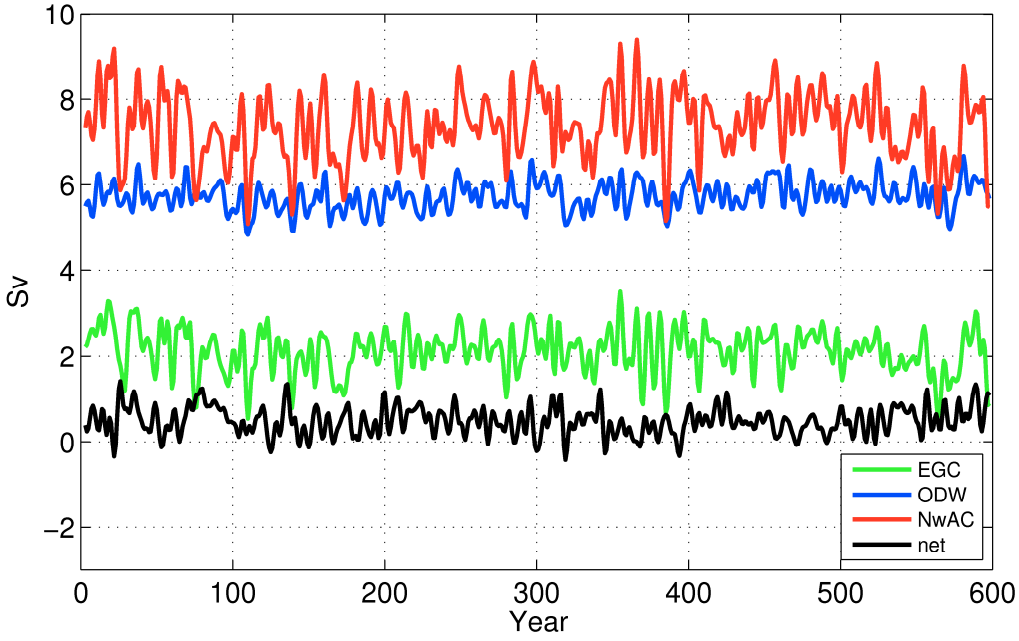

Fig. 8 (a) Cross section of the Greenland-Scotland Ridge, where the salinity is shown in colours. The black line shows the salinity criteria dividing the southward flowing East Greenland Current (EGC) from the northward flowing Irminger Current (IC), which is included in the definition of the Norwegian Atlantic Current (NwAC). White line is the density line dividing the upper flow from the deep overflows (ODW). (b) Low-pass filtered annual volume transports (in Sv) across the ridge. Positive net flow indicates southward flow, where the northward flowing NwAC is weaker than the sum of the southward flowing (EGC and ODW)

The ODW exits the Nordic Seas through two openings, the Faroe-Shetland Channel and the Denmark Strait, which on average contribute with 3.8 Sv and 1.9 Sv, respectively. The overflows in the two sections are anti-correlated, with a correlation coefficient of -0.47. The

variability of the ODW is mainly controlled by the Denmark Strait overflow, where the correlation between the two is 0.82.

On average the total outflow of EGC and ODW, is larger than the inflow across GSR (0.4 Sv net southward transport). This is essentially balanced by the inflow to the Nordic Seas through the Fram Strait (1.1 Sv) and the British Channel (0.5 Sv), and the outflow through the Barents Sea opening (1.3 Sv; Table 3). The seeming 0.1 Sv imbalance of the net budget is due to round-off errors when relating the exchanges at GSR to water masses.

Table 3 Long-term annual mean transports in and out of the Nordic Seas calculated relative to a reference salinity of 34.9 and a reference temperature of 0˚C

Section	**Volume (Sv)**	**Salt (kt s^{-1})**	**Heat (TW)**	**Freshwater (mSv)**
British Channel	0.5	18.9	28	-11
Fram Strait	1.1	37.8	-12	55
Barents Sea Opening	-1.3	-48.9	-56	35
Denmark Strait	-3.2	-112.8	-11	-37
Iceland – Faroe	2.2	80.4	91	-55
Faroe – Scotland	0.7	27.1	177	-95
Nordic Seas				
Net (In – Out)	0.0	2.4	217	-108
External		-2.3	-185	78
Storage anomaly		0.0	0	-
Imbalance		-0.1	-32	-
GSR transports				
NwAC	7.4	275.9	307	-169
EGC	-2.1	-74.8	-23	-40
ODW	-5.7	-206.4	-27	22

The water masses south of the GSR have been studied in a section spanning the entire North Atlantic, from Newfoundland (~48˚N) in the west to Portugal (~38˚N) in the east, hereafter called the Newfoundland section (Fig. 9a). The Labrador Sea Water (LSW) in this section is defined as the water in layer 17 with salinity less than 35.3 (according to Langehaug et al. *submitted*), forming the upper part of the Deep Western Boundary Current at the exit of the Labrador Sea. In the deep basins on either side of the mid-Atlantic ridge (layer 19-35), we have the Lower North Atlantic Deep Water (LNADW). The upper layer of LNADW (layer 18) in the western Atlantic basin has the same salinity criteria as the LSW. This is due to the

presence of higher salinity Mediterranean water on the eastern side of the mid-Atlantic ridge (Langehaug et al. *submitted*), which we do not want to include in the deep water from the northern source region. A summary of the definitions of the water masses is given in Table 1.

(a)

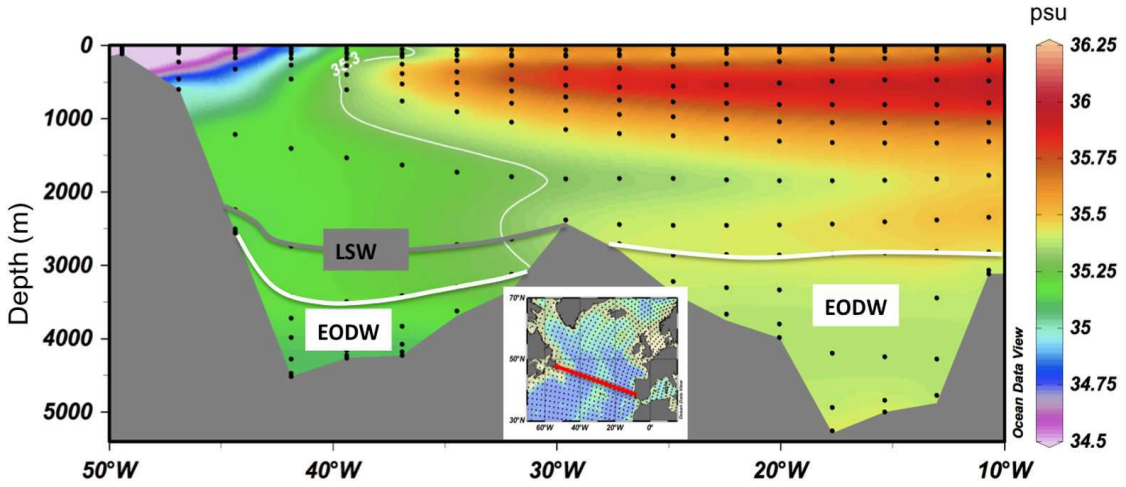

(b)

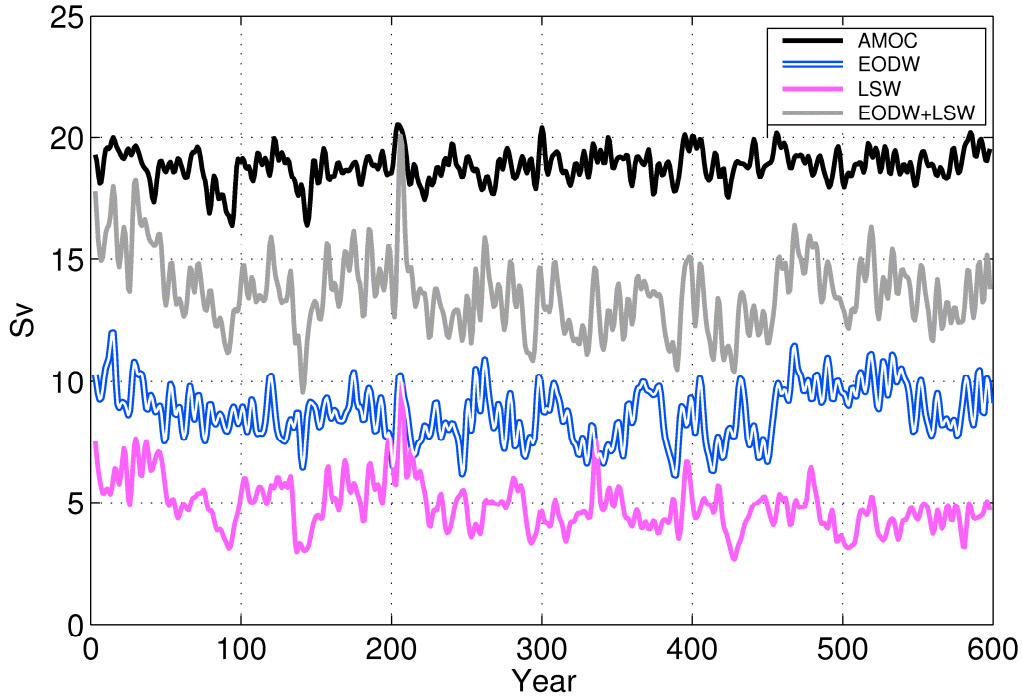

Fig. 9 (a) Average salinity in the Newfoundland cross section (colours) and the location of the Labrador Sea Water (LSW; gray line) together with the upper limit of the Entrained Overflowing Deep Water (EODW; thick white line). The thin white line marks the salinity criteria for LSW and EODW. (b) The northward volume transport aloft (Atlantic Meridional Overturning Circulation - AMOC) together with the southward volume transports of EODW and LSW derived from the section shown in (a). The sum of EODW and LSW (gray line) together makes up the lower limb of the AMOC. Transports are given as absolute values

As the ODW cascades down the steep slope of the GSR it mixes with the ambient warm and saline Atlantic water, increases in volume and decreases in density. Fig. 10 shows which density layer that is situated at the bottom, which gives and indication of where strong diapycnal mixing occurs in the model. Areas with large changes in density across sloping topography, such as at the GSR, are associated with substantial entrainment. This involves the surrounding Atlantic water being mixed into the ODW as it descends down the steep slopes of the GSR. The main areas of entrainment into the ODW are downstream of the Denmark Strait and the Faroe-Shetland Channel, where the layer situated at the bottom changes rapidly downstream. The same areas of entrainment are also found in Dickson and Brown (1994) and Xu et al. (2010). The decrease in density of the DW as a consequence of the entrainment south of the ridge can be seen in Fig. 11 (transition from filled to open blue circles). The cold and dense ODW becomes both more saline and warmer as it is transported toward the Newfoundland section.

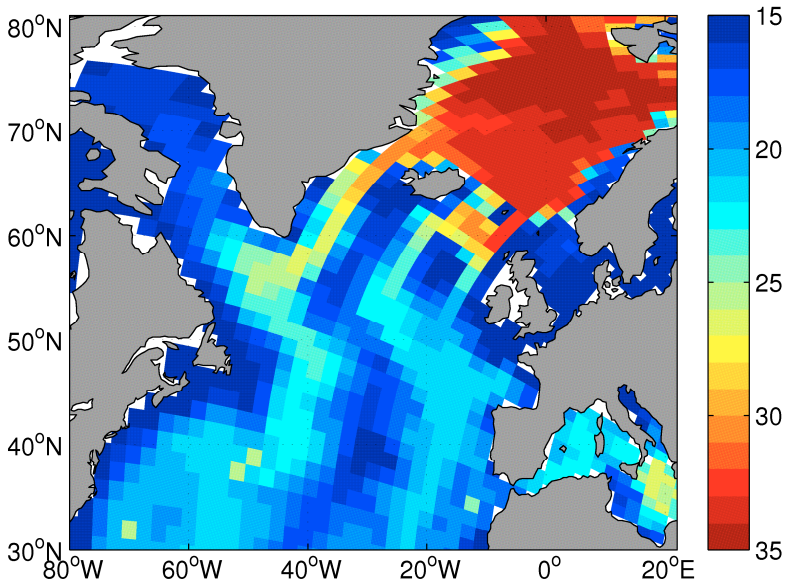

Fig. 10 Isopycnic layer situated at the bottom of each grid cell, which points to where strong diapycnal mixing occurs. Only layers with a thickness exceeding 0.5 m are included. Colours show layer number

The increased volume transport associated with Nordic Seas deep water can be seen in the Newfoundland section (Fig. 9a) as Entrained Overflowing Deep Water (EODW) around two years later (not shown). The water entrained into the ODW downstream of the GSR is defined as the difference between the EODW (8.7 Sv) and the ODW (5.7 Sv) two years earlier. The two-year time lag is the estimated time from a signal is found on the ridge until

the same signal is found in the Newfoundland section. This gives an average entrainment of 3 Sv. Dickson and Brown (1994) estimated that the dense overflows double in volume transports due to entrainment, which is somewhat more efficient than found in this model.

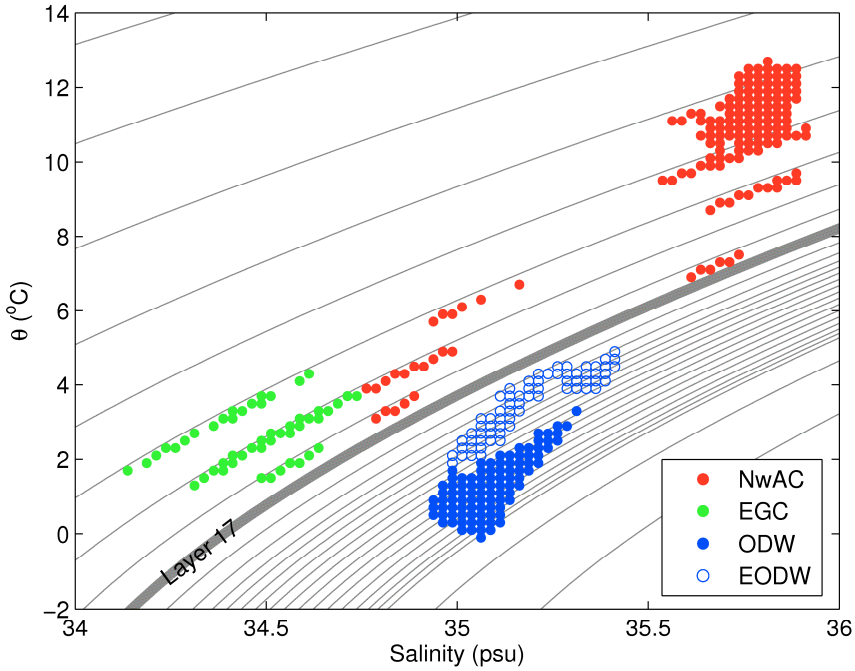

Fig. 11 *TS*-diagram for the net flow crossing the Greenland-Scotland Ridge (dots): Norwegian Atlantic Current (NwAC), East Greenland Current (EGC), Overflowing Deep Water (ODW), and the entrainment of water south of the ridge resulting in the southward flow of Entrained Overflowing Deep Water (EODW) through the Newfoundland section (open circles). Dots are shown for each *TS*-bin with volume transports larger than 0.01 Sv for each *TS*-bin

In addition to the contribution from the Nordic Seas, the convection in the Labrador Sea contributes on average 4.9 Sv to the NADW. The time series for the volume transports in the Newfoundland section are shown in Fig. 9b. There is quite large variability of both the LSW flow and the EODW. The variability of the EODW is mainly due to the entrainment since the ODW is relatively constant in comparison (see Fig. 8b). On average the flow of NADW (EODW + LSW: gray line; 13.6 Sv) is 5.2 Sv lower than the AMOC (18.8 Sv). If we also include the Mediterranean water, the sum is 17.5 Sv. Additional dense water is found in layer 16. This water can not be attributed to any specific source region since it also consists of re-circulated water, hence is omitted from the further analysis. The AMOC co-vary with the flow of NADW (R = 0.45), where the LSW flow dominates the variability of NADW (R = 0.50).

4. Discussion

In the previous section we described the water masses and circulation in the North Atlantic. The main regions of deep convection are found in the Nordic Seas and in the Labrador Sea. The convection in the Labrador Sea has a direct connection with the deep North Atlantic circulation, while the links between the Nordic Seas convection and exchanges across the ridge are more complicated due to the barrier of the GSR. The deep water formed in these two regions make up the bulk part of the North Atlantic Deep Water constituting the lower limb of the AMOC.

4.1 Water mass transformation in the Nordic Seas

In the Bergen Climate Model convection occurs both in the Nordic Seas and in the Labrador/Irminger seas in contrast to many earlier model studies showing deep convection mainly in the Labrador Sea (e.g., Deshayes at al. 2007; Zhu and Jungclaus 2008). For models that have deep convection in the Nordic Seas, convection is mainly associated with the central Greenland Sea (Bentsen et al. 2004; Dong and Sutton 2005; Jungclaus et al. 2005). The convection in this version of the Bergen Climate Model occurs more towards the eastern rim of the Nordic Seas. This is consistent with the concept first introduced by Mauritzen (1996), where the inflowing Atlantic Water gradually looses buoyancy and sinks as it circulates around the basin. This is due to heat loss (while freshwater forcing partly compensates), as has been shown in several other observational studies (Rudels et al. 1999; Segtnan et al. *submitted*).

To elucidate the water mass transformation in the Nordic Seas, volume, heat and freshwater budgets are calculated for the region (Table 3). The volume transport budget for the Nordic Seas is closed, with estimated transports close to observations (cf., Østerhus et al. 2005; Skagseth et al. 2008). In the following, all heat transports/fluxes are given relative to 0˚C. Vertical heat fluxes of 185 TW (1 TW = 1012 W) is lost to the atmosphere within the Nordic Seas. This is in good agreement with recent estimates of 197 TW (Segtnan et al. *submitted*). Comparing with the heat convergence calculated from the oceanic heat transports (217 TW), there is an imbalance in the budget of 32 TW. This is likely due to processes that are not captured by this analysis, such as sub-grid scale eddy activity. Since our budget calculations have been done offline on monthly averaged data, there is also a substantial uncertainty due

to time averaging prior to the calculations. A modest storage anomaly term of -0.05 TW is calculated from the total temperature drift of -0.19˚C over the entire 600-year period.

Looking at the freshwater budget, all transports are calculated relative to a salinity of 34.9. Based on the vertical fluxes, the net freshwater input from evaporation minus precipitation (E-P) and runoff is 78 mSv, which is equivalent to removing salt at a rate of 2.3 kt s^{-1} (kt s^{-1} = 10^6 kg s^{-1}). The external freshwater forcing does not add any volume to the budget, but is rather a "virtual salt flux" accounted for by adjusting the salinity according to the forcing. The external freshwater input in the model compares favourable with recent observational-based estimates of around 55 mSv (Dickson et al. 2007; Segtnan et al. *submitted*). Note that the model includes river runoff to the Baltic Sea and the North Sea, which is not included for in observational-based estimates. The salt and freshwater convergence give a net inflow of 2.4 kt s^{-1} salt to the Nordic Seas, which is equivalent to a net freshwater export of 108 mSv from the Nordic Seas. The imbalance in the budget of -0.1 kt s^{-1} is due to time averaging and sub-grid scale processes as stated above. The change in storage is 0.02 kt s^{-1}, calculated from the total salinity increase of 0.06 psu over the entire 600-year period.

From the freshwater and heat budgets, there is an increase in the Nordic Seas density of around 0.07 kg m^{-3} over the entire period, which is partly due a net heat loss and partly due to a net freshwater export from the Nordic Seas resulting in colder and more saline water. In the model, it is not found that a density difference of this magnitude in the Nordic Seas has any significant consequence for the dynamics. Furthermore, the change in density is not affecting the intensity of the overflow as one should expect (e.g., Curry and Mauritzen 2005). In the model there is a decrease in the steric sea surface height in the Nordic Seas compensating for the change in density (not shown). A similar mechanism has been discussed by Olsen et al. (2008).

Based on the heat and freshwater budgets, the water mass transformation from the warm and saline inflowing AW to the two distinct outflowing water masses, PW and DW can be described. Most of the heat transported across GSR by the NwAC (307 TW, Table 3) is lost to the atmosphere (185 TW) within the Nordic Seas. This can be seen from Fig. 11, where the AW with a temperature of on average 10.5˚C (Table 2) transforms into DW and PW with temperatures of 1.4˚C and 3.3˚C, respectively. The modelled heat transported into the Nordic Seas crossing the GSR compares well with the observational estimates of 313 TW from

Østerhus et al. (2005). The EGC and ODW remove 23 and 27 TW of heat from the Nordic Seas. The southward positive heat transport of the EGC is not seen in observations, as observed temperatures are lower than in the model, where the PW is -1.5˚C and DW 0.5˚C (Rudels et al. 1999; Eldevik et al. 2009).

The circulation in the Nordic Seas can be divided into a horizontal estuarine and a vertical overturning part. To a good approximation, there is a volume balance on GSR both in observations (Hansen et al. 2008) and in the model. Hence there is a strong and significant correlation between the strength of the inflow and outflows at zero lag. The correlation coefficients between the NwAC and the EGC, and the ODW are 0.86 and 0.65, respectively. The weaker correlation between the ODW and EGC (0.44) indicates that the volume transports of the two water masses are depending on two factors: firstly, increased inflow will tend to increase transports in both (positive correlation); whilst, secondly, increased heat loss will tend to increase ODW and decrease EGC transports (negative correlation). Indeed, correlation between the EGC and ODW volume transports when the variability of the NwAC is removed through linear regression gives a significant negative correlation of -0.33. The increase in EGC relative to ODW occurs for negative anomalies in the Nordic Seas density as should be expected (not shown).

4.2 Mechanisms controlling AMOC variability on decadal to multidecadal scale

Labrador Sea convection is forced by heat loss and, to a slightly lesser degree, a negative freshwater flux (mainly due to less precipitation) associated with a positive phase of the North Atlantic Oscillation (NAO+) at zero time lag (Fig. 7b). During NAO+ northerly air masses blow over the Labrador area, where it is found to be colder and dryer than normal (Hurrell 1995), giving favourable conditions for deep convective mixing. In addition, an increased Labrador Sea sea-ice extent is also found at this time, contributing additionally to the convection through brine release.

In order to assess to what extent changes in AMOC are related to convective mixing, the winter convection in each grid cell is regressed onto the AMOC index (Fig. 12). The convection in the Labrador Sea is found to be related to a positive phase of AMOC. Correlating the convection (PC1 from Fig. 5d) with the AMOC index gives a maximum correlation of 0.5 where the convection is leading AMOC by two years. As for the Labrador Sea, the heat and freshwater fluxes, forced by the NAO, contributes to the variability in the

Nordic Seas convection. Here the increased air-sea fluxes are connected to a negative phase of NAO, when fewer storms are bringing warm and moist air masses into the Nordic Seas (Hurrell 1995; Furevik and Nilsen 2005).

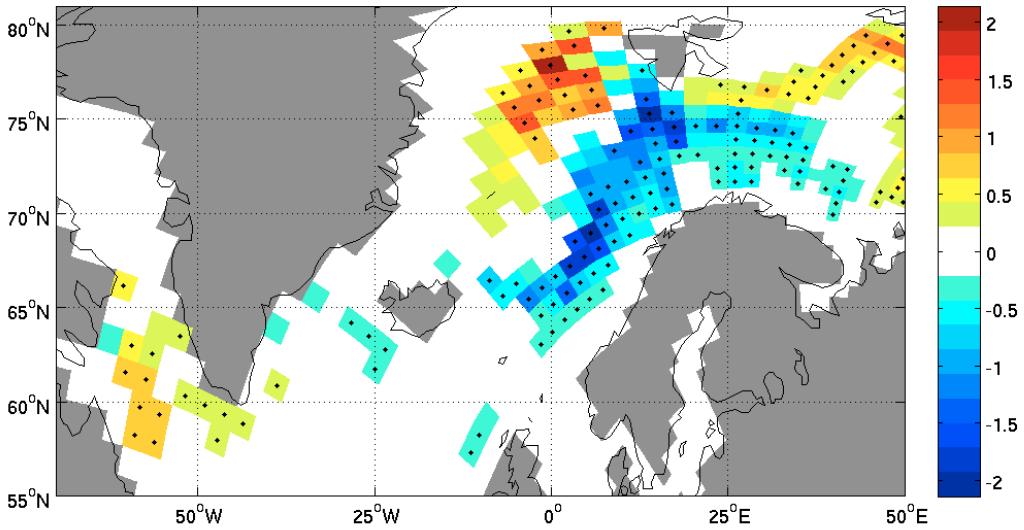

Fig. 12 Regression between winter convection and AMOC. Units are given in m day^{-1} std^{-1} of AMOC. Both time series are filtered using a band-pass filter. Dots indicate significance at 5 % level

So far the results are in agreement with the traditional view that NAO is responsible for the deep water formation, and hence AMOC (e.g., Dickson et al. 1996; Curry et al. 1998; Häkkinen 1999; Eden and Willebrand 2001; Bentsen et al. 2004; Deshayes and Frankignoul 2008). However, there is one important difference in this study: For the Nordic Seas the convection does not determine the water mass exchange across the GRS but is rather a result of it. An increased water mass exchange leads to an increased net poleward heat transport (PHT); the total heat available for northern water mass transformation.

An increased water mass exchange across the GSR is associated with an atmospheric sea level pressure (SLP) pattern (Fig. 13a) very similar to the negative phase of the so-called Scandinavia pattern (Buen and Nakamura 2007; EOF3 of model SLP in the Atlantic sector; Fig. 13b), also called the Eurasian type 1 pattern (Barnston and Livezey 1987). This pattern is dominated by a deep low-pressure anomaly located over Scandinavia and a weaker high-pressure anomaly over Greenland. This atmospheric pattern is associated with stronger than normal northerly winds blowing over the Nordic Seas. The wind has both a direct and an

indirect effect on the water mass exchange, where: 1) The winds set up an increased Ekman transport towards Greenland and the sea ice edge, leading to an elevated sea surface height in the west and reduced in the east, where the along-ridge gradient gives rise to an increased flow across the ridge (Olsen et al. 2008). 2) There is a rapid barotropic adjustment to the surface elevation gradient induced by the Ekman transport (e.g., Nilsen et al. 2003) giving an increased barotropic circulation. Due to volume conservation a strengthening of the Norwegian Atlantic Current and increased PHT will be the consequence. These results also support the findings of Hansen et al. (2010), where they state that the Iceland-Faroe inflow to the Nordic Seas is driven by a pressure gradient due to low sea level in the southern Norwegian Seas.

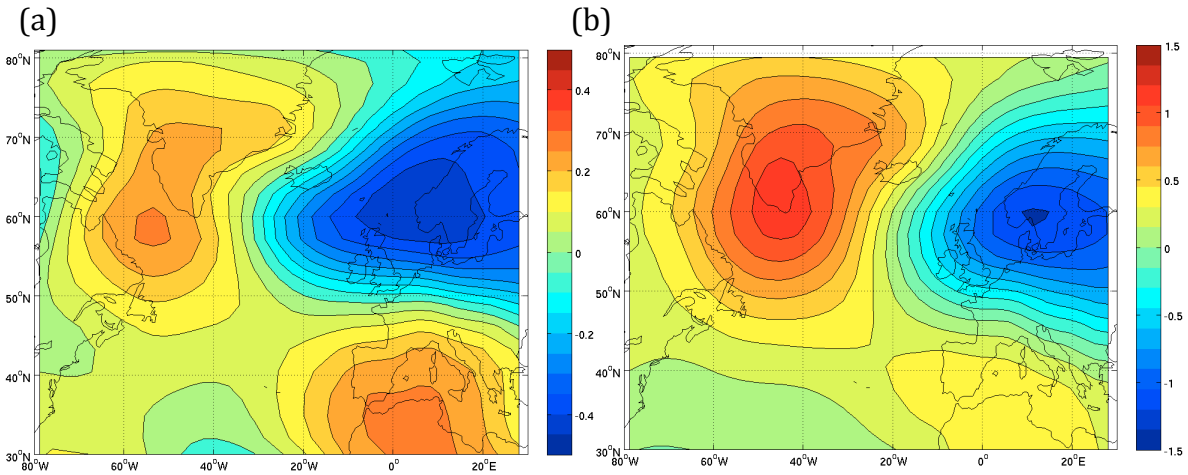

Fig. 13 (a) Correlation between the annual poleward heat transport at the Greenland-Scotland Ridge and the sea level pressure (SLP), where SLP leads by one year (b) negative of EOF3 of the SLP (in hPa std^{-1}), also called the Scandinavian Pattern

The PHT is a measure of the water mass transformation actually taking place within the Nordic Seas, contributing to the ODW across the GSR. It has a correlation with AMOC of 0.41, where PHT is leading AMOC by 3 years. Thus, the deep convective mixing is not necessarily an ideal measure of the total water mass transformation that is taking place in the Nordic Seas (Fig. 4), since some of the deep convection occurring will end up below the sill depth of the GSR, and therefore not contribute directly to the ODW.

Increased heat transport into the Nordic Seas will lead to more sea ice melting, with the increased PHT leading reduced sea ice cover by 3 years. As the sea ice retreats, more water mass transformation will occur through open ocean convection in the central Greenland Sea, concurrent with a decrease in the Norwegian Sea convection, and a decreased total Nordic

Seas convection (from Fig. 4 and Fig. 5a). Furthermore, from Fig. 12 the in-phase relation of the timing of high AMOC and an increased convection in the central Greenland Sea is seen, while there is a reduced convection in the Norwegian Sea. A schematic of the mechanisms leading to an increase in the deep water masses supplying AMOC is given in Fig. 14. Labrador Sea convection has a direct influence on AMOC variability, while the water mass transformation in the Nordic Seas is rather a result of PHT, where increased PHT is both associated with increased water mass exchange on the GSR, and a stronger AMOC.

The two convective regions' influence on AMOC can be further understood through their interaction via the Subpolar Gyre (SPG). In an accompanying paper by Langehaug et al. (*submitted*) a more detailed assessment of North Atlantic/Arctic exchanges including the influence on, and their interaction within the SPG can be found.

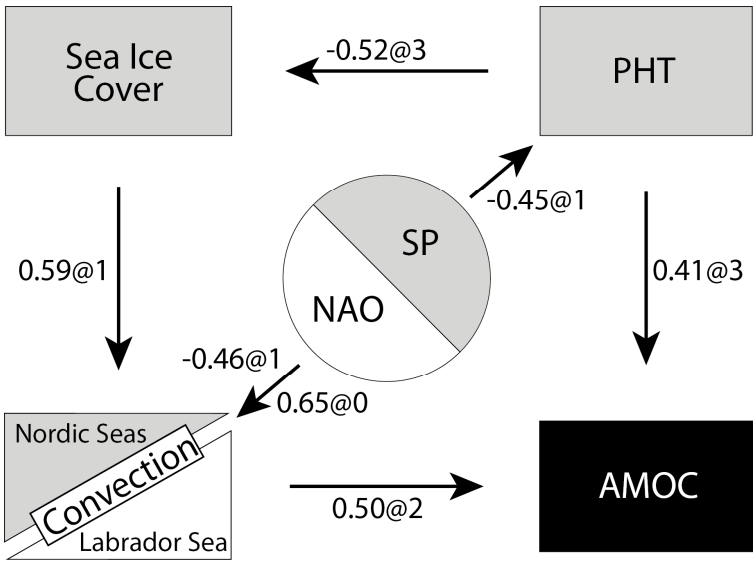

Fig. 14 Schematics of Nordic Seas (gray) and Labrador Sea (white) mechanisms contributing to changes in the modelled AMOC. The circle in the middle represents the atmospheric forcing associated with the North Atlantic Oscillation (NAO) and Scandinavian Pattern (SP), and PHT is the net poleward heat transport across the Greenland-Scotland Ridge. The correlation and time lags (@ in years) between each process is given along the arrows

5. Summary and Conclusions

An increased understanding of the atmospheric and oceanic climate variability is needed for prediction of future climate, where the response to altered air-sea fluxes might play an

important role in the Atlantic oceanic heat transport. In this study we have investigated the mechanism for decadal to multidecadal Atlantic Meridional Overturning Circulation (AMOC) variability in a multi-century, pre-industrial control simulation, using the Bergen Climate Model.

The modelled AMOC is found to be within the observed range of Atlantic overturning, and has increased energy in a 40-70 year frequency band. A novelty with this study is that convective mixing is directly diagnosed in the model, opposed to most previous model studies. Deep-water formation is found both in the Labrador Sea and in the Nordic Seas, but the linkages to the AMOC differ substantially.

The water mass exchange, and hence poleward heat transport (PHT) on the Greenland-Scotland Ridge (GSR) is driven by increased northerly winds associated with the Scandinavian Pattern, the third mode of the sea level pressure in the Atlantic sector. The PHT sets the mode of variability of the convection in the Nordic Seas through the sea ice extent. For high PHT the sea ice edge retracts, resulting in more open ocean convection in the Greenland Sea and less in the Norwegian basin. On average most of the Nordic Seas convection occurs in the Norwegian basin, and a reduction in the Norwegian basin convection is concurrent with an overall decrease in the total Nordic Seas deep-water formation.

Air-sea fluxes, related to opposite phases of the North Atlantic Oscillation (NAO), are contributing to the convection in the Labrador Sea and in the Nordic Seas. For a positive phase of NAO cold and dry air masses contribute to favourable conditions for convection, i.e., stronger wind, increased heat loss and less precipitation, in the Labrador Sea. In the Nordic Seas the same effect of the air-sea fluxes are found during a negative phase of NAO, when there are fewer storms bringing warm and moist air masses into the region.

The Nordic Seas contributes with most of the North Atlantic Deep Water originating in the high northern latitudes (two-thirds when entrainment of ambient water downstream the GSR is included), while the rest is a result of deep convection in the Labrador Sea. The variability in the Labrador Sea convection is forced by the local air-sea fluxes related to NAO, where the convection is directly related to the AMOC. The Scandinavian Pattern, the third mode of atmospheric variability in the North Atlantic, is a driver of the ocean's PHT, the overall

constraint on northern water mass transformation. Increased PHT is both associated with an increased water mass exchange across the GSR, and a stronger AMOC.

Acknowledgements This work has been supported by the Research Council of Norway through the NorClim (IM and TF) and BIAC (HRL and TE) projects. It also contributes to the DecCen project (TF). This publication is no. xxxx from the Bjerknes Centre for Climate Research. Thanks to OH Otterå for providing the model data, and to OH Otterå, M Bentsen, H Drange and PB Rhines for discussions and comments.

References

Bacon S (1997) Circulation and fluxes in the North Atlantic between Greenland and Ireland. *J Phys Oceanogr* **27**:1420-1435

Barnston AG, Livezey RE (1987) Classification, seasonality and persistence of low-frequency atmospheric patterns. *Mon Weather Rev* **115**:1083-1126

Bentsen M, Drange H, Furevik T, Zhou T (2004) Simulated variability of the Atlantic meridional overturning circulation. *Clim Dyn* **22**:701–720. doi: 10.1007/s00382-004-0397-x

Biastoch A., Böning CW, Getzlaff J, Molines JM, Madec G (2008) Causes of interannual-decadal variability in the meridional overturning circulation of the mid-latitude North Atlantic Ocean. *J Clim* **21**:6599–6615. doi: 10.1175/2008JCLI2404.1

Bleck R, Rooth C, Hu D, Smith LT (1992) Salinity-driven thermocline transients in a wind- and thermohaline-forced isopycnic coordinate model of the North Atlantic. *J Phys Oceanogr* **22**:1486–1505.

Bryden H, Longworth HR, Cunningham SA (2005) Slowing of the Atlantic meridional overturning circulation at 25˚N. *Nature* **438**:655-657. doi: 10.1038/nature04385

Buen C, Nakamura H (2007) Scandinavian pattern and its climatic impacts. *Q J R Meteorol Soc* **133**:2117-2131. doi: 10.1002/qj.173

Chelton DB (1983) Effects of sampling errors in statistical estimation. *Deep-Sea Res* **30**:1083-1101

Clarke RA (1984) Transport through the Cape Farewell-Flemish Cap section. *Rap Proces* **185**:120-130

Clarke RA, Gascard JC (1983) The formation of Labrador Sea water. Part I: Large scale processes. *J Phys Oceanogr* **13**:1764-1778

Cunningham SA, Kanzow T, Rayner D, Baringer MO, Johns WE, Marotzke J, Longworth HR, Grand EM, Hirschi JJM, Beal LM, Meinen CS, Bryden HL (2007) Temporal variability for the Atlantic Meridional Overturning Circulation at 26.5˚N. *Science* **317**:935-937. doi: 10.1126/science.1141304

Cunningham SA, Marsh R (2010) Observing and modeling changes in the Atlantic MOC. *Wiley Interdiscip Rev: Clim Change* **1**:180-191. doi: 10.1002/wcc.22

Curry R, Mauritzen C (2005) Dilution of the northern North Atlantic Ocean in recent decades. *Science* **308**:1772-1774. doi: 10.1126/science.1109477

Curry R, McCartney MS (2001) Ocean gyre circulation changes associated with the North Atlantic Oscillation. *J Phys Oceanogr* **31**:3374-3400

Curry R, McCartney MS, Joyce TM (1998) Oceanic transport of subpolar climate signals to mid-depth subtropical waters. *Nature* **391**:575-577

Delworth TL, Greatbatch RJ (2000) Multidecadal thermohaline circulation variability driven by atmospheric surface flux forcing. *J Clim* **13**:1481-1495

Delworth TL, Manabe S, Stouffer RJ (1993) Interdecadal variation in the thermohaline circulation in a coupled ocean-atmosphere model. *J Clim* **6**:1993–2011

Déqué M, Dreveton C, Braun A, Cariolle D (1994) The ARPEGE/IFS atmosphere model: a contribution to the French community climate modelling. *Clim Dyn* **10**:249–266

Deshayes J, Frankignoul C (2008) Simulated variability of the circulation of the North Atlantic from 1953 to 2003. *J Clim* **21**:4919–4933. doi: 11.1175/2008JCLI1882.1

Deshayes J, Frankignoul C, Drange H (2007) Formation and export of deep water in the Labrador and Irminger Seas in a GCM. *Deep-Sea Res I* **54**(4):510-532. doi: 10.1016/j_dsr.2006.10.014

Dickson RJ, Brown J (1994) The production of North Atlantic Deep Water: Sources, rates and pathways. *J Geophys Res* **99**(C6):12319-12341

Dickson R, Lazier J, Meincke J, Rhines P, Swift J (1996) Long-term coordinated changes in the convective activity of the North Atlantic. *Prog Oceanogr* **38**:241– 295

Dickson R, Rudels B, Dye S, Karcher M, Meincke J, Yashayaev I (2007) Current estimates of freshwater fluxes through Arctic and subarctic areas. *Prog Oceanogr* **73**:210-230. doi: 10.1016/j.pocean.2006.12.003

Dong B, Sutton RT (2005) Mechanism of interdecadal thermohaline circulation variability in a coupled ocean-atmosphere GCM. *J Clim* **18**:1117-1135

Eden C, Willebrand J (2001) Mechanisms of interannual to decadal variability of the North Atlantic circulation. *J Clim* **14**:2266–2280

Egbert GD, Ray RD (2000) Significant dissipation of tidal energy in the deep ocean inferred from satellite altimeter data. *Nature* **405**:775-778

Eldevik T, Nilsen JEØ, Iovino D, Olsson KA, Sandø AB, Drange H (2009) Observed sources and variability of Nordic Seas overflow. *Nat Geosci* **2**:406-410. doi: 10.1038/NGEO518

Furevik T, Bentsen M, Drange H, Kindem IKT, Kvamstø NG, Sorteberg A (2003) Description and validation of the Bergen Climate Model: ARPEGE coupled with MICOM. *Clim Dyn* **21**:27–51. doi: 10.1007/s00382-003-0317-5

Furevik T, Nilsen JEØ (2005) Large-Scale Atmospheric Circulation Variability and its Impacts on the Nordic Seas Ocean Climate - a review. In: Drange H, Dokken T, Furevik T, Gerdes R, Berger W (ed) *The Nordic Seas: An Integrated Perspective*, AGU Monograph 158, American Geophysical Union, Washington DC, pp 105-136

Gade HG, Gustafsson KE (2004) Application of classical thermodynamic principles to the study of oceanic overturning circulation. *Tellus* **56A**:371-386

Ganachaud A (2003) Large-scale mass transports, water mass formation, and diffusivities estimated from World Ocean Experiment (WOCE) hydrographic data. *J Geophys Res* **108**(C7):3213. doi: 10.1029/2002JC001565

Ganachaud A, Wunsch C (2000) Improved estimates of global ocean circulation, heat transport and mixing from hydrographic data. *Nature* **408**:453-457

Gaspar P (1988) Modeling seasonal cycle of the upper ocean. *J Phys Oceanogr* **18**:161-180

Gregory JM, Dixon KW, Stouffer RJ, Weaver AJ, Driesschaert E, Eby M, Fichefet T, Hasumi H, Hu A, Jungclaus JH, Kamenkovich IV, Levermann A, Montoya M, Murakami S, Nawarath S, Oka A, Sokolow AP, Thorpe RB (2005) A model intercomparison of changes in the Atlantic thermohaline circulation in response to increasing atmospheric CO_2 consentration. *Geophys Res Lett* **32**:L12703. doi: 10.1029/2005GL023209

Häkkinen S (1999) Variability of the simulated meridional heat transport in the North Atlantic for the period 1951- 1993. *J Geophys Res* **104**(C5):10991–11007

Hansen B, Hátún H, Kristiansen R, Olsen SM, Østerhus S (2010) Stability and forcing of the Iceland-Faroe inflow of water, heat and salt to the Arctic. *Ocean Sci* **6**:1013-1026. doi: 10.5194/os-6-1013-2010

Hansen B, Østerhus S (2000) North Atlantic-Nordic Seas exchanges. *Prog Oceanogr* **45**:109-208

Hansen B, Østerhus S, Turrell WR, Jónsson S, Valdimarsson H, Hátún H, Olsen SM (2008) The inflow of Atlantic Water, heat, and salt to the Nordic Seas across the Greenland-Scotland Ridge. In: Dickson RR, Meincke J, Rhines P (ed) *Arctic-Subarctic Ocean fluxes*, Springer Netherlands, Chap. 1, pp 15-43. doi: 10.1007/978-1-4020-6774-7_2

Holland MM, Bitz CM, Eby M, Weaver AJ (2001) The role of ice-ocean interactions in the variability of the North Atlantic thermohaline circulation. *J Clim* **14**:656-675

Hurrell JW (1995): Decadal trends in the North Atlantic Oscillation: Regional temperatures and precipitation. *Science* **269**(5224):676-679

Johnson GC (2008) Quantifying Antarctic Bottom Water and North Atlantic Deep Water volumes. *J Geophys Res* **113**:C05027. doi: 10.1029/2007JC004477

Jungclaus JH, Haak H, Latif M, Mikolajewicz U (2005) Arctic – North Atlantic interactions and multidecadal variability of the meridional overturning circulation. *J Clim* **18**:4013-4031

Kraus EB, Turner JS (1967) A one-dimensional model of the seasonal thermocline II. The general theory and its consequences. *Tellus* **19**:98-106. doi: 10.1111/j.2153-3490.1967.tb01462.x

Kuhlbrodt T, Griesel A, Montoya M, Levermann A, Hofmann M, Rahmstorf S (2007) On the driving processes of the Atlantic Meridional Overturning Circulation. *Rev Geophys* **45**:RG2001. doi: 10.1029/2004RG00166

Lozier MS (2010) Deconstructing the Conveyor Belt. *Science* **328**:1507-1511. doi: 10.1126/science.1189250

Lumpkin R, Speer K (2003) Large-scale vertical and horizontal circulation in the North Atlantic Ocean. *J Phys Oceanogr* **33**:1902-1920

Mauritzen C (1996) Production of dense overflow waters feeding the North Atlantic across the Greenland–Scotland Ridge. Part 1: Evidence for a revised circulation scheme. *Deep-Sea Res I* **43**(6):769-806

McManus JF, Francois R, Gherardi JM, Keigwin L, Brown-Leger S (2004) Collapse and rapid resumption of Atlantic meridional circulation linked to deglacial climate changes. *Nature* **428**:834-837. doi: 10.1038/nature02494

Medhaug I, Furevik T (2011) North Atlantic 20th century multidecadal variability in coupled climate models: Sea surface temperature and ocean overturning circulation. *Ocean Sci Discuss* **8**:353-396. doi: 10.5194/osd-8-353-2011

Meehl GA, Stocker TF, Collins WD, Friedlingstein P, Gaye AT, Gregory JM, Kitoh A, Knutti R, Murphy JM, Noda A, Raper SCB, Watterson IG, Weaver AJ, Zhao ZJ (2007) Global Climate Projections. In: Solomon S, Qin D, Manning M, Chen Z, Marquis M, Averyt KB, Tignor M, Miller HL (ed) *Climate Change 2007: The Physical Science Basis. Contribution of Working group I to the Fourth Assessment Report of the Intergovernmental Panel on Climate Change*, Cambridge University Press, Cambridge, United Kingdom and New York, NY, USA

Munk W, Wunsch C (1998) Abyssal recipes II: Energetics of tidal and wind mixing. *Deep-Sea Res I* **45**:1977-2010

Nilsen JEØ, Gao Y, Drange H, Furevik T, Bentsen M (2003) Simulated North Atlantic - Nordic Seas water mass exchanges in an isopycnic coordinate OGCM. *Geophys Res Lett* **30**(10):1536. doi: 10.1029/2002GL016597

Olsen SM, Hansen B, Quadfasel D, Østerhus S (2008) Observed and modelled stability of overflow across the Greenland-Scotland ridge. *Nature* **455**:519-522. doi: 10.1038/nature07392

Orre S, Smith JN, Alfimov V, Bentsen M (2009) Simulating transport of ^{129}I and idealized tracers in the northern North Atlantic Ocean. *Environ Fluid Mech* **10**(1-2):213-233. doi: 10.1007/s10652-009-9138-3

Østerhus S, Turrell WR, Jónsson S, Hansen B (2005): Measured volume, heat and salt fluxes from the Atlantic to the Arctic Mediterranean. *Geophys Res Lett* **32**:L07603. doi: 10.1029/2004GL022188

Otterå OH, Bentsen M, Bethke I, Kvamstø NG (2009) Simulated pre-industrial climate in Bergen Climate Model (version 2): model description and large scale circulation features. *Geosci Model Dev* **2**:197–212

Otterå OH, Bentsen M, Drange H, Sou L (2010) External forcing as a metronome for Atlantic multidecadal variability. *Nat Geosci* **3**:688-694. doi: 10.1038/ngeo955

Pickart RS, Straneo F, Moore GWK (2003) Is Labrador Sea Water formed in the Irminger basin? *Deep-Sea Res I* **50**:23-52. doi: 10.1016/S0967-0637(02)00134-6

Pickart RS, Torres DJ, Fratantoni PA (2005) The East Greenland spill jet. *J Phys Oceanogr* **35**:1037-1053

Rhines P, Häkkinen S, Josey SA (2008) Is oceanic heat transport significant in the climate system? In: Dickson RR, Meincke J, Rhines P (ed) *Arctic-Subarctic Ocean fluxes*, Springer Netherlands, Chap. 4, pp 87-109. doi: 10.1007/978-1-4020-6774-7_5

Rudels B, Friedrich HJ, Quadfasel D (1999) The Arctic Circumpolar Boundary Current. *Deep-Sea Res II* **46**:1023–1062

Salas-Mélia D (2002) A global coupled sea ice-ocean model. *Ocean Model* **4**:137–172. doi: 10.1016/S1463.4003(01)00015-4

Schlesinger ME, Ramankutty N (1994) An oscillation in the global climate system of period 65-70 years. *Nature* **367**:723-726

Schott FA, Lee TN, Zantopp R (1988) Variability of structure and transport of the Florida Current in the period range of days to seasonal. *J Phys Oceanogr* **18**:1209-1230

Skagseth Ø, Furevik T, Ingvaldsen R, Loeng H, Mork KA, Orvik KA, Ozhigin V (2008) Volume and heat transports to the Arctic Ocean via the Norwegian and Barents Seas. In: Dickson RR, Meincke J, Rhines P (ed) *Arctic-Subarctic Ocean fluxes*, Springer Netherlands, Chap. 2, pp 45-64. doi: 10.1007/978-1-4020-6774-7_3

Smethie WM, Fine RA (2001) Rates of North Atlantic Deep Water formation calculated from chlorofluorocarbon inventories. *Deep-Sea Res I* **48**:189-215. doi: 10.1016/S0967(00)00 048-0

Talley LD, Reid JL, Robbins PE (2003) Data-based meridional overturning streamfunctions for the global ocean. *J Clim* **16**:3213-3226

Vellinga M, Wood R (2002) Global climatic impacts of a collapse of the Atlantic thermohaline circulation. *Clim Change* **54**:251–267

Vellinga M, Wu P (2004) Low-latitude freshwater influence on centennial variability of the Atlantic thermohaline circulation. *J Clim* **17**:4498-4511. doi: 10.1175/3219.1

Willis JK (2010) Can in situ floats and satellite altimeters detect long-term changes in Atlantic Ocean overturning? *Geophys Res Lett* **37**:L06602. doi: 10.1029/2010GL042372

Wunsch C (2002) What is the thermohaline circulation? *Science* **298**:1180-1181

Xu X, Schmitz WJ Jr., Hurlburt HE, Hogan PJ, Chassignet EP (2010) Transport of Nordic Seas overflow water into and within the Irminger Sea: An eddy-resolving simulation and observations. *J Geophys Res* **115**:C12048. doi: 10.1029/2010JC006351

Zhu X, Jungclaus J (2008) Interdecadal variability of the meridional overturning circulation as an ocean internal mode. *Clim Dyn* **31**(6):731-741. doi: 10.1007/s00382-008-0383-9

Paper III

Arctic/Atlantic exchanges via the Subpolar Gyre

Langehaug, H. R., I. Medhaug, T. Eldevik and O. H. Otterå

Journal of Climate, (submitted)

Arctic/Atlantic exchanges via the Subpolar Gyre

H. R. Langehaug[1,2], I. Medhaug[2,3], T. Eldevik[2,3] and O. H. Otterå[2,4]

[1]*Nansen Environmental and Remote Sensing Center, Bergen, Norway*

[2]*Bjerknes Centre for Climate Research, Bergen, Norway*

[3]*Geophysical Institute, University of Bergen, Bergen, Norway*

[4]*Uni Bjerknes Center, Bergen, Norway*

Abstract

The decadal variability in the strength and shape of the Subpolar Gyre (SPG) in the North Atlantic has been investigated in a 600-year simulation with the Bergen Climate Model (BCM). This long model integration is well suited for establishing decadal relationships between specific variables, such as the SPG strength and the flow of individual water masses. Despite the relatively coarse resolution in BCM, a rather distinct partition of the warm and saline Atlantic Water, the cold and fresh Polar Water, and the cold and dense Overflow Water is simulated. The atmospheric influence on the SPG strength is reflected in the variability of Labrador Sea Water (LSW), which is largely controlled by the North Atlantic Oscillation (NAO) index. The changes in the amount of LSW and the strength of the Nordic Seas overflow both contribute to changes in the SPG – but in different ways. Typically, an increase of one standard deviation (std) of the overflow (0.2 Sv) corresponds to an intensification of about a half std of the SPG strength (0.9 Sv, 1 Sv = 10^6 m^3 s^{-1}). A similar response is found for an increase of one std in the amount of LSW, but simultaneously the strength of the North Atlantic Current (NAC) increases by a half std (0.4 Sv). A combination of the overflow, the amount of LSW, and the East Atlantic Pattern index predict the decadal variability in the SPG strength relatively well, and can explain 44% of the decadal variability in the SPG strength derived from BCM.

Keywords: Decadal ocean variability, Subpolar gyre, Greenland-Scotland Ridge, water masses, Bergen Climate Model (BCM).

1. Introduction

The subpolar North Atlantic Ocean (Fig. 1) is a region of complex dynamics, playing a key role in the variability of the Earth's climate (Hátún et al., 2005; Schott and Brandt, 2007;

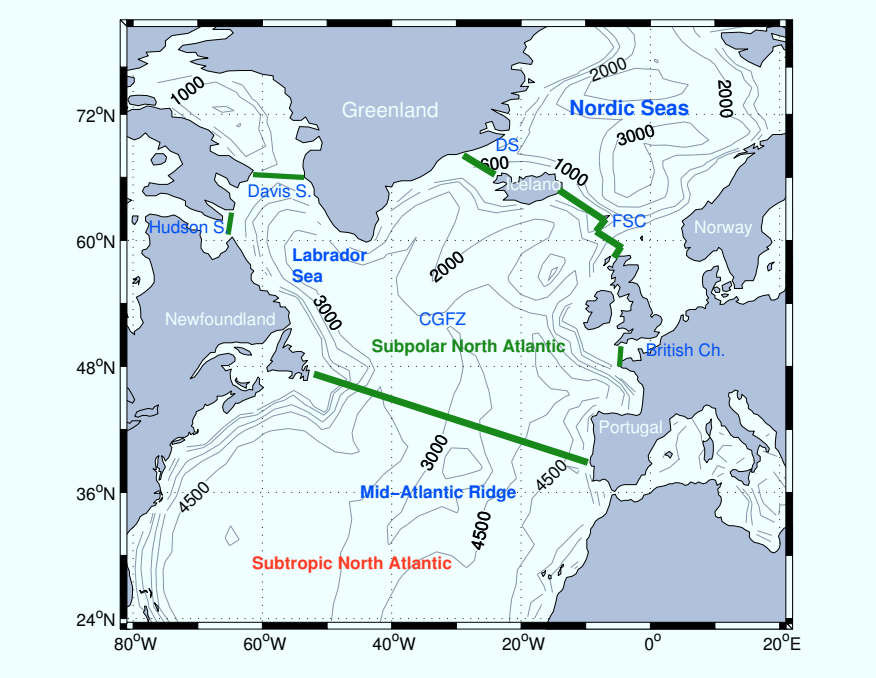

Fig. 1 The model bathymetry (m) of the North Atlantic Ocean and Nordic Seas, with names that are referred to in the text. Abbreviations are: Denmark Strait (DS); Faroe-Shetland Channel (FSC); Charlie Gibbs Fracture Zone (CGFZ). The green sections enclose the subpolar region

Lozier 2010). The cyclonic circulation of the Subpolar Gyre (SPG) is a dominant feature of the subpolar North Atlantic and represents an important part of the Atlantic meridional overturning circulation (AMOC) (Kuhlbrodt et al., 2007). The variable gyre is maintained by buoyancy contrasts and overflows from neighboring seas, as well as wind forcing. The northward flowing eastern branch (above 1000 m) of the gyre includes the North Atlantic Current (NAC, Fig. 2), supplying the SPG with warm, saline water from the subtropics (McCartney and Talley, 1982). In the western part of the SPG cold and fresh Polar Water (PW) are carried by the East Greenland Current (EGC) through the Denmark Strait (Aagaard and Carmack, 1989). The southward export of sea ice and freshwater through the Canadian Archipelago is also feeding the SPG with cold and fresh waters.

In winter, the waters in the SPG are cooled through surface heat loss leading to deep convection and subsequent formation of Labrador Sea Water (LSW; Talley and McCartney, 1982; Curry et al., 1998; Eden and Willebrand, 2001) in the Labrador Sea. At larger depths (below 1000 m) the circulation of LSW and Overflow Water (OW) from the Nordic Seas dominates the SPG circulation (Fig. 2), where LSW circulates at intermediate depths. Cold and dense OW spills over the Greenland-Scotland Ridge (GSR) into the Subpolar basin

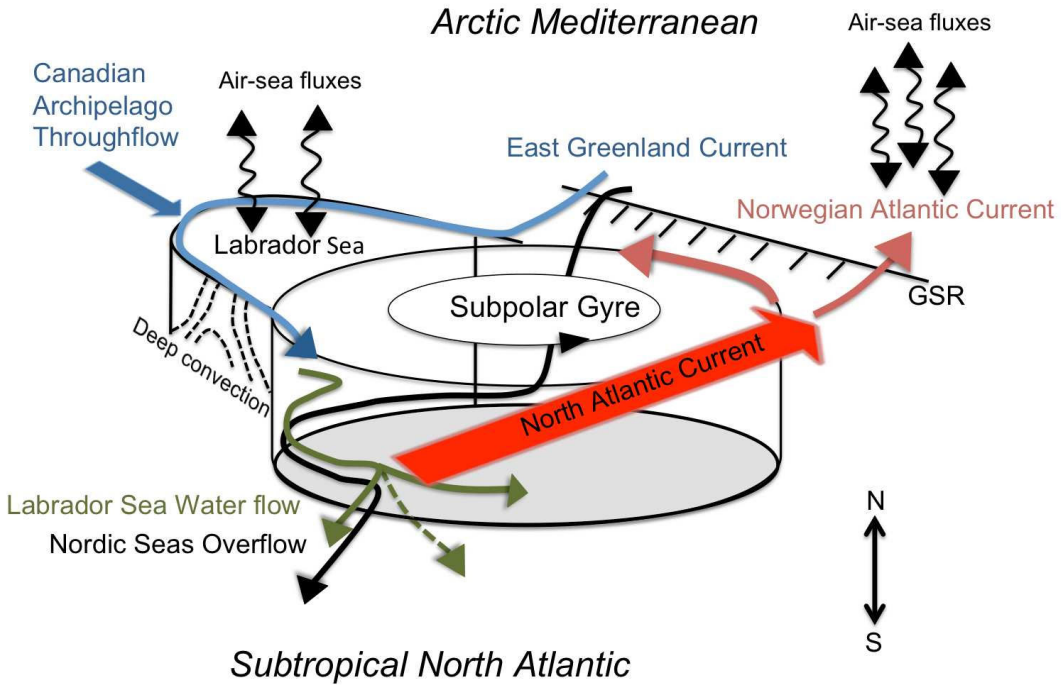

Fig. 2 Schematic of the main circulation in the subpolar North Atlantic

(Dickson and Brown, 1994). The OW from the Nordic Seas is a product of the densification of the Atlantic Boundary Current in the Arctic Mediterranean (comprised of the Nordic Seas and Arctic Ocean; Mauritzen, 1996; Rudels et al., 1999; Eldevik et al., 2009). The Deep Western Boundary Current (DWBC; Smethie et al., 2000; Smethie and Fine, 2001) is the major contributor to the lower limb of the meridional overturning, where the DWBC carries the OW and LSW through the northern North Atlantic to lower latitudes (Lumpkin and Speer, 2003). The total volume transport of the DWBC is about 12.9 Sv (1 Sv = 10^6 m^3 s^{-1}), measured at the southwestern exit of the SPG, east of the Grand Banks near 43ºN (Schott et al., 2004).

Several model studies have investigated the importance of the overflow on the SPG circulation (e.g., Böning et al., 1996; Redler and Böning, 1997; Roberts and Wood, 1997; Born et al., 2009). From a sensitivity experiment with a coupled climate model, Born et al. (2009) found that the model's representation of the overflow had a large influence on the properties and strength of the SPG, where the SPG strength was intensified for an increased overflow. Redler and Böning (1997) suggest that the overflow in the Denmark Strait is the main controlling mechanism for the DWBC downstream, while the changes in the flow through the Faeroe Bank Channel have a smaller effect on the deep transport in the western

basin. Nevertheless, the magnitude and variability of the DWBC is still not well understood (Bacon and Saunders, 2010). While model transports are often compared with observations at the GSR, few model studies have investigated the downstream development of the DWBC (Bacon and Saunders, 2010).

The different water masses in the SPG are, generally, well defined by the precision of hydrographic measurements. However, water mass modification due to diapycnal mixing in the DWBC tends to be poorly resolved in observations (Lauderdale et al., 2008). The nature and complexity of the hydrography and ocean circulation in the subpolar region poses a particular challenge for ocean models. Many important small-scale ocean processes and boundary currents in the northwestern North Atlantic Ocean cannot be resolved in coupled climate models (de Jong et al., 2009). The overflow processes are sub-grid scale in course resolution ocean models, and the models often have too weak overflow (e.g., Bailey et at., 2005; Deshayes et al., 2007). This can be due to a limited model domain that only includes parts of the Arctic Mediterranean where the specified northern boundary conditions constrain the overflow, or diluted overflow because of too vigorous entrainment of ambient water as it cascades down the GSR (e.g., Winton et al., 1998; Lee et al., 2007). An adequate representation of the dense overflow from the Nordic Seas is important when assessing the relative contributions of the deep-water formation in the Labrador and Nordic seas to the circulation of the Atlantic Ocean (Döscher and Redler, 1997; Bailey et al., 2005).

The influence of the atmospheric forcing on the SPG circulation has been investigated in several studies (Eden and Willebrand, 2001; Levermann and Born, 2007; Lohmann et al., 2009). It is well established that the hydrographic properties in the subpolar North Atlantic undergo pronounced variations on decadal-to-centennial time scales, partly as a consequence of changes in the local atmospheric conditions associated with the winter North Atlantic Oscillation (NAO). This contributes to a thickening of the LSW layer due to deep convection, subsequently leading to a strengthening of the SPG (Curry et al., 1998). Lohmann et al. (2009) investigated the response of the SPG to persistent positive NAO forcing. They found that the increase of LSW led to an increased advection of warm and saline subtropical water to the subpolar region, via an increase in the AMOC, which subsequently led to a decline in the SPG strength.

Model studies focusing on the subpolar North Atlantic have so far mostly been restricted to hindcast simulations with Ocean General Circulation Models (OGCM) forced with

atmospheric reanalysis fields (Hátún et al., 2005; Böning et al., 2006; Deshayes and Frankignoul, 2008; Lohmann et al., 2009). Longer time scales can not be investigated in observations because of the limited length of the time series, so that fully coupled climate models remain our most valuable tool to investigate the SPG and the mechanisms controlling its variability on decadal to multidecadal time scales (Delworth and Mann, 2000; Cooper and Gordon, 2002; Gao and Yu, 2008; Born et al., 2009). The proposed mechanisms in OGCM studies (i.e., relationship between the SPG strength and the overflow, formation of LSW, and the AMOC) should also be tested in coupled climate models to establish to what degree such mechanisms are robust among different models and at different time scales (Gao and Yu, 2008).

The main objective of this study is to identify and quantify the controlling factors for decadal-scale variability in the strength of the SPG. In particular, the influence of decadal variations in the different currents flowing into and out of the subpolar region on the SPG will be assessed, with emphasize on the deep branches and the northward flow of Atlantic derived water. For this, a 600-year control simulation with a fully coupled atmosphere-ocean-sea ice model, the Bergen Climate Model (BCM; Otterå et al., 2009), will be used. An advantage with using such a long model integration is the possibility to study mechanisms and natural climate variability on decadal to multidecadal time scales. It is important to understand and identify the natural variability, since the climate of the next few decades will depend as much on natural climate variations as it will on anthropogenic forcing (Cane, 2010).

The paper is organized as follows: The model and the methods used are presented in Section 2. The results from the comparison between modeled and observed hydrography and circulation in specific sections are given in Section 3, followed by an analysis of the relations between the SPG strength and the different inflow/outflow branches to the subpolar region, and the influence of the atmospheric forcing on the SPG strength. Finally, a discussion and summary follows in sections 4 and 5, respectively.

2. Methods

2.1 Model Description

The model run of this study is a 600-year long simulation of the pre-industrial control climate with the Bergen Climate model (BCM), a fully coupled atmosphere-ocean-sea ice

general circulation model. A general description of the model can be found in Furevik et al. (2003) with further information about this version and simulation given in Otterå et al. (2009). Only a brief overview of the model system will be given here.

The model consists of the ocean model MICOM (Miami Isopycnic Coordinate Ocean Model; Bleck et al., 1992) coupled with the atmospheric model ARPEGE/IFS (Action de Recherche Petite Echelle Grande Echelle/Integrate Forecast System; Déqué et al., 1994), and a dynamic-thermodynamic sea ice model (GELATO; Salas-Mélia, 2002). There is no flux adjustment. The model is thus free to evolve its own climate. The only constraint is the seasonal cycle of the incoming solar radiation at the top of the atmosphere.

ARPEGE is run with a truncation at wave number T_L63 on a reduced Gaussian grid, with a resolution of approximately 2.8˚ latitude and longitude and a total of 31 vertical levels, ranging from the surface to 0.01 hPa. The horizontal distribution of continental and marine aerosols, aerosols from desert dust and black carbon are held constant at their respective default values. Concentrations of tropospheric sulphate aerosols are set to pre-industrial level. The atmospheric CO_2 concentration is held fixed at pre-industrial level, and a solar constant of 1370 W m^{-2} is used.

The horizontal ocean grid in MICOM is almost regular with a grid spacing approximately 2.4˚ latitude × 2.4˚ longitude, but to resolve tropically confined dynamics latitudinal grid spacing is gradually decreasing to 0.8˚ near the Equator. The ocean model consists of 34 isopycnic layers below a non-isopycnic mixed layer (ML). The current version of MICOM uses potential density with reference pressure at 2000 decibar (dbar) as vertical coordinate (σ_2-coordinate), whereas the previous version of BCM used 0 db (σ_0-coordinate) as reference pressure. The potential density relative to 2000 dbar ranges from 1030.119 to 1037.800 kg m^{-3} in the isopycnic layers. The pressure gradient force is computed as the gradient of the geopotential on pressure surfaces and the geopotential is found by an accurate integration of the hydrostatic equation using in-situ density.

This simulation is the basis for the climate simulation investigated in Otterå et al. (2010), where the most relevant natural external forcing has been incorporated.

2.2 Statistical methods and study area

The annual values have been low-pass filtered using an 11-year running Bartlett window to filter out high-frequency variability. In the correlation/regression analysis, the time series are further linearly detrended. For significance testing a student *t*-test is used together with the method of Chelton (1983) for estimating the effective number of degrees of freedom; significance refers to a 95% confidence level herein.

The subpolar region is enclosed by five sections as shown in Fig. 1; Newfoundland-Portugal (hereafter referred to as the Newfoundland section), British Channel, Greenland-Scotland Ridge (GSR), Davis Strait, and Hudson Strait. The different water masses present in the two largest sections (Newfoundland and GSR) are defined using σ_2, temperature, and salinity criteria.

The water masses found at the GSR have distinct temperature and salinity properties compared to the water masses present in the Newfoundland section. Hence, the water mass exchange across the GSR will be visualized by use of a volumetric temperature and salinity (*TS*-) diagram. A coherent assessment of water masses in ocean or climate models requires thermohaline model properties to be analyzed according to the methodology routinely applied to observations (e.g., *TS*-diagram). When combining these properties with the corresponding model transports, water mass transformation (e.g., from warm and saline Atlantic water to colder and fresher water in the Nordic Seas) can be quantified (Bailey et al., 2005). The calculation is done in the following manner: The volume transports (in *u*- and *v* direction) in each grid cell are sorted into *TS*-bins for each year. The net volume flux for each *TS*-bin is visualized in a so-called volumetric *TS*-diagram. By summing the volume transport for a given *TS*-domain, the volume transport carrying the associated water mass is the result.

3. Results

3.1 Subpolar Gyre Circulation and transport budget

The mean barotropic streamfunction and mean mixed layer velocity in the North Atlantic are shown in Fig. 3. Both the subpolar (negative streamfunction) and the subtropical gyres (positive streamfunction) are evident, with their anti-clockwise and clockwise circulations, respectively. The North Atlantic Current is strongest at the border between the two gyres.

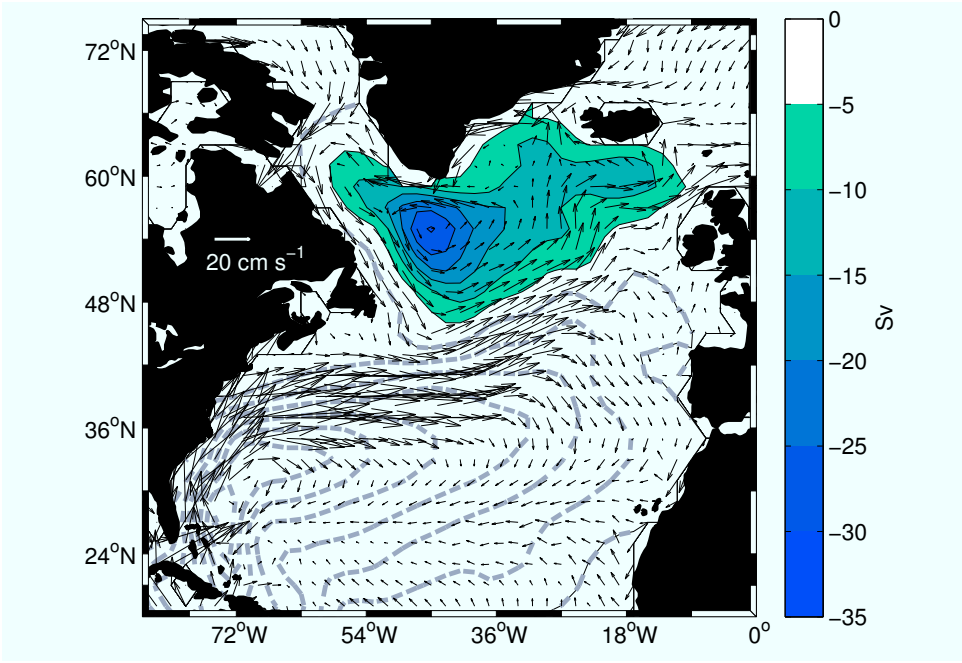

Fig. 3 Mean barotropic streamfunction (contours) with 5 Sv intervals, where filled contours indicate negative and dashed lines indicate positive values. Mean mixed layer velocities are shown by black arrows, with a reference velocity of 20 cm s^{-1}

The SPG has three great arms; one extending toward the Faroe Island, one towards the Denmark Strait, and the last towards the Davis Strait. The mean barotropic streamfunction has a minimum south of Cape Farewell, with an averaged strength of -30 Sv. This compares well with observed estimates that range from -40 to -25 Sv (Clarke, 1984; Bacon, 1997). In this study the SPG strength is simply defined as the absolute value of the minimum streamfunction.

The simulated volume transport estimates for some key sections in the Arctic Mediterranean compare, in general, well with estimates from the observational literature (Otterå et al., 2009). A budget of the volume transports into and out of the subpolar region is given in Table 1. The largest inflow (40.8 Sv) and outflow (42.8 Sv) is captured in the Newfoundland section, which also has the largest net flow (outflow of 2 Sv). This outflow is balanced by the net flow through the remaining sections embracing the subpolar region. It is mainly balanced by the net inflow from the Davis Strait (1.8 Sv), where the inflow is more than four times larger than the outflow. The net inflow at the GSR is 0.5 Sv, while there is a net outflow in British Channel of 0.4 Sv. The net inflow from the Arctic Mediterranean (1.8 Sv) to the subpolar region is due to the net flow through the Bering Strait. In addition, there is a small net inflow from the Hudson Strait, which gives a net inflow of 2 Sv from the four northern sections, balancing the net outflow at the Newfoundland section.

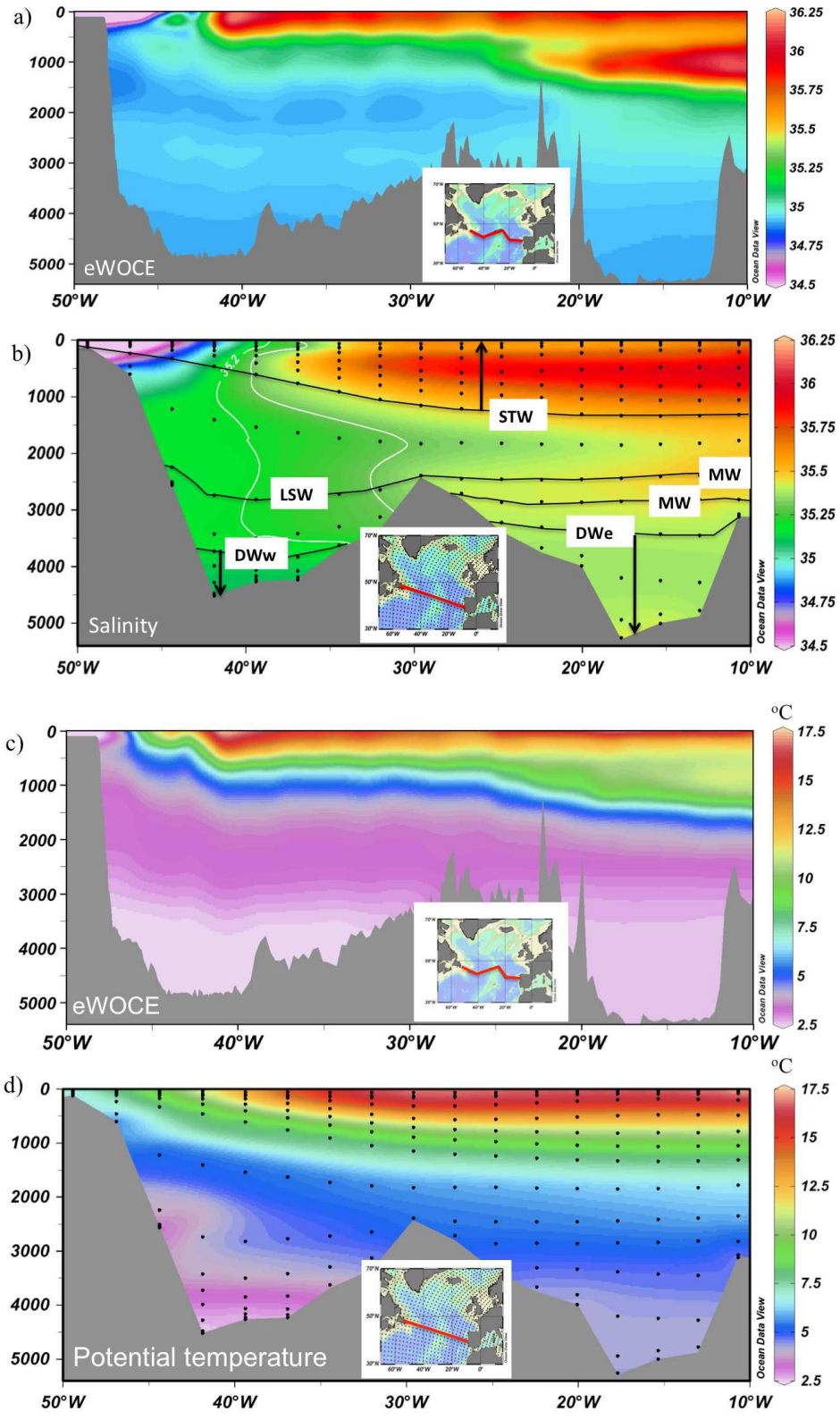

Fig. 4 Salinity and potential temperature (˚C) from WOCE data are shown in a) and c), respectively. Model salinity and potential temperature in the Newfoundland section are shown in b) and d), respectively. Black dots show the center of the grid cells. Marked water masses are Subtropical Water (STW), Labrador Sea Water (LSW), Mediterranean Water (MW), Deep Water west (DWw), and Deep Water east (DWe). Note the difference in the location of the modeled and observed sections

Table 1 Volume transport budget (in Sv) for the subpolar region. Inflow and outflow denote water flowing into or out of the subpolar region, respectively. Net flow is defined as inflow minus outflow

Section	**Inflow**	**Outflow**	**Net flow**
Newfoundland section	40.8	42.8	-2.0
Greenland-Scotland Ridge	9.8	9.3	0.5
Davis Strait	2.3	0.5	1.8
Hudson Strait	1.3	1.1	0.2
British Channel	0	0.4	-0.4
Total	**54.2**	**54.1**	**0.1**

3.2 Observed and simulated hydrography and circulation in the subpolar region

The GSR section and the Newfoundland section will be of prime focus here, since these sections capture the dominant water masses in the subpolar region (Fig. 1). The model temperature and salinity in the Newfoundland and GSR sections are compared to observations to provide a background on the model performance. Observations from the NISE Data Set (Nilsen et al., 2008) at the Greenland-Scotland Ridge and WOCE data (http://www.ewoce.org/) are applied.

3.2.1 Newfoundland section

The WOCE data is from the section given in the small inset in Fig. 4 (a and c). A fresh layer is evident on the western continental slope in the upper 500 m. For the rest of the section the observations show a distinct warm and saline Atlantic layer in the upper 1000 m. The core of the NAC, characterized by salinities up to 36.25, is located west of the Mid-Atlantic Ridge at around 40ºW. A colder and fresher intermediate layer (1500-2500 m) is present west of the Mid-Atlantic Ridge, with the coldest and freshest deep water found below this layer. On the eastern side of the Mid-Atlantic Ridge, between the intermediate layer and the deepest water (2500-3500 m), there is a layer of relatively high salinity.

The spatial structure of the model temperature and salinity in the Newfoundland section compares favourably to the observations, except for the deep eastern part (Fig. 4, b and d). Both the modelled east-west temperature and salinity gradients in the deeper waters are larger than seen in the observations, where the eastern deep waters are particularly warm and saline in the model. The model temperatures and salinities below ~1000 m are in general

Table 2 Definitions of the water masses in the various sections by using σ_2 isopycnals (the vertical level of BCM), salinity (S) and potential temperature (T) criteria

Water mass	**Abbreviation**	**Layers, σ_2** [kg m^{-3}]	**S/T limit**
Subtropical Water	STW	$\sigma_{2,ML}$ - $\sigma_{2,15}$ (= 36.712)	
Labrador Sea Water	LSW	$\sigma_{2,17}$ (= 36.946)	S < 35.3
Mediterranean Water	MW	$\sigma_{2,17}$ - $\sigma_{2,18}$(= 37.020)	S ≥ 35.3
Deep Water west	DWw	$\sigma_{2,19}$ (= 37.074) - $\sigma_{2,35}$	S < 35.2
Deep Water east	DWe	$\sigma_{2,19}$ (= 37.074) - $\sigma_{2,35}$	S ≥ 35.2
Atlantic Water	AW	$\sigma_{2,ML}$ - $\sigma_{2,16}$ (= 36.846)	S > 34.7 & T > 8ºC
Polar Water	PW	$\sigma_{2,ML}$ - $\sigma_{2,16}$ (= 36.846)	S ≤ 34.7 & T ≤ 8ºC
Overflow Water	OW	$\sigma_{2,17}$ - $\sigma_{2,35}$ (= 37.800)	

higher than present-day observations. Another distinct difference between the modelled and observed sections is the location of the core of the northward flowing NAC. The model NAC detach from the American coastline further south (Fig. 3), indicated by an eastward shift in the location in the section compared to in the observations. The observed NAC further curves around Grand Banks before it detaches from the coastline (Schott and Brandt, 2007).

Five water masses are defined in the model Newfoundland section (see Fig. 4b for location and Table 2 for details); Subtropical Water (STW), Labrador Sea Water (LSW), Mediterranean Water (MW), Deep Water east (DWe) and Deep Water west (DWw) of the Mid-Atlantic Ridge. The STW is northward flowing waters in the 15 uppermost layers (above ~1000 m east of the Mid-Atlantic Ridge) and is transported by the NAC. The LSW is southward flowing water in layer 17 (σ_2 = 36.946, corresponding to σ_0 ~ 27.883) and with salinity less than 35.3. The MW is defined as the water with salinity higher or equal to 35.3 in layer 17 and 18. The net flow of this water mass in the Newfoundland section is close to zero, due to recirculation. The DWe is southward flowing waters in layers 19-35 and with salinities higher or equal to 35.2. The DWw is also defined as southward flowing waters in layers 19-35, but with salinity *less* than 35.2. Layer 19 corresponds to σ_0 ~ 27.960 and σ_0 ~ 28.019 for DWw and DWe *TS*-properties, respectively.

The mean model transport of NAC is 26 Sv (Table 3), while the NAC transport entering the eastern basin across 36˚W has been estimated to 21 Sv from observations (above 1000 m

Table 3 Long-term mean volume transport (Flux in Sv) for the currents flowing into (Inflow) and out of (Outflow) the subpolar region. The volume transport for each current is constrained by the water mass definitions of the associated water mass (Table 2). Net flow is defined as inflow minus outflow

Current	**Abbreviation**		**Flux**	**Water mass**
North Atlantic Current	NAC	In	26.0	STW
Labrador Sea Water flow	LSW flow	Out	4.9	LSW
Mediterranean Water flow	MW flow	Out	3.9	MW
Deep Water west flow	DWw flow	Out	3.9	DWw
Deep Water east flow	DWe flow	Out	3.8	DWe
Norwegian Atlantic Current	NwAC	Net	-7.4	AW
East Greenland Current	EGC	Net	2.1	PW
Overflow	Overflow	Net	5.7	OW

depth; Pèrez-Brunius et al., 2004). The modeled transport of DWw is on average 3.9 Sv, which is in good agreement with the observed estimates of 3.8-4.6 Sv (Schott et al., 2004; Dengler et al., 2006). The southward model transport of DWe is 3.8 Sv. The estimated transport of LSW from observations decreases considerably from north to south of Grand Banks, from 11.3 to 3.3 Sv (Schott et al., 2004; Dengler et al., 2006), and the model transport lies within this interval (4.9 Sv).

3.2.2 Greenland-Scotland Ridge

A volumetric *TS*-diagram of the water mass exchanges over the Greenland-Scotland Ridge is given in Fig. 5, since the water masses here have distinct temperature and salinity properties compared to the Newfoundland section. Red and blue bars give the net northward and southward transport, respectively. Three water masses stand out in this section: Atlantic Water (AW) defined as water that moves northward in the uppermost 16 layers with a salinity larger than 34.7 or with a potential temperature higher than 8˚C (see Table 2); Polar Water (PW) defined as water that moves southward in the uppermost 16 layers, with salinity and potential temperature less or equal to 34.7 and 8˚C, respectively; Overflow Water (OW) defined as water that moves southward beneath the PW and AW. The salinity limit (34.7) is applied to distinguish between the PW and AW in the Denmark Strait. In observational studies the northward flowing AW in the Denmark Strait, the Irminger Current, is found to carry salinities above 34.8 (Holliday et al., 2006). The observed characteristics of AW, PW,

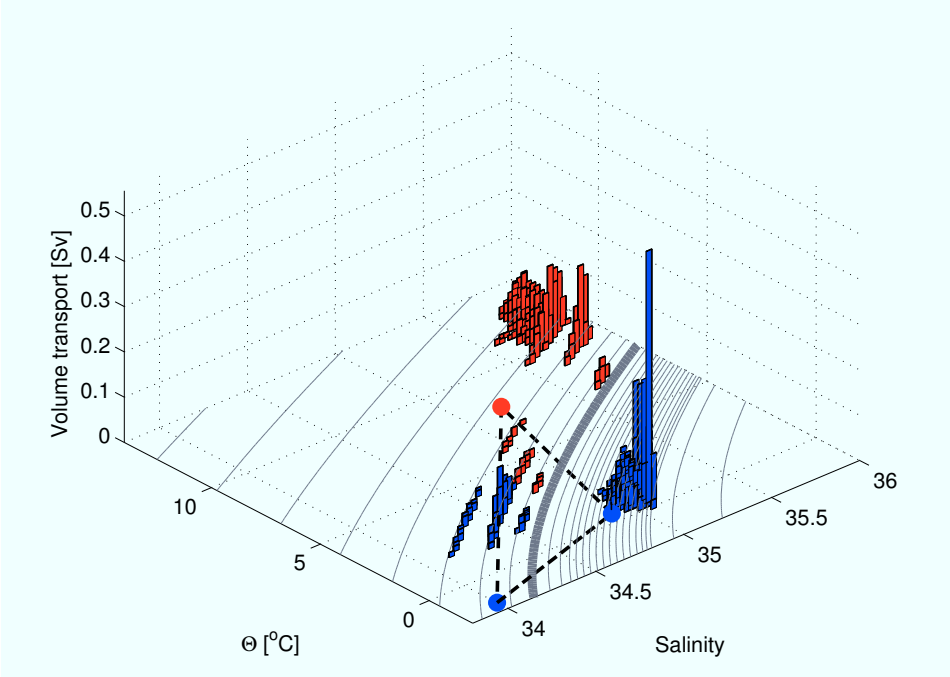

Fig. 5 Volumetric *TS*-diagram for the Greenland-Scotland Ridge. Red (blue) bars denote net northward (southward) volume transport larger than 0.01 Sv within the corresponding *TS*-interval. The dashed triangle shows the observed properties of the three components; Atlantic Water (AW), Polar Water (PW), and Overflow Water (OW) from Rudels et al. (1999) and Eldevik et al. (2009). The σ_2-isolines illustrate the vertical discretization of the model, where the thick grey line is the upper isopycnal (layer 17) defining the OW. The properties of the mixed layer are seen as a continuous distribution of squares for the AW

and OW (Rudels et al., 1999; Eldevik et al., 2009) are shown in Fig. 5 as a dashed triangle. The thermohaline contrasts spanned by the three water masses are similar to the observed, but the model hydrography is skewed towards warmer and more saline water masses, especially for AW and PW.

The volume transports of AW, PW, OW across the GSR, Norwegian Atlantic Current (NwAC), East Greenland Current (EGC), and overflow, are all in good agreement with estimates of the present-day exchanges inferred from current meters. To sort out recirculating water, the net flow within the water mass definitions (given in Table 2) is used. The NwAC is found to be 8.5 Sv in observations (Østerhus et al., 2005), while the average model transport is 7.4 Sv (Table 3). The observation-based estimate of total overflow is 6.4 Sv (Olsen at el., 2008) is in reasonable agreement with the modelled value of 5.7 Sv. The mean model EGC is 2.1 Sv, which may also include water from recirculation of the Irminger Current. From observational estimates this is found to be between 0.4 and 2.1 Sv (Nilsson et al., 2008). The NwAC is located mainly east of Iceland, EGC in the Denmark Strait, and the overflow mainly in the Denmark Strait and the Faroe-Shetland Channel. The correlations

Table 4 Peak correlations (R) between the a) Subpolar Gyre (SPG) strength, b) Labrador Sea Water (LSW) thickness and the variables given in the tables. Time series are low-pass filtered. Subpolar Gyre strength/Labrador Sea Water lags for negative lags (given in yrs). The momentum flux is averaged over the subpolar region and the Labrador Sea (LS), and the heat and freshwater fluxes over the LS. *The time series of the DWe flow contains a non-linear trend. Time scales shorter than 11 yrs and longer than 100 yrs has therefore been removed from the time series by a centred third order Butterworth filter

a)

Variables	**R**	**Lag**
NAC	0.35	+1
LSW flow	0.24	0
DWw flow	0.62	+1
DWe flow*	0.39	+11
NwAC	0.57	-1
EGC	0.43	-1
Overflow	0.43	-1
Sea Surface Height	0.70	-1
Mom. flux in SPG	0.36	-6
EAP index	0.42	-5

b)

Variables	**R**	**Lag**
SPG strength	0.47	0
Heat flux	0.41	-2
Freshwater flux	0.27	-2
Mom. flux in LS	0.33	-1
NAO index	0.59	-1
AMOC index	0.79	0

between the NwAC and the overflow and the EGC are found to be 0.70 and 0.88 at zero lag, respectively. This is due to continuity as the exchanges across GSR are balanced to the first order.

3.3 Water mass exchanges and pathways within the subpolar region

The regression between the SPG strength and the currents crossing the GSR, and Newfoundland sections are shown in Fig. 6. An increase of one standard deviation (std) for the DWw flow is associated with an enhancement of the SPG of 1.3 Sv. Compared to one std of the SPG strength (2 Sv), this change is more than a half std of the SPG strength. The transports of all water masses, except for the flow of DWe, are significantly correlated with the SPG strength (Table 4a). This means that the SPG strength is enhanced when the volume transport crossing the GSR and at the southern exit of the Labrador Sea (close to Newfoundland) increase. The SPG strength has a correlation of 0.43 and 0.62 with the overflow, and flow of DWw, respectively. The overflow and the DWw flow is leading and lagging the SPG strength by one year, respectively. The LSW flow has maximum correlation with the SPG strength at zero lag, while the NAC lags the SPG strength by one year.

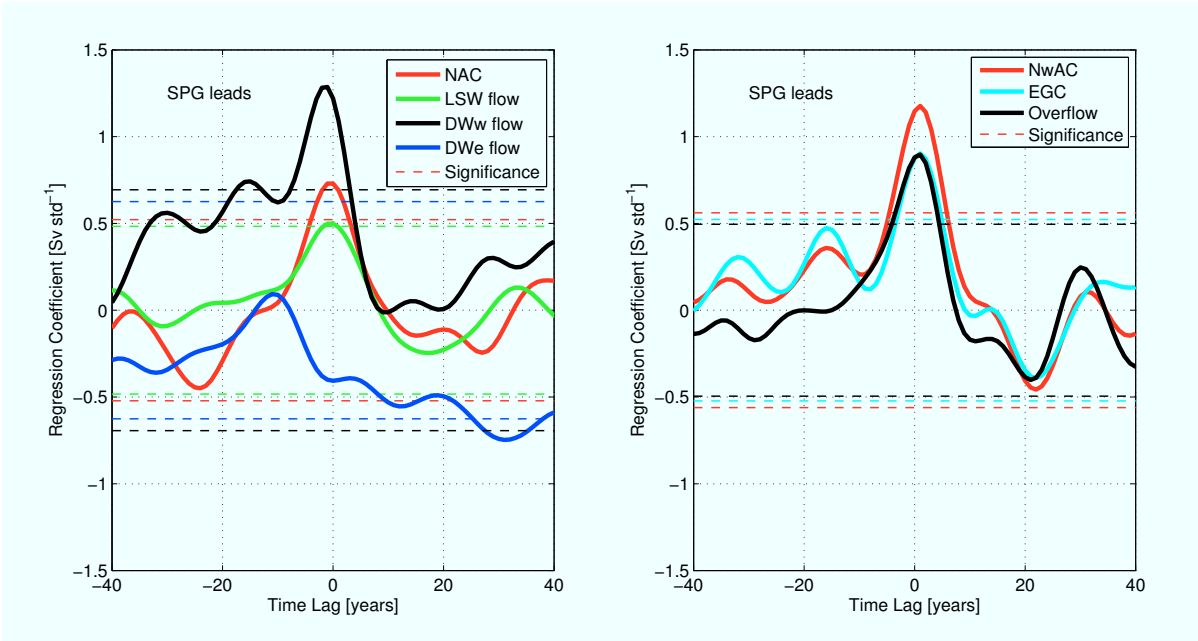

Fig. 6 Subpolar Gyre (SPG) strength regressed on the strength of the different flows across the Newfoundland section (left) and the Greenland-Scotland Ridge (right). An increase of one standard deviation (std) for the DWw flow is associated with an enhancement of the SPG of 1.3 Sv, which is more than a half std of the SPG strength (1 std = 2 Sv). The abbreviations are as given in Table 2.

Fig. 7 illustrates the deep-water pathways within the subpolar region. The colours give the fraction of the total water column occupied by the respective water mass. The DWw is mainly found in the western North Atlantic Basin, while the DWe is only in the eastern part. An upper salinity limit (35.4) is added to the DWe to sort out the contribution from the MW. From the mean velocities in layers 19 to 35 the DWw and DWe appear to originate from the Denmark Strait Overflow (DS) and Faroe-Shetland Channel Overflow (FSC), respectively. The DS and DWw flow have a correlation of 0.6 at three years lag, where the DS is leading. The time series of the DWe flow contains a non-linear trend. Time scales shorter than 11 yrs and longer than 100 yrs has therefore been removed from the time series by a centred third order Butterworth filter. The correlation between DWe flow and the FSC is only slightly above the significance level at three yrs lag (0.28), where the FSC leads.

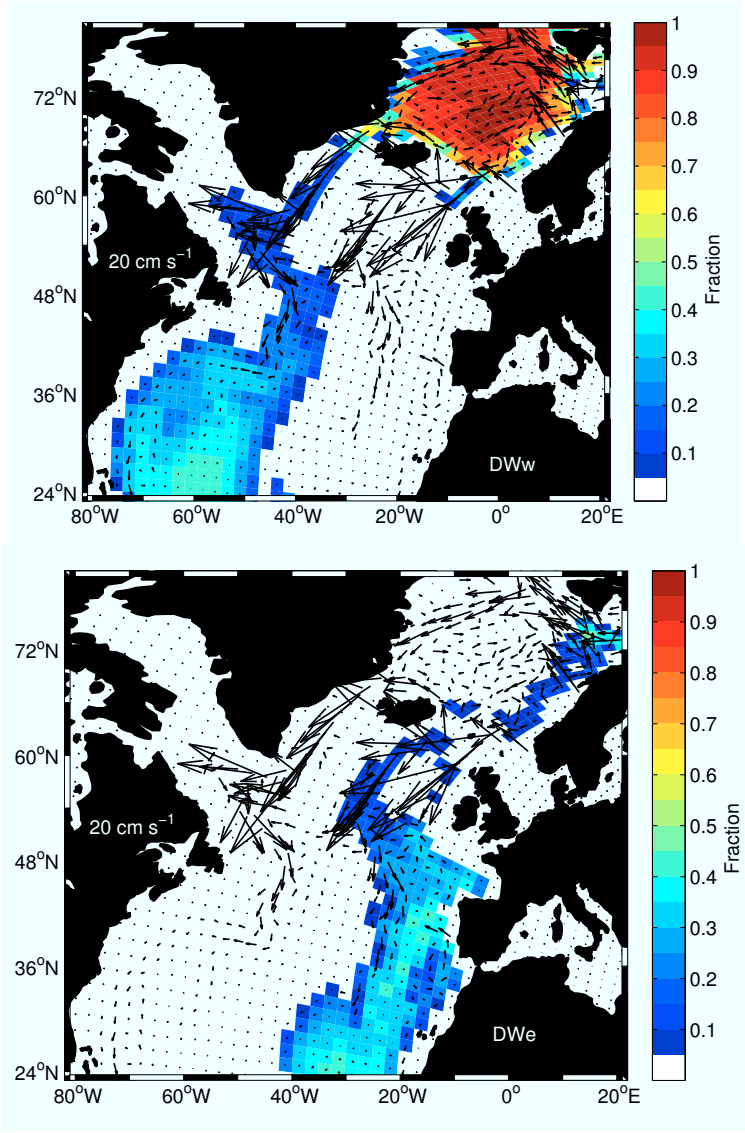

Fig. 7 Deep water velocities (layer 19-35; arrows) and fraction of the total water column (color) consisting of Deep Water west (DWw; upper) and Deep Water east (DWe; lower), with a reference velocity of 20 cm s^{-1} (cf. Fig. 4)

3.4 Atmospheric forcing and hydrography in the Labrador Sea

The average structure of the water column in the Labrador Sea is shown in Fig. 8. Layers 1, 14, and 15 have almost the same variability in thickness, temperature, and salinity (layer 1 is the mixed layer and layer 14 and 15 contain Atlantic derived water; layers 2 to 13 are empty). Cold and fresh upper layers are found when the SPG circulation is strong (not shown). Simultaneously, the temperature of the inflows through the Davis and Hudson straits is anomalously low.

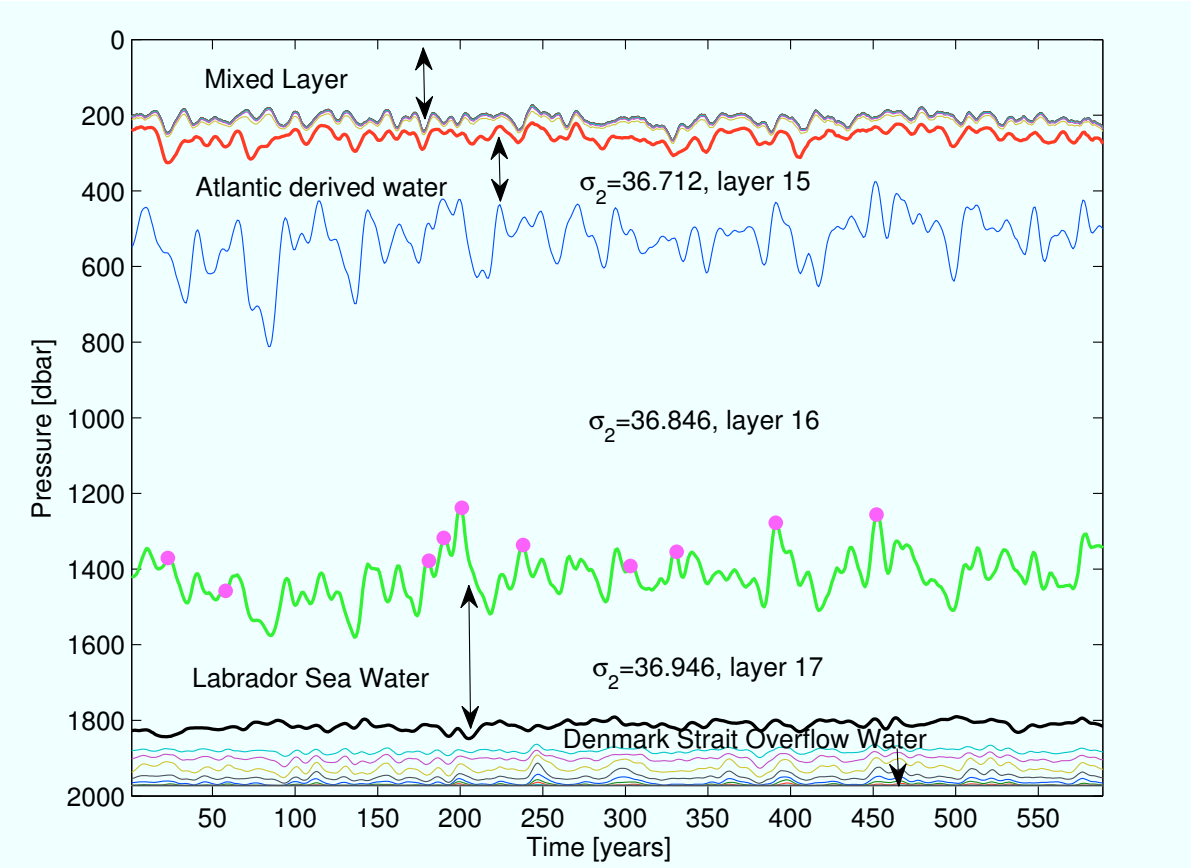

Fig. 8 Time series for the depth (dbar) of the layer interfaces averaged over the Labrador Sea. Black arrows indicate layer thickness. The σ_2-value is given for some of the layers. The magenta dots show end of NAO+ periods > 1.5 std of the filtered normalized time series

The variability of the thickness of the LSW layer is similar to that of the LSW flow in the Newfoundland section downstream (correlation of 0.74 with two yrs lag). Deeper down in the Labrador Sea, the variability of isopycnal surfaces (layer 19–24) is related to the overflow (correlation of 0.61 with the surface of layer 19, with the overflow leading by one yr). According to Fig. 7, the deepest water in the Labrador Sea originates from the Denmark Strait, hence is denoted as Denmark Strait Overflow Water in Fig. 8.

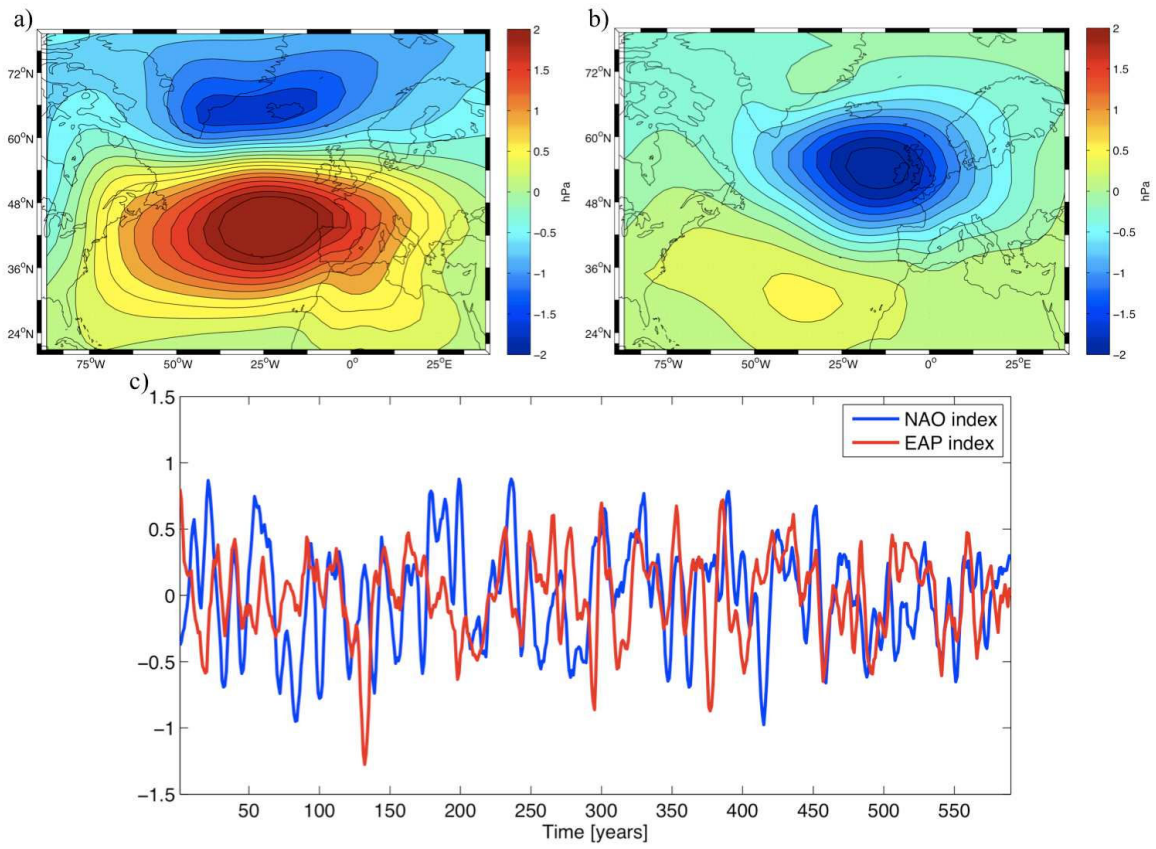

Fig. 9 The a) first and b) second empirical orthogonal function explain 43% and 12%, respectively, of the variance in the winter (November to April) mean sea level pressure field. The analysis is done for the North Atlantic sector. c) The corresponding first and second principal components; the North Atlantic Oscillation (NAO) index and East Atlantic Pattern (EAP) index

The thickness of LSW is a proxy for the amount of convective mixing in the Labrador Sea (Curry et al., 1998), which is primarily a result of the air-sea fluxes and wind forcing. Increased convection is found for increased heat loss, less fresh water input, and stronger winds in the Labrador Sea, where heat flux has highest correlation with the convection (Medhaug et al., in prep). The heat and freshwater fluxes and the momentum flux are here averaged over the Labrador Sea. The NAO index represents the dominant mode of atmospheric variability in the North Atlantic sector, and is defined here as the first principal component of the mean sea level pressure in winter (November to April) within 20˚ - 80˚N and 90˚W - 40˚E. The first empirical orthogonal function explains 43% of the variance in the mean sea level pressure field (Fig. 9a). The large-scale atmospheric pattern, represented by the NAO index (Fig. 9c), and the heat flux in the Labrador Sea both have a significant correlation with the LSW thickness (Table 4b). The LSW thickness increases during high NAO+ periods, here defined as the years when the NAO index is higher than 0.6, where the end of such periods is depicted in Fig. 8 (magenta dots).

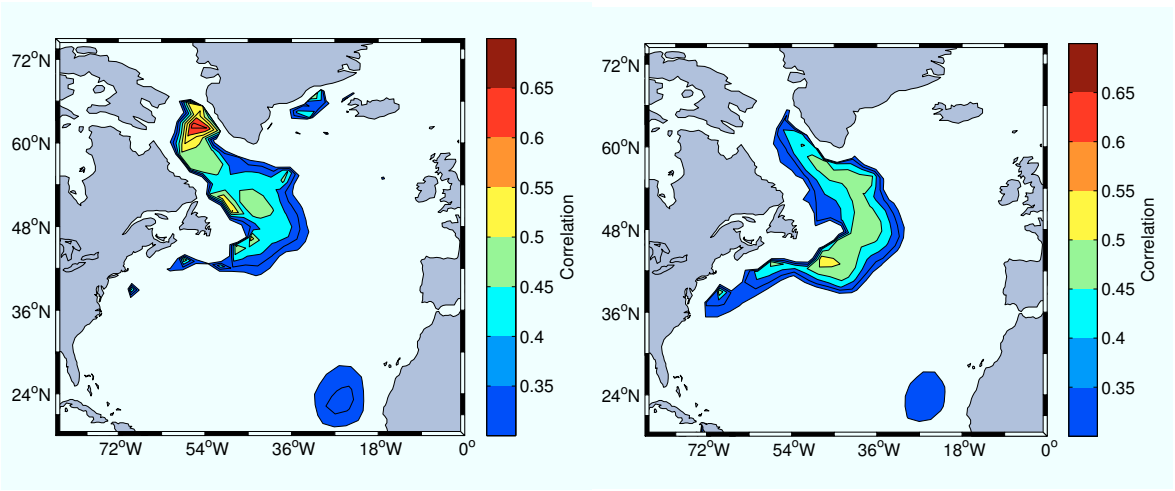

Fig. 10 Correlation between Subpolar Gyre (SPG) strength and anomalies in the layer thickness of the Labrador Sea Water (as indicated in Fig. 8) at SPG maximum (left panel) and 5 years after SPG maximum (right panel)

A thickness anomaly in the LSW layer propagates from the Labrador Sea and southwards west of the Mid-Atlantic Ridge (Fig. 10), seen from the correlations between the LSW thickness and the SPG strength, for maximum SPG strength and five years after its maximum. The hydrography of the LSW layer does not have any significant correlations with the SPG strength (not shown).

The second empirical orthogonal function explains 12% of the variance in the winter mean sea level pressure field (Fig. 9b), and resembles the East Atlantic Pattern (EAP; Barnston and Livezey, 1987). The time variability of the EAP, represented by the second principal component, is illustrated in Fig. 10c together with NAO index. The NAO index has no significant correlation with the SPG strength. On the contrary side, the EAP index has a significant correlation of 0.42 with the SPG strength, where the EAP index is leading. The NAO index is strongly related to the heat loss in the Labrador Sea (correlation of 0.65 at zero lag), while the EAP index is strongly related to the momentum flux in the subpolar region as given in Fig. 1 (correlation of 0.68, where the momentum flux leads by one year).

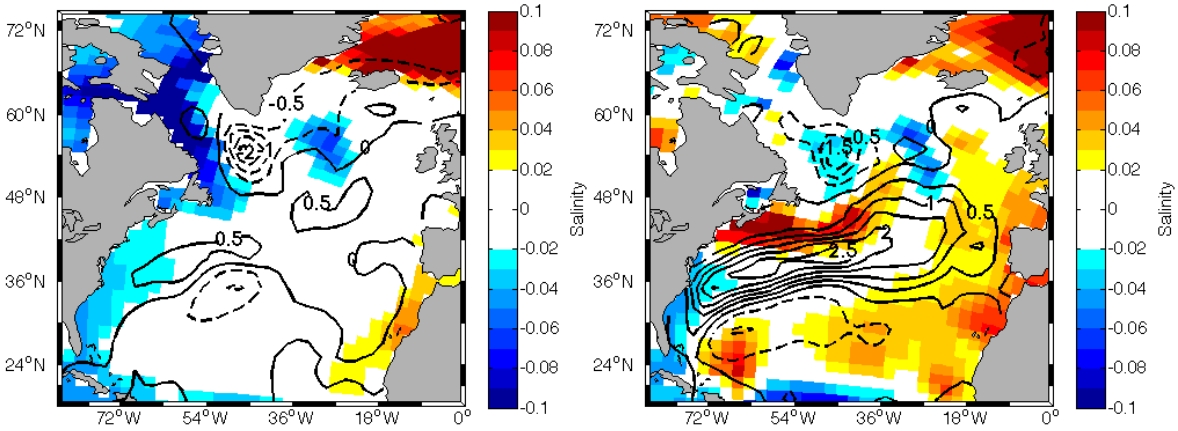

Fig. 11 Composites of anomalies in the barotropic streamfunction (black contours) and mixed layer salinity (colors) for overflow (left) and Labrador Sea Water thickness (right) larger than 1.5 std of the filtered normalized time series. Black contours are shown with 0.5 Sv intervals, where negative values are illustrated by dashed lines. Negative values imply a strengthening of the cyclonic circulation in the subpolar region

In several studies the Sea Surface Height (SSH) in the subpolar region is used to construct an index for the SPG circulation (Häkkinen and Rhines, 2004). Here we have area weighted the SSH in the central part of the model SPG, confined by 53 - 59˚N and 41 - 47˚W. The SPG strength and the SSH have a significant correlation of 0.7 (Table 4b). As the sea surface height decreases (depression) the SPG strength increases. In spite of this high correlation, these two variables cannot be used interchangeably. This is due to different response to other variables, e.g., atmospheric forcing. The SSH has a significant correlation with both the NAO and EAP index (not shown), while the SPG strength has only significant correlation with the EAP index.

3.5 Variability in the shape and strength of the Subpolar Gyre

A strong relationship between two time series may only be pronounced for a given state of the atmosphere-ocean system, giving an overall weak correlation between the corresponding time series (Brauch and Gerdes, 2005; Lohmann et al., 2009). Compositing, also sometimes called superposed epoch analysis when applied to time series (Mass and Portman, 1989), is a simple technique of sorting data into categories and comparing means for different categories (Thompson and Wallace, 2001). This technique is useful for long-term data records. Composites of anomalies in the barotropic stream function and mixed layer salinity have been made for two different criteria; only taking into account years with strong overflow, and only years with large LSW thickness (Fig. 11; only anomalies larger than 1.5

std of the filtered normalized time series are considered). When the overflow is strong (44 years included in the composite), the SPG intensifies south of Cape Farewell, up to an averaged value of 2 Sv. This is in accordance with Fig. 6, where we found that an increase of one std for the overflow is associated with an increase of around 0.8 Sv for the SPG strength. Periods of strong overflow are also related to positive salinity anomalies in the Nordic Seas and negative anomalies in the Davis Strait, Hudson Strait, and the southern coastal current in the Labrador Sea, i.e., the Labrador Current.

The associated change in the barotropic streamfunction in periods when the LSW thickness is large (42 years included in the composite) differs to some extent from what was associated with strong overflow. The SPG intensifies south of Cape Farewell, but in addition there is a large increase in the strength of the NAC of up to 2.5 Sv. Simultaneously positive salinity anomalies appear along the NAC. Also the eastern rim of the North Atlantic basin is dominated by positive salinity anomalies, while the centre of the SPG is fresher than average.

The overflow, the thickness of LSW layer, and the EAP index are all strongly correlated with the SPG strength through the 600 years time span (see Table 4), however, the correlations between these three time series are barely significant. Fig. 12 shows a multiple linear regression of the SPG strength by computing the SPG strength as a function of these three variables. The time series of predictors are shifted in time according to the time lag given in Table 4. By comparing the black and red curve in Fig. 12, it is evident that the regression model is appropriate in some periods (e.g., around year 200 and 500), while not in other periods (e.g., around year 50 and 425). Overall in the 600 years simulation, the SPG strength from the regression model has a significant correlation with the SPG strength derived from BCM (0.66). Hence, the changes in the overflow, LSW thickness, and EAP index predict the decadal variability in the SPG strength relatively well. However, in some periods there are other factors that control the variability in the SPG strength. Additional mechanisms, such as the freshwater fluxes associated with the EGC and the southward flow in the Davis Strait, could affect the structure of the water column in the Labrador Sea. For instance, buoyant eddies and shedding of boundary currents is important in the restratification of the Labrador Sea (Hátún et al., 2007). These are not resolved in BCM.

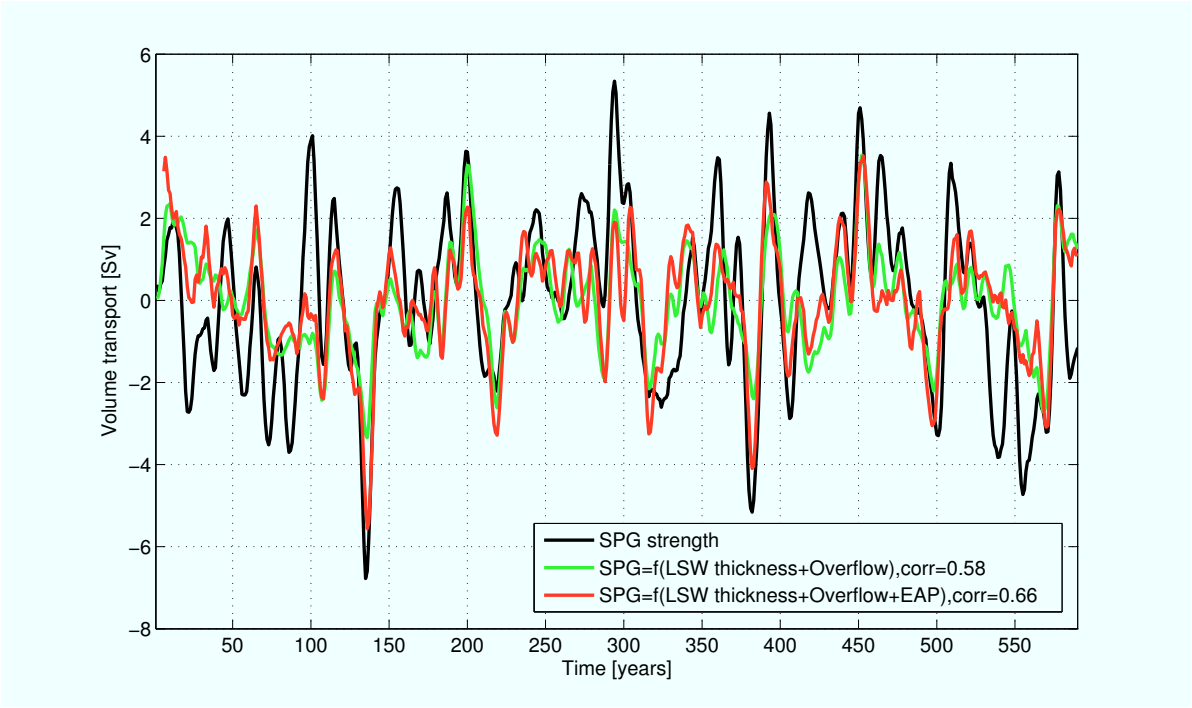

Fig. 12 Subpolar Gyre (SPG) strength modeled using a multiple linear regression as a function of the Labrador Sea Water (LSW) thickness, total overflow at the Greenland-Scotland Ridge, and East Atlantic Pattern (EAP) index. The correlation (corr) between the modeled SPG strength and the SPG strength derived from Bergen Climate Model is given in the legend

4. Discussion

In the previous section we described the shape and circulation of the SPG in the BCM enclosed by five sections. The large northern and southern sections, the GSR and the Newfoundland section, capture the main inflow and outflow branches to the subpolar region, and have therefore been the main focus of this study. A volumetric *TS*-diagram, analysing the transport of volume, heat and salt in the *TS*-plane, is applied to distinguish between the different modelled water masses at the GSR. Three water masses are evident through this analysis; the warm and saline AW, the cold and fresh PW, and the cold and dense OW. The rather distinct partition of these three components in the coarse BCM is surprising with respect to what is seen in other coupled climate models (de Jong et al., 2009). The water mass transformation in the Nordic Seas is reflected in these three branches, and is analyzed in more detail in Medhaug et al. (in prep.).

In the southern section, we distinguish between STW, LSW, MW, and DWw, and DWe. The variability in the LSW flow is linked to changes in the thickness of an intermediate layer in

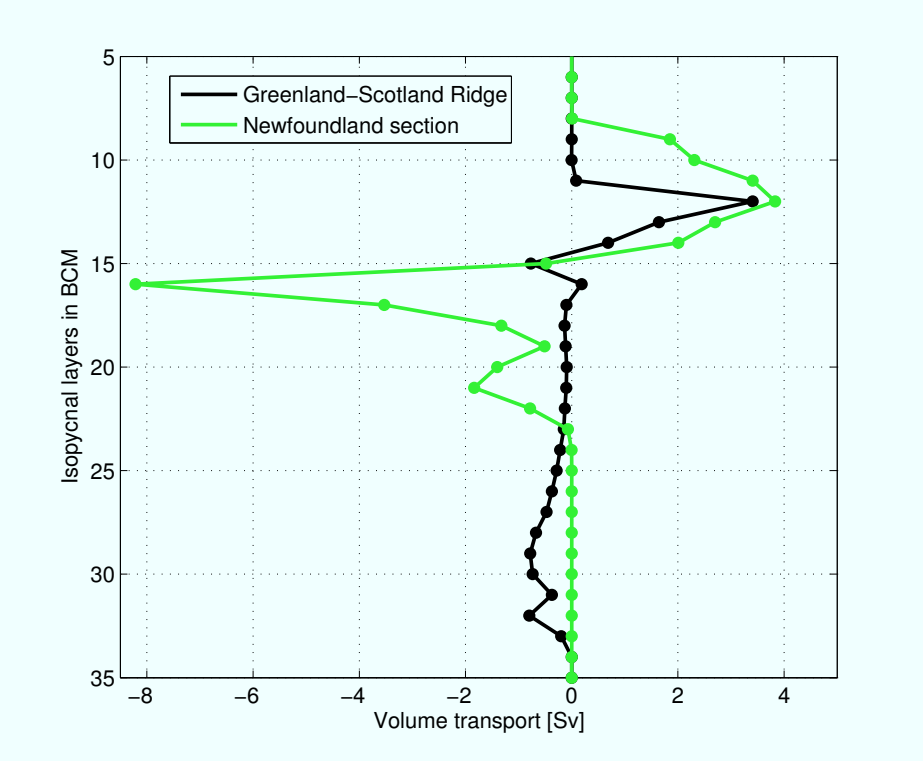

Fig. 13 Net volume transport in density space (represented by the isopycnal layers in BCM) across specific sections, as denoted in the legend. The transports also include the mixed layer transport, which is non-isopycnic. The distribution of the mixed layer transport in density space at the Greenland-Scotland Ridge can be seen in Fig. 5

the Labrador Sea, while the DWw flow is related to the DS. The DWe flow is, on other hand, more difficult to track back to its source region. This is partly due to a larger entrainment of warm and saline water compared to the DS. This can be seen from Fig. 7, where the amount of deep water with salinity higher than 35.2 (i.e., DWe) is less than 5% south of the Denmark Strait. At the GSR the temperature and salinity of the two overflows are very similar, i.e., they cannot be distinguished in the volumetric *TS*-diagram (cf. Fig. 5). The Newfoundland section reveals a different picture of the deep waters. Here one can distinguish between two cores of the deep water: relatively cold and fresh water west of the Mid-Atlantic Ridge and relatively warm and saline water east of the ridge.

The main differences in the volumetric *TS*-diagrams at the GSR and the Newfoundland section are summarized in Fig. 13. The volume transports illustrated in this figure also include the mixed layer transport, which has a time variable density. There is an evident water mass transformation in the deeper layers in the region within these two sections, and

areas of strong diapycnal mixing south of the GSR are pointed out in Medhaug et al. (in prep.). This process gives a diapycnal flux from dense water masses to lighter water masses, as the dense overflow cascades down the ridge and interacts with the warm and saline Atlantic Water. An additional section (not shown here) between Cape Farewell and Ireland shows that most of the transformation in the deep layers occurs between this section and the GSR. Lumpkin and Speer (2003) suggests that 50% of the diapycnal flux required to close the North Atlantic Meridional Overturning Circulation occurs in the DWBC between Denmark Strait and Cape Farewell. More recent studies by Cenedese and Adduce (2010) and Lauderdale et al. (2008) also point to the importance of including the entrainment when assessing the lower limb of AMOC. The amount of entrainment shapes the final properties of the overflows, and is therefore vital in determining the location and depth of the deeper water masses as they flow southward. Generally, level coordinate models tend to dilute their overflows too much, so that they are typically found at shallower depths compared to observations (Winton et al., 1998; Bryan et al., 2006). In BCM the overflow derived water is found from about 3000 m depths and down to the bottom in the Newfoundland section (see Fig. 4b and d).

The isopycnic layer (layer 16) above the LSW layer (layer 17) contains a massive southward volume transport (8 Sv) in the Newfoundland section (see Fig. 13). Half of this transport is located on the shelf break close to Newfoundland, just below the very fresh core situated on top of the shelf. The remaining half is found east of the Mid-Atlantic Ridge. The source of this water mass is not fully clear. At the GSR the volume transport in this layer is slightly northward, while it has increased to almost 7 Sv moving southward in a section between Cape Farewell and Ireland. Part of this increase can be explained by convection in the western Irminger Sea (along the coast of Greenland), which contributes to the thickening of layer 16 (not shown here).

In BCM the entrainment between the GSR and the Newfoundland sections is estimated to 3 Sv. The southward flow of deep-water increases from 5.7 Sv at the GSR (dense overflows) to 8.7 Sv at the Newfoundland section (layers 18-35; below LSW). Here, the transport associated with MW has been subtracted. A similar method to estimate the entrainment was applied by Mauritzen et al. (2005) for the overflow in the Faroese Channels (i.e., quantify the increase in the deep transport for a given density range). Only the southward transport is taken into account in our estimate of the entrainment, even though there is considerable recirculation in the Newfoundland section. The recirculation is possibly a blend of water

masses with both northern and southern origin (Antarctic intermediate water; Talley, 2008). Holliday et al. (2009) also consider the southward transport in estimates of the transport in the DWBC in sections from the Irminger Sea to the Labrador Sea.

The dynamics of the DWBC, comprising the southward flow of LSW and overflow derived water, is not yet fully understood (Bacon and Saunders, 2010; Lozier, 2010). Therefore, it has been an objective in this study to investigate and identify the deep pathways within the subpolar region. The deep water originating from the Faroe-Shetland Channel is observed to flow through the Charlie Gibbs Fracture Zone (CGFZ; Dickson and Brown, 1994; Schott et al., 1999; Smethie and Fine, 2001; LeBel et al., 2008), and vine around the Reykjanes Ridge into the Irminger basin. It then becomes part of the DWBC, sandwiched between the LSW and the deep water derived from the Denmark Strait. A recent model study by Xu et al. (2010) suggests additional pathways from the GSR to the SPG for the FSC than through the CGFZ, which include gaps through the Reykjanes Ridge and southward along the eastern flank of the Mid-Atlantic Ridge. The latter has also been proposed earlier (Smethie and Fine, 2001). In the BCM, there is a flow through the model CGFZ (Fig. 7). However, the main flow of deep water originating from the Faroe-Shetland Channel appears to be located on the eastern flank of the ridge. The water that enters the western part of the basin flows southward on the western flank of the ridge, and does not circulate in the Labrador Sea as seen in observations (Yashayaev, 2007).

The southward transport of LSW and water derived from the DS on the western side of the Mid-Atlantic Ridge is less than observational estimates of the DWBC. The DWBC is measured to be 12.9 Sv close to the Grand Banks at 43˚N (Schott et al., 2004). The model DWBC is 8.8 Sv in the Newfoundland section (about 43 - 47˚N). The 4 Sv remaining could be due to the apparent lack of a contribution from overflow-derived waters from the Faroe-Shetland Channel.

The DS dominates the variability of the total overflow in BCM (not shown), where the DS also has a higher correlation with the SPG strength compared to the total overflow (0.62 compared to 0.43). Similar results were found in Redler and Böning (1997). Furthermore, a recent study based on a fully coupled AOGCM simulation also supports a strong link between the total overflow and SPG strength (Born et al., 2009).

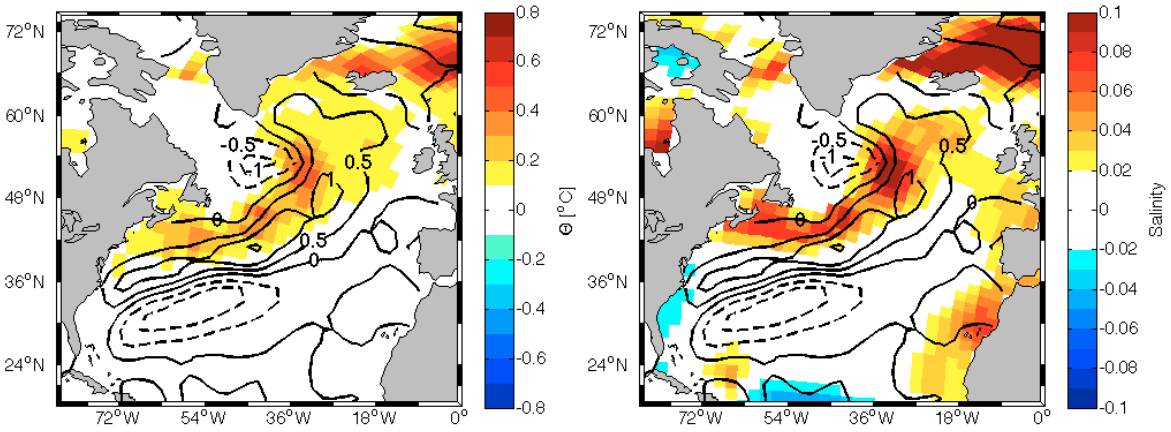

Fig. 14 Composites of anomalies in the barotropic streamfunction (black contours) and mixed layer potential temperature (left) and salinity (right) three yrs after NAO+ periods > 1.5 std of the filtered normalized time series. Black contours are shown with 0.5 Sv intervals, where negative values are illustrated by dashed lines. Negative values imply a strengthening of the cyclonic circulation in the subpolar region

The large-scale atmospheric pattern, represented by the NAO index (defined in section 3.4), has a significant correlation with the thickness of the LSW layer in BCM, which is also found in previous studies (Eden and Jung, 2001; Bentsen et al., 2004; Bailey et al., 2005). When the NAO index is in a positive phase (NAO+), cold Arctic air masses moves southward over the Canadian Archipelago and the Labrador Sea, leading to large heat loss from the ocean to the atmosphere, and a subsequent production of LSW. Lazier et al. (2002) showed that the thickness of the LSW layer is directly related to the strength of SPG. This is also the case for BCM. Fig. 14 shows the changes in hydrography and the barotropic streamfunction of the North Atlantic three yrs after NAO+ periods > 1.5 std of the filtered normalized time series. The southern inflowing branch is intensified, with positive temperature and salinity anomalies found along this path. A similar mechanism is found in the Hadley Centre Coupled Model (Cooper and Gordon, 2002). Lohman et al. (2009) suggested that these anomalies are due to advection associated with an intensified AMOC for NAO+, and that the anomalies lead to a decline in the SPG strength. Whether the associated thermohaline anomalies are mostly due to advection (by an anomalous NAC) or due to local forcing, have not been investigated herein.

The SPG relates differently to the overflow and LSW thickness, even though a positive phase for both indicates an intensified SPG circulation. An increase in the overflow is consistent with an enhanced SPG south of Cape Farewell, while an increase in the LSW

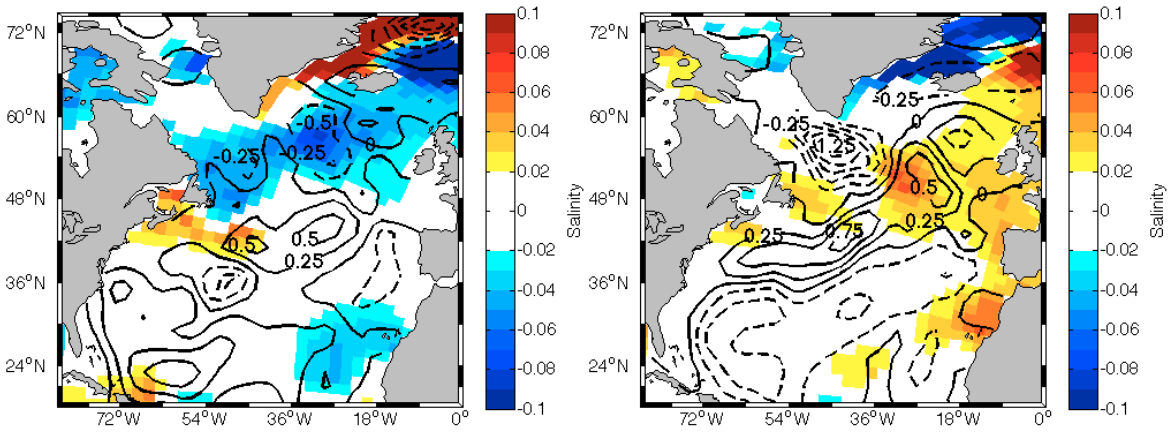

Fig. 15 Composites of anomalies in the barotropic streamfunction and mixed layer salinity when the Atlantic Water salinity anomaly at the Greenland-Scotland Ridge is larger than -1.5 std (left) and +1.5 std (right) of the filtered normalized time series. Black contours are shown with 0.25 Sv intervals, where negative values are illustrated by dashed lines. Negative values imply a strengthening of the cyclonic circulation in the subpolar region

thickness is also associated with a strengthening of the NAC (Fig. 10), which forms the upper limb of AMOC. The LSW thickness has a correlation of 0.79 with AMOC (at zero lag; see Table 4). The SPG strength and AMOC have a correlation of 0.53, where the SPG is leading AMOC by one year. Other model simulations also suggest this strong connection between the SPG circulation and the AMOC (e.g., Häkkinen, 2001; Bentsen et al., 2004; Böning et al., 2006; Gao and Yu, 2008).

Hátún et al. (2005) and Levermann and Born (2007) find that the salinity of the Atlantic inflow to the Nordic Seas reflects changes in the SPG dynamics. In this model simulation, there is no clear relationship between the SPG strength and the properties of the AW. However, composites of anomalies in the barotropic streamfunction and mixed layer salinity for large anomalies in the AW salinity (i.e., larger than 1.5 std of the filtered normalized time series) indicate consistent changes in the subpolar region (Fig. 15). For a negative anomaly (i.e., when the AW salinity is low), the eastern subpolar region is fresher than normal, and there is an intensification of the cyclonic circulation in this area. There is a weaker intensification south of Cape Farewell, which may be the reason for the lack of correlation between the SPG strength and the AW salinity. When the AW salinity is high, there is a strong intensification of the cyclonic circulation south of Cape Farewell, while the circulation in the western subpolar region has an anti-cyclonic anomaly.

5. Summary and Conclusions

There is increasing evidence that the Subpolar Gyre (SPG) holds a key role in modulating the Atlantic Meridional Overturning Circulation (AMOC) and the exchanges between the Atlantic proper and the Arctic Mediterranean (Hátún et al., 2005; Häkkinen and Rhines, 2009; Lohmann et al., 2009; Lozier, 2010). It is thus essential to understand the processes affecting the gyres role in ocean circulation and thus northern climate, including decadal scale variability, which is the scope of the present research. The natural variability of this region must in particular be constrained if the emerging field of climate prediction is to be skilful for the North Atlantic region (Dunstone and Smith, 2010). The maximum AMOC north of 20˚N is a frequently used index to diagnose climate change in the North Atlantic. Importantly, the structure of northward flowing Subtropical Water (STW) is rather complex in the subpolar region, where the North Atlantic Current (NAC) breaks up into several pathways feeding sites of deep water formation (Brambilla and Talley, 2008). The distribution of heat and salt in this area reflect both the meridional overturning and the SPG circulations (Hátún et al., 2005).

In previous studies, decadal changes in the SPG circulation have been associated with changes in the intensity of deep convection in the Labrador Sea, the strength of the Nordic Seas Overflow, and upper ocean hydrography in the northeastern Atlantic (Born et al., 2009; Sarafanov et al., 2010). The goal of this study has been to further elucidate these relationships on decadal scale, using a multi-century simulation of the Bergen Climate Model (BCM). The main results from this study are as follows:

- The mean water mass exchange on the Greenland-Scotland Ridge (GSR) is well represented in BCM, comprising the warm and saline Atlantic Water (AW), the cold and fresh Polar Water (PW), and the cold and dense Overflow Water (OW).

- The spatial structure of the model temperature and salinity in a section from Newfoundland to Portugal compares favourably to observations. However, the deep water (below ~1000 m) has a bias towards warmer and more saline waters, and the North Atlantic Current (NAC) core is shifted eastward compared to observations. The model DWBC is less than found in observational estimates. This could be due to the pathway of Faroe Shetland Channel Overflow (FSC), which is mainly located on the eastern flank of the Mid-Atlantic Ridge.

- The strength of the overflow at the GSR and deep convection in the Labrador Sea (represented by the thickness of Labrador Sea Water, LSW) are the factors, considered in this analysis, which have strongest relationship with the SPG strength. The overflow leads the SPG strength by one year, while the LSW thickness changes simultaneously with the SPG strength.

- The Denmark Strait Overflow (DS) dominates the variability of the total overflow across the GSR. It propagates southward on the western side of the Mid-Atlantic Ridge, and its signal is seen three years later near Grand Banks.

- The North Atlantic Oscillation (NAO) index is strongly related to the heat flux in the Labrador Sea, and controls part of the decadal variability of the LSW thickness. The East Atlantic Pattern (EAP) index is strongly related to the averaged momentum flux in the subpolar region.

- A multiple linear regression function, with the overflow, LSW thickness, EAP index time series as predictors, has an overall correlation of 0.66 with the SPG strength derived from BCM. However, this relationship is not evident for all time segments in the 600 years integration, indicating that other factors might be important as well.

- The overflow and the LSW thickness have different imprint on the shape of the SPG circulation. The response due to a strengthening of the overflow is localized to an intensification of the SPG just south of Cape Farewell. A thickening of the LSW layer is both related to an intensification of the SPG in the same area, and a strengthening of the NAC.

The subpolar North Atlantic is the linkage between the temperate subtropics and the cold Arctic, and the processes within this region are connected to the meridional overturning and the poleward heat transport in the North Atlantic. It is thus of great importance to assess the variability in this region. A continued evaluation of the performance and nature of climate models will allow us to identify which mechanisms are robust, and which are not. It is essential to be aware of where and for which time scales the climate models are representative and reliable, and where they are inadequate. The focus in this study has been on the model representation of temperature and salinity in the North Atlantic Ocean, i.e., in reproducing the main water masses, and the associated transports. These properties of the

ocean have earlier not been of prime focus in model studies, but are key to provide reliable simulations of climate (Bailey et al., 2005).

Acknowledgement

The project has been supported by the Research Council of Norway through the BIAC (H. R. Langehaug and T. Eldevik) and NorClim (I. Medhaug and O. H. Otterå) projects. This publication is no. XXXX from the Bjerknes Centre for Climate Research, and this research uses data provided by the Bergen Climate Model (BCM) project (www.bcm.uib.no) at the Bjerknes Centre for Climate Research, largely funded by the Research Council of Norway. We thank Helge Drange, Peter B. Rhines, and Mats Bentsen for insightful and helpful guidance when preparing this paper.

References

Aagaard, K., and E. C. Carmack, 1989: The role of sea ice and other fresh water in the Arctic circulation. *J. Geophys. Res.*, **94**(C10): 14 485–14 498.

Bacon, S., 1997: Circulation and fluxes in the North Atlantic between Greenland and Ireland. *J. Phys. Oceanogr.*, **27**: 1420–1435.

Bacon, S., and P. M. Saunders, 2010: The Deep Western Boundary Current at Cape Farewell: Results from a Moored Current Meter Array. *J. Phys. Oceanogr.*, **40**: 815-829, doi: 10.1175/2009JPO4091.1.

Bailey, D. A., P. B. Rhines, and S. Häkkinen, 2005: Formation and pathways of North Atlantic Deep Water in a coupled ice-ocean model of the Arctic-North Atlantic Oceans. *Climate Dyn.*, **25**: 497–516, doi: 10.1007/s00382-005-0050-3.

Barnston, A. G., and R. E. Livezey, 1987: Classification, seasonality and persistence of low-frequency atmospheric circulation patterns. *Mon. Wea. Rev.*, **115**: 1083–1126.

Bentsen, M., H. Drange, T. Furevik, and T. Zhou, 2004: Simulated variability of the Atlantic meridional overturning circulation. *Climate Dyn.*, **22**: 701-720, doi: 10.1007/s00382-004-0397-x.

Bleck R., C. Rooth, D. Hu, and L. T. Smith, 1992: Salinity-driven thermocline transients in a wind- and thermohaline-forced isopycnic coordinate model of the North Atlantic. *J. Phys. Oceanogr.*, **22**: 1486–1505.

Brambilla, E., and L. D. Talley, 2008: Subpolar mode water in the northeastern Atlantic: 1. Averaged properties and mean circulation. *J. Geophys. Res.*, **113**, C04025, doi: 10.1029/2006JC004062.

Böning, C. W., F. O. Bryan, W. R. Holland, and R. Döscher, 1996: Deepwater formation and meridional overturning in a high-resolution model of the North Atlantic. *J. Phys. Oceanogr.*, **26**, 1142–1164.

Böning, C. W., M. Scheinert, J. Dengg, A. Biastoch, and A. Funk, 2006: Decadal variability of subpolar gyre transport and its reverberation in the North Atlantic overturning. *Geophys.*

Res. Lett., **33**, L21S01, doi: 10.1029/2006GL026906.

Born, A., A. Levermann, and J. Mignot, 2009: Sensitivity of the Atlantic circulation to a hydraulic overflow parameterization in a coarse resolution model. *Ocean Modelling*, **27**: 132–140, doi: 10.1016/j.oce.mod.2008.11.006.

Brauch, J. P., and R. Gerdes, 2005: Response of the northern North Atlantic and Arctic oceans to a sudden change of the North Atlantic Oscillation. *J. Geophys. Res.*, **110**, C11018, doi: 10.1029/2004JC002436.

Bryan, F. O., G. Danabasoglu, N. Nakashiki, Y. Yoshida, D. H. Kim, J. Tsutsui, and S. C. Doney, 2006: Response of the North Atlantic thermohaline circulation and ventilation to increasing carbon dioxide in CCSM3. *J. Climate*, **19**: 2382–2397, doi: 10.1175/JCLI3757.1.

Cane, M. A., 2010: Climate science: Decadal predictions in demand. *Nat. Geosci.*, **3**: 231–232, doi: 10.1038/ngeo823.

Cenedese, C., and C. Adduce, 2010: A New Parameterization for Entrainment in Overflows. *J. Phys. Oceanogr.*, **40**: 1835-1850, doi: 10.1175/2010JPO4374.1.

Chelton, D. B., 1983: Effects of sampling errors in statistical estimation. *Deep-Sea Res.*, **30**: 1083-1101.

Clarke, R.A., 1984: Transport through the Cape Farewell-Flemish Cap section. *Rapp. P. V. Reun. Cons. Int. Explor. Mer.*, **185**: 120-130.

Cooper, C., and C. Gordon, 2002: North Atlantic oceanic decadal variability in the Hadley Centre coupled model. *J. Climate*, **15**: 45–72.

Curry, R., M. McCartney, and T. Joyce, 1998: Oceanic transport of subpolar climate signals to mid-depth subtropical waters. *Nature*, **391**: 575–577.

de Jong, F., S. S. Drijfhout, W. Hazeleger, H. M. van Aken, and C. A. Severijns, 2009: Simulations of hydrographic properties in the north western North Atlantic Ocean in Coupled Climate Models. *J. Climate*, **22**(7): 1767-1786, doi: 10.1175/2008JCLI2448.1.

Delworth, T. L., and M. E. Mann, 2000: Observed and simulated multidecadal variability in the Northern Hemisphere. *Climate Dyn.*, **16**: 661–676.

Dengler, M., J. Fischer, F.A. Schott, and R. Zantopp, 2006: Deep Labrador Current and its variability in 1996-2005. *Geophys. Res. Lett.*, **33**, L21S06, doi: 10.1029/2006GL026702.

Déqué M., C. Dreveton, A. Braun, and D. Cariolle, 1994: The ARPEGE/IFS atmosphere model: a contribution to the French community climate modelling. *Climate Dyn.*, **10**: 249–266.

Deshayes, J., and C. Frankignoul, 2008: Simulated Variability of the Circulation in the North Atlantic from 1953 to 2003. *J. Climate*, **21**: 4919–4933, doi: 10.1175/2008JCLI1882.1.

Deshayes, J., C. Frankignoul, and H. Drange, 2007: Formation and export of deep water in the Labrador and Irminger Seas in a GCM. *Deep-Sea Res. I*, **54**: 510–532, doi: 10.1016/j.dsr.2006.12.014.

Dickson, R.R., and J. Brown, 1994: The production of North Atlantic Deep Water: sources, rates and pathways. *J. Geophys. Res.*, **99**: 12319–12341.

Döscher, R., and R. Redler, 1997: The relative influence of North Atlantic overflow and subpolar deep convection on the thermohaline circulation in an OGCM. *J. Phys. Oceanogr.*, **27**: 1894-1902.

Dunstone, N. J., and D. M. Smith, 2010: Impact of atmosphere and sub-surface ocean data on decadal climate prediction, *Geophys. Res. Lett.*, **37**, L02709, doi:10.1029/2009GL041609.

Eden, C., and T. Jung, 2001: North Atlantic interdecadal variability: Oceanic response to the North Atlantic Oscillation (1865-1997). *J. Climate*, **14**: 676-691.

Eden, C., and J. Willebrand, 2001: Mechanism of inter-annual to decadal variability of the North Atlantic Oscillation. *J. Climate*, **14**: 2266–2280.

Eldevik, T., J. E. Ø. Nilsen, D. Iovino, K. A. Olsson, A. B. Sandø, and H. Drange, 2009: Observed sources and variability of Nordic seas overflow. *Nat. Geosci.*, **2**: 406–410, doi: 10.1038/ngeo518.

Furevik, T., M. Bentsen, H. Drange, I. K. T. Kindem, N. G. Kvamstø, and A. Sorteberg, 2003: Description and validation of the Bergen Climate Model: ARPEGE coupled with MICOM. *Climate Dyn.*, **21**: 27–51, doi: 10.1007/s00382-003-0317-5.

Gao, Y. Q., and L. Yu, 2008: Subpolar gyre index and the North Atlantic meridional overturning circulation in a coupled climate model. *Atmos. and Oceanic Sci. Lett.*, **1**: 29–32.

Häkkinen, S., 2001: Variability in sea surface height: A qualitative measure for the meridional overturning in the North Atlantic. *J. Geophys. Res.*, **106**(C7): 13837-13848.

Häkkinen, S., and P. B. Rhines, 2004: Decline of Subpolar North Atlantic circulation during the 1990s. *Science*, **304**: 555-559, doi: 10.1126/science.1094917.

Häkkinen, S., and P. B. Rhines, 2009: Shifting surface currents in the northern North Atlantic Ocean. *J. Geophys. Res.*, **114**, C04005, doi: 10.1029/2008JC004883.

Hátún, H., C. C. Eriksen, and P. B. Rhines, 2007: Buoyant Eddies Entering the Labrador Sea Observed with Gliders and Altimetry. *J. Phys. Oceanogr.*, **37**: 2838–2854, doi: 10.1175/2007JPO3567.1.

Hátún, H., A. B. Sandø, H. Drange, B. Hansen, and H. Valdimarsson, 2005: Influence of the Atlantic Subpolar Gyre on the Thermohaline Circulation. *Science*, **309**: 1841-1844, doi: 10.1126/science.1114777.

Holliday, N. P., S. Bacon, J. Allen, E. L. McDonagh, 2009: Circulation and Transport in the Western Boundary Currents at Cape Farewell, Greenland. *J. Phys. Oceanogr.*, **39**, 1854–1870. doi: 10.1175/2009JPO4160.1.

Holliday, N. P., J. J. Waniek, R. Davidson, D. Wilson, L. Brown, R. Sanders, R. T. Pollard, and J. T. Allen, 2006: Large-scale physical controls on phytoplankton growth in the Irminger Sea Part I: Hydrographic zones, mixing and stratification. *J. Mar. Syst.*, **59**: 201–218, doi:

10.1016/j.jmarsys.2005.10.004.

Kuhlbrodt, T., A. Griesel, M. Montoya, A. Levermann, M. Hofmann and, S. Rahmstorf, 2007: On the driving processes of the Atlantic Meridional Overturning Circulation. *Rev. Geophys.*, **45**, RG2001, doi: 10.1029/2004RG00166.

Lauderdale, J. M., S. Bacon, A. C. Naveira Garabato, and N. P. Holliday, 2008: Intensified turbulent mixing in the boundary current system of southern Greenland. *Geophys. Res. Lett.*, **35**, L04611, doi: 10.1029/2007GL032785.

Lazier, J., R. Hendry, A. Clarke, I. Yashayaev, and P. Rhines, 2002: Convection and restratification in the Labrador Sea, 1990–2000. *Deep-Sea Res. I*, **49**, 1819–1835.

LeBel, D. A., and Coauthors, 2008: The formation rate of North Atlantic Deep Water and Eighteen Degree Water calculated from CFC-11 inventories observed during WOCE. *Deep-Sea Res. I*, **55**: 891–910, doi: 10.1016/j.dsr.2008.003.009.

Lee, M.-M., A. J. G. Nurser, A. C. Coward, and B. A. de Cuevas, 2007: Eddy advective and diffusive transports of heat and salt in the Southern Ocean. *J. Phys. Oceanogr.*, **37**: 1376–1393, doi: 10.1175/JPO3057.1.

Levermann, A., and A. Born, 2007: Bistability of the Atlantic subpolar gyre in a coarse resolution climate model. *Geophys. Res. Lett.*, **34**, L24605, doi: 10.1029/2007GL031732.

Lohmann, K., H. Drange, and M. Bentsen, 2009: Response of the North Atlantic subpolar gyre to persistent North Atlantic Oscillation like forcing. *Climate Dyn.*, **32**: 273-285, doi: 10.1007/s00382-008-0467-6.

Lumpkin, R., and K. Speer, 2003: Large-scale vertical and horizontal circulation in the North Atlantic Ocean. *J. Phys. Oceanogr.*, **33**(9): 1902-1920.

Lozier, M. S., 2010: Deconstructing the Conveyor Belt. *Science*, **328**: 1507-1511, doi: 10.1126/science.1189250.

Mauritzen, C., 1996: Production of dense overflow waters feeding the North Atlantic across the Greenland-Scotland Ridge. Part 1: Evidence for a revised circulation scheme. *Deep-Sea Res. I*, **43**: 769–806.

Mauritzen, C., J. Price, T. Sanford, and D. Torres, 2005: Circulation and mixing in the Faroese Channels. *Deep-Sea Res. I*, **52**: 883–913, doi: 10.1016/j.dsr.2004.11.018.

McCartney, M. S., and L. D. Talley, 1982: The Subpolar Mode Water of the North Atlantic. *J. Phys. Oceanogr.*, **12**: 1169–1188.

Nilsen, J. E. Ø., H. Hátún, K. A. Mork, and H. Valdimarsson, 2008: The NISE Data Set. Technical Report 08-01 (Faroese Fisheries Laboratory, Box 3051, Tórshavn, Faroe Islands), 17 pp.

Nilsson, J., G. Bjork, B. Rudels, P. Winsor, and D. Torres, 2008: Liquid freshwater transport and Polar Surface Water characteristics in the East Greenland Current during the AO-02 Oden expedition. *Prog. Oceanogr.*, **78**: 45–57, doi: 10.1016/j.pocean.2007.06.002.

Olsen, S. M., B. Hansen, D. Quadfasel, and S. Østerhus, 2008: Observed and modeled stability of overflow across the Greenland–Scotland ridge. *Nature*, **455**: 519-522, doi: 10.1038/nature07302.

Østerhus, S., W. R. Turrell, S. Jónsson, and B. Hansen, 2005: Measured volume, heat, and salt fluxes from the Atlantic to the Arctic Mediterranean. *Geophys. Res. Lett.*, **32**: L07603, doi: 10.1029/2004GL022188.

Otterå, O. H., M. Bentsen, I. Bethke, and N. G. Kvamstø, 2009: Simulated pre-industrial climate in Bergen Climate Model (version 2): model description and large-scale circulation features. *Geosci. Mod. Dev.*, **2**: 197-212.

Pèrez-Brunius, P., T. Rossby, and D. R. Watts, 2004: The transformation of the warm waters of the North Atlantic from a streamfunction perspective. *J. Phys. Oceanogr.*, **34:** 2238-2256.

Redler, R., and C. W. Böning, 1997: Effect of the Overflows on the Circulation in the Subpolar North Atlantic: A Regional Model Study. *J. Geophys. Res.*, **102**(C8): 18529-18552.

Roberts, M. J., and R. A. Wood, 1997: Topography sensitivity studies with a Bryan–Cox-type ocean model. *J. Phys. Oceanogr.*, **27**: 823–836.

Rudels, B., H. J. Friedrich, and D. Quadfasel, 1999: The Arctic Circumpolar Boundary Current. *Deep-Sea Res. II*, **46**: 1023–1062.

Salas-Mélia, D., 2002: A global coupled sea ice-ocean model. *Ocean Modelling*, **4**: 137–172, doi: 10.1016/S1463.4003(01)00015.4.

Sarafanov, A., A. Falina, P. Lherminier, H. Mercier, A. Sokov, and C. Gourcuff, 2010: Assessing decadal changes in the Deep Western Boundary Current absolute transport southeast of Cape Farewell, Greenland, from hydrography and altimetry. *J. Geophys. Res.*, **115**, C11003, doi: 10.1029/2009JC005811.

Schott, F., and P. Brandt, 2007: Circulation and Deep Water export of the subpolar North Atlantic during the 1990s. *Ocean circulation: mechanisms and impacts. Geophys. Monogr.,* Vol. 173, Amer. Geophys. Union, 91–118.

Schott, F., L. Stramma, and J. Fischer, 1999: Interaction of the North Atlantic Current with the deep Charlie-Gibbs Fracture Zone throughflow. *Geophys. Res. Lett.*, **26**: 369–372.

Schott, F. A., R. Zantopp, L. Stramma, M. Dengler, J. Fischer, and M. Wibaux, 2004: Circulation and deep-water export at the western exit of the subpolar North Atlantic. *J. Phys. Oceanogr.*, **34**: 817–843.

Smethie W. M., and R. A. Fine, 2001: Rates of North Atlantic Deep Water formation calculated from chlorofluorocarbon inventories. *Deep-Sea Res. I*, **48**: 189–215, doi: 10.1016/S0967-0637(00)00048-0.

Smethie W. M., R. A. Fine, A. Putzka, and E. P. Jones, 2000: Tracing the flow of North Atlantic Deep Water using chlorofluorocarbons. *J. Geophys. Res.*, **105**:14297–14323, doi: 10.1029/1999JC900274.

Talley, L. D., 2008: Freshwater transport estimates and the global overturning circulation: Shallow, deep and through flow components. *Prog Oceanogr.*, **78**: 257-303, doi: 10.1016/j.pocean.2008.05.001.

Talley, L. D., and M. S. McCartney, 1982: Distribution and circulation of Labrador Sea Water. *J. Phys. Oceanogr.*, **12**: 1189–1205.

Thompson, D. W. J., and J. M. Wallace, 2001: Regional Climate Impacts of the Northern Hemisphere Annular Mode. *Science*, **293**: 85-89, doi: 10.1126/science.1058958.

van Aken, H. M., and G. Becker, 1996: Hydrography and through-flow in the northeastern North Atlantic Ocean: the NANSEN project. *Prog. Oceanogr.*, **38**: 297-346.

Winton, M., R. Hallberg, and A. Gnanadesikan, 1998: Simulation of density-driven frictional downslope flow in z-coordinate ocean models. *J. Phys. Oceanogr.*, **28**: 2163–2174.

Xu, X., W. J. Schmitz Jr., H. E. Hurlburt, P. J. Hogan, and E. P. Chassignet, 2010: Transport of Nordic Seas overflow water into and within the Irminger Sea: An eddy-resolving simulation and observations. *J. Geophys. Res.*, **115**, C12048, doi: 10.1029/2010JC006351.

Yashayaev, I., 2007: Hydrographic changes in the Labrador Sea, 1960–2005. *Prog. Oceanogr.*, **73**: 242–276, doi: 10.1016/j.pocean.2007.04.015.